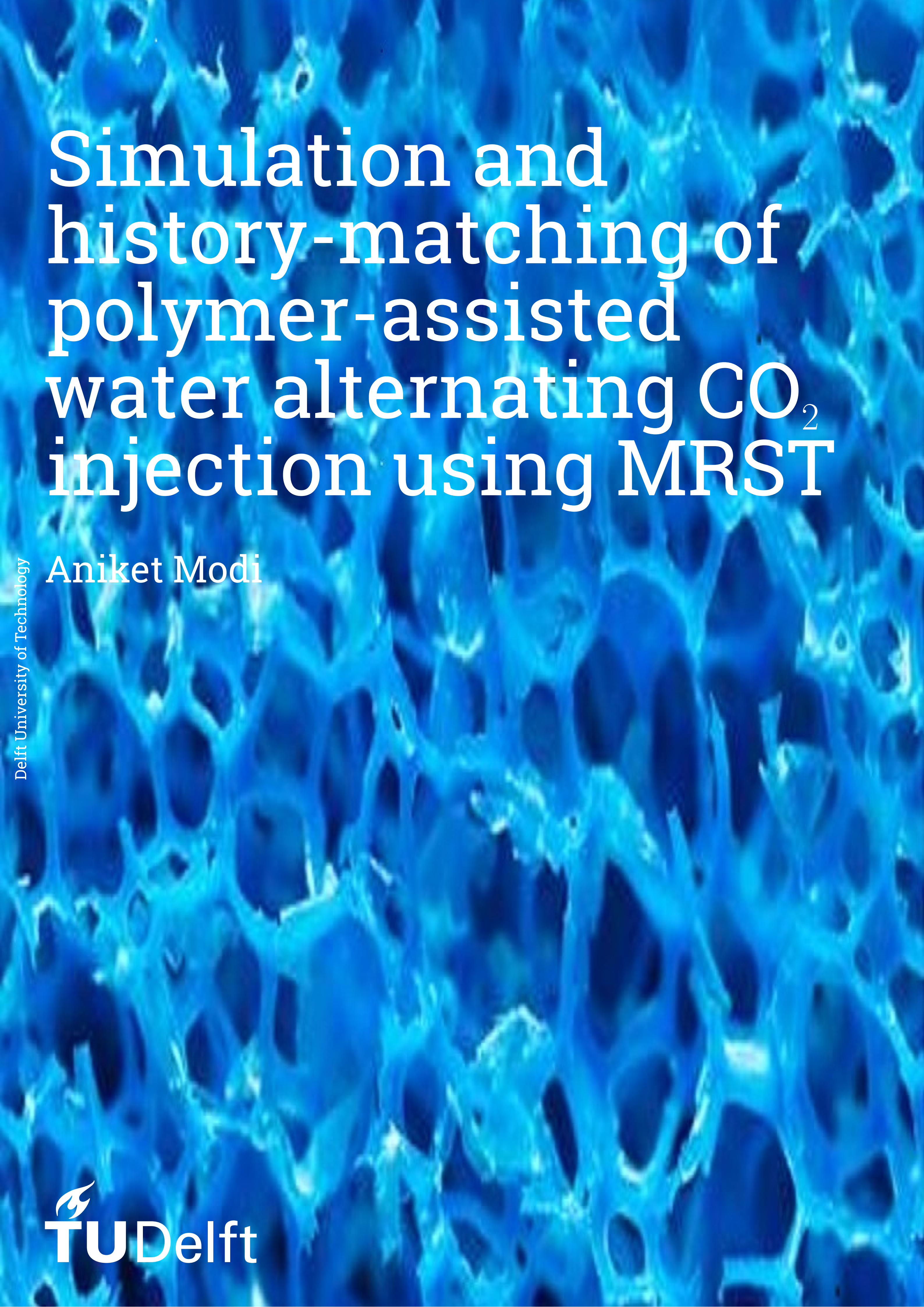

Simulation and history-matching of polymer-assisted water alternating CO$_2$ injection using MRST

Aniket Modi

Delft University of Technology

TUDelft

Simulation and history-matching of polymer-assisted water alternating CO_2 injection using MRST

by

Aniket Modi

to obtain the degree of
Master of Science
in Applied Earth Science
at the Delft University of Technology,
to be defended publicly on Thursday, August 31, 2023 at 10:30 AM.

Student number:	5250404	
Project duration:	Novemebr 9, 2022 – August 31, 2023	
Supervisors:	Prof. dr. P.L.J. Zitha,	TU Delft
	Dr. M. Mirzaie. Yegane,	TU Delft, DPI[1]
Thesis committee:	Prof. dr. P.L.J. Zitha,	TU Delft
	Dr. M. Mirzaie. Yegane,	TU Delft, DPI[1]
	Dr. A. Fadili,	Shell
	Prof. Knut-Andreas Lie,	SINTEF
	Dr. Stephan Toby,	TU Delft
	Dr. Sian Jones,	TU Delft

[1] DPI, P.O. Box 902, 5600 AX Eindhoven, the Netherlands.

Abstract

CO_2 flooding is a widely employed method for enhancing oil recovery. However, it faces challenges stemming from differences in viscosity and density between oil and CO_2, leading to poor sweep efficiency. This can result in issues such as viscous fingering, channelling, and gravity segregation, causing premature breakthroughs and excessive gas production. To address these concerns, the Polymer Assisted Water Alternating Gas (PA-WAG) technique combines the advantageous attributes of CO_2 flooding, such as solubility and displacement, with the effective mobility control provided by polymer flooding. This results in a chemically enhanced Water Alternating Gas (WAG) flooding approach. A study by van Wieren et al. (2022) delved into the effectiveness of PA-WAG in addressing CO_2 flow challenges and improving sweep efficiency by conducting core-flood experiments. This work builds upon that study by employing numerical simulations to replicate the core-flood experiments. These simulations shed light on the fundamental physical mechanisms during the PA-WAG injection process while also facilitating the calibration of flow parameters for practical implementation on a larger scale. The primary goal of this study was to comprehensively model three distinct enhanced oil recovery (EOR) techniques: polymer injection, CO_2 flooding, and PA-WAG, all applied specifically to the Bentheimer sandstone cores. The objective was to history-match CT (Computed Tomography) scan saturation data, observed pressure drops, and oil recovery. A 2-dimensional (2D) model was constructed for each experiment, with CT scan images used to allocate varying porosity and permeability values to individual grid blocks. This enabled monitoring saturation distributions from the initial primary drainage phase onward. In the history matching of the primary drainage phase, parameters for relative permeabilities were determined from the Brooks-Corey equation, leveraging CT scan saturation data. The scaling of relative permeabilities based on CT scan saturations effectively accounted for capillary end effects observed in the core-flood experiments. During the history-matching of the polymer injection process, it was demonstrated that polymer-specific parameters, as determined from experimental data, could effectively modify waterflood relative permeabilities, thereby reducing the mobility ratio and accurately capturing the advancement of the polymer front. The formation of emulsions towards the end of polymer injection led to a notable increase in pressure drop, necessitating the incorporation of a high Residual Resistance Factor (RRF) to accommodate permeability reduction. In the case of history-matching for the CO_2 flood, the black oil model successfully replicated the process of immiscible gas injection. It aptly captured gravity segregation while utilising CT scan saturation scaled relative permeabilities to assess the impact on oil recovery. The study unveiled that the relative permeability of gas under immiscible conditions was relatively lower than in miscible and near-miscible conditions. Simulating the PA-WAG injection by combining polymer and CO_2 models effectively reproduced the core-flood experiments. The study substantiated the role of gas trapping in reducing the relative permeability of gas as a function of injection time, consequently leading to heightened pressure drops during subsequent polymer slug injections. The study showcased the efficacy of integrating black oil models for polymer and CO_2 injection to successfully simulate PA-WAG injection and achieve unity with core-flood experiments yielding valuable insights into the physical processes underlying the technique.

Acknowledgments

I wish to convey my sincere gratitude to Prof. Dr Pacelli Zitha, my esteemed head supervisor, for bestowing upon me this invaluable opportunity and for generously sharing his vast experience, time, and knowledge across every facet of this thesis. I also sincerely appreciate Dr Mohsen Mirzaie Yegane, whose unwavering guidance, support, motivation, and wealth of expertise played an integral role in the successful execution of this project. Their encouragement has been instrumental in enabling me to produce work of the highest quality.

This committed group of experts imparted vital insights and expertise drawn from their adeptness, actively moulding the strategic approach that culminated in noteworthy findings within this endeavour. Their input has accelerated my learning curve and ignited a profound enthusiasm for reservoir engineering within me. Additionally, I extend my gratitude to Prof. Knut-Andreas Lie and SINTEF for granting me access to and supporting my work with MRST.

I would like to extend a special acknowledgement to Dr Ali Fadili from Shell for the engaging discussions and invaluable insights exchanged during our bi-weekly meetings. These interactions have significantly guided the trajectory of this project in a positive direction.

I extend my gratitude to the esteemed members of my graduation committee: Dr Ali Fadili, Prof. Knut-Andreas Lie, Dr Stephan Toby and Dr Sian Jones. Their keen interest in my work and the opportunity they've offered me to graduate are deeply cherished.

Lastly, I wish to thank all my professors and classmates who have been part of this journey and convey my profound gratitude to my family and friends. Their constant support throughout this thesis has provided me with comfort and encouragement during even the most overwhelming moments.

The work of Aniket Modi forms part of the research programme of DPI, project 849.

Contents

List of Figures

List of Tables

Nomenclature

Abbreviations

Abbreviation	Definition
1D	1-Dimensional
2D	2-Dimensional
3D	3-Dimensional
AD-OO	Automatic Differentiation Object Oriented
ATBS	Acrylomido Tertiary Butyl Sulfonate
AMPS	2-acrylamido-2-methyl propane sulfonic acid
CCS	Carbon Capture and Storage
CO_2	Carbon Dioxide
CT	Computed Tomography
EOR	Enhanced Oil Recovery
Exp 1	Polymer Flood Experiment
Exp 2	CO_2 Flood Experiment
Exp 3	PA-WAG Injection Experiment
HCPV	Hydrocarbon Pore Volume
HPAM	Hydrolyzed Polyacrylamide
IFT	Interfacial Tension
IPV	Inaccessible Pore Volume
MMP	Minimum Miscibility Pressure
MRST	MATLAB Reservoir Simulation Toolbox
OIP	Oil in Place
OIIP	Oil Initially in Place
PA-WAG	Polymer Assisted Water Alternating Gas
PAM	Polyacrylamide
PF	Polymer Flood
ppm	Parts Per Million
PV	Pore Volume
PVI	Pore Volumes Injected
RF	Resistance Factor
RRF	Residual Resistance Factor
WAG	Water Alternating Gas

Symbols

Symbol	Definition	Unit
A	Core Cross-Sectional Area	m^2
b_o	Inverse Oil Formation Volume Factor	-
b_g	Inverse Gas Formation Volume Factor	-
b_w	Inverse Water Formation Volume Factor	-
c	Polymer Concentration	kg/m^3
c^a	Polymer Adsorption Concentration	kg/m^3
D_p	Grain Diameter	mm
E	Total Recovery Efficiency	%
E_d	Displacement Efficiency	%

Symbol	Definition	Unit
E_v	Volumetric Sweep Efficiency	%
f_w	Fractional Flow of Water	-
g	Acceleration due to gravity	m/s^2
K	Consistency Index	-
k	Absolute Permeability	$Darcy$
k_{row}	Oil Relative Permeability in Oil-Water System	-
k_{rog}	Oil Relative Permeability in Gas-Oil System	-
k_{rg}	Gas Relative Permeability	-
k_{rw}	Water Relative Permeability	-
k_{roe}	Oil End-Point Relative Permeability	-
k_{rge}	Gas End-Point Relative Permeability	-
k_{rwe}	Water End-Point Relative Permeability	-
M	Mobility Ratio	-
N_{ca}	Capillary Number	-
P_c	Capillary Pressure	bar
p	Reservoir Pressure	bar
p_w	Wellbore Pressure	bar
n	Flow Behaviour Index	-
n_o	Brooks-Corey Shape Coefficient for Oil	-
n_g	Brooks-Corey Shape Coefficient for Gas	-
n_w	Brooks-Corey Shape Coefficient for Water	-
q_o	Oil Flow Rate	m^3/day
q_g	Gas Flow Rate	m^3/day
q_w	Water Flow Rate	m^3/day
$R_k(c)$	Reduced Permeability	-
r_s	Solution Gas Oil Ratio	m^3/m^3
r_v	Vapour Oil Gas Ratio	m^3/m^3
ST	User Defined Surface Tension	$dyne/cm$
S_o	Oil Saturation	-
S_g	Gas Saturation	-
S_w	Water Saturation	-
S_{orw}	Residual Oil Saturation in Oil-Water System	-
S_{org}	Residual Oil Saturation in Gas-Oil System	-
S_{gr}	Residual Gas Saturation	-
S_{wr}	Residual Water Saturation	-
S_{lc}	Residual Liquid Saturation	-
S_{oi}	Initial Oil Saturation	-
$S_{or,PF}$	Residual oil saturation after polymer flooding	-
S_{or,CO_2}	Residual oil saturation after CO_2 flooding	-
s_{ipv}	Inaccessible Pore Volume	-
v	Darcy Velocity	m/s
W_I	Well Index	-
α	Carmen-Kozeny Factor	-
ΔP	Pressure Differential	$mbar$
∇P	Pressure Gradient	bar
λ	Fluid mobility	-
λ_{bo}	Brine mobility before polymer injection	-
λ_{b1}	Brine mobility after polymer injection	-
λ_p	Mobility of polymer solution	-
μ	Viscosity	cP or $Pa.s$
$\mu_{w,eff}$	Effective Water Viscosity	cP or $Pa.s$
$\mu_{p,eff}$	Effective Polymer Viscosity	cP or $Pa.s$
σ	Interfacial Tension	N/m
τ	Shear Stress	N/m^2 or Pa

Symbol	Definition	Unit
γ	Shear Rate	s^{-1}
ϕ	Porosity	-
ρ_o	Oil Density	kg/m^3
ρ_g	Gas Density	kg/m^3
ρ_w	Water Density	kg/m^3
ρ_r	Reservoir Rock Density	kg/m^3
ω	Polymer Mixing Parameter	-

1

Introduction

1.1. General Introduction

The energy transition encompasses more than just power generation. It involves shifting the sector's reliance on fossil fuels like oil, coal, and natural gas for electricity generation towards renewable resources such as wind, solar, hydro, and geothermal energy. The broader objective is to reduce carbon dioxide (CO_2) emissions across all sectors while advancing energy storage and electrifying significant industries and transportation systems. However, despite efforts to transition to cleaner energy sources, it is essential to acknowledge that oil remains the most significant energy supplier currently and in the foreseeable future. Renewable energy projects often struggle to be profitable, and besides being a fuel source, oil is essential for producing everyday items like plastics, lubricants, waxes, and asphalts. Amid global efforts to find alternative energy sources and lessen reliance on oil while fulfilling environmental obligations, the oil demand persists in its upward trajectory [53]. This compels the requirement for developing and adopting innovative approaches that not only cater to the goal of enhancing oil recovery to tackle the increasing demand but also hold potential for applications in improving the efficiency of carbon capture and storage (CCS). Such approaches can play a pivotal role in substantially curbing CO_2 emissions.

The productive lifespan of an oil field can be categorised into three main stages: primary, secondary, and tertiary recovery. During the primary recovery stage, the production relies solely on the natural energy present in the reservoir, such as gas cap expansion, solution-gas expansion, aquifer influx, rock compaction, and gravity drainage. Primary recovery continues until the original energy source can no longer generate profitable production rates [37]. Secondary recovery methods are employed once the reservoir pressure declines to a level where oil production becomes challenging. These methods involve injecting water into the reservoir to increase pressure or gas into the gas cap to displace remaining oil towards production wells, thereby extending the field's lifespan. The secondary recovery stage concludes when significant amounts of water or gas are produced, rendering the process economically unfeasible [37]. Following the secondary recovery phase, where capillary forces dominate over viscous forces in the porous media, a considerable portion of the oil remains trapped. In the tertiary recovery stage, various techniques modify the initial properties of the in-situ fluids and rock-fluid interactions. These techniques are collectively known as enhanced oil recovery (EOR) methods and include miscible displacement (such as injecting CO_2 or hydrocarbon gas when reservoir pressure conditions are favourable), thermal recovery (involving steam injection or in-situ combustion), and chemical flooding (utilising alkaline, surfactant, polymer, or their combinations). These EOR methods can also be applied during the primary and secondary recovery stages [27].

One widely used method for oil recovery is CO_2 injection, which has been commercially employed for over four decades. It is the second most common EOR technique, following steam flooding [63]. CO_2 injection not only increases oil recovery but also has the potential to store CO_2 in reservoirs, thereby reducing greenhouse gas emissions. However, due to the significant differences in viscosity and density between oil and CO_2, the CO_2 injection process suffers from poor sweep efficiency. Challenges such as viscous fingering, channelling through high permeability streaks, and gravity segregation result in premature breakthrough and gas production [3]. While Water-Alternating-Gas (WAG) injection has been employed to enhance the mobility contrast and has demonstrated improved performance compared to continuous gas injection, it may not eliminate the challenges posed by viscous instabilities and gravity segregation [20].

To overcome the problems of gas breakthrough and gravity segregation, a new combination method called Polymer Assisted Water Alternating Gas (PA-WAG) was proposed. PA-WAG combines the benefits of CO_2 flooding, including solubility and displacement, with the superior mobility control of polymer flooding, resulting in a chemically enhanced WAG flooding process. However, the stability of polymers under reservoir conditions, such as high pressure, temperature, salinity levels, and CO_2, needs to be considered. To assess the effectiveness of PA-WAG, van Wieren et al. (2022) [65] conducted a CT (Computed Tomography)-aided core-flood experimental study. This study examined the stability of the polymer in combination with CO_2 and its impact on viscosity retention. The results demonstrated the technique's effectiveness in mitigating CO_2 flow issues in porous media, thereby enhancing reservoir sweep efficiency.

While the experiments have shown the effectiveness of PA-WAG injection, it is crucial to conduct thorough numerical simulation work to history-match the core-flood experiments. This will allow a deeper comprehension of the physical mechanisms that impact flow dynamics during PA-WAG injection. Additionally, it will assist in calibrating the flow parameters involved in the process, which can then be utilised in pilot or sector-scale models to optimise the injection schemes and predict the performance of PA-WAG in real-world applications [33]. Ultimately, the numerical simulations will enhance our understanding of PA-WAG injection and its potential benefits on a larger scale.

1.2. Research Questions and Objectives

This research focuses on understanding and improving the CO_2 flow in porous media, which has implications for underground CO_2 storage and EOR. The inherent challenges of poor reservoir sweep efficiency, including viscous fingering, channelling through high permeability streaks, and gravity override, are addressed through PA-WAG injection. Previous CT-aided core-flood experiments by van Wieren et al. (2022) [65] have demonstrated the success of PA-WAG in enhancing reservoir sweep efficiency. This research aims to investigate the physical mechanisms involved in the PA-WAG injection process by developing a model based on the black oil approach in MATLAB Reservoir Simulation Toolbox (MRST). The core-flood experiments will be history-matched using the model to determine the parameters required for simulating the injection scheme in a sector model for a field-scale study. The research is based on two central hypotheses: (1) The model developed using the black oil approach in MRST effectively captures the intricate physical mechanisms of the PA-WAG process. (2) Mechanistic simulation of the PA-WAG process replicates the core-flood experiments resulting in a successful history-match. The research questions derived from these hypotheses will be the foundation for further investigation and analysis.

(1) The model developed using the black oil approach in MRST effectively captures the intricate physical mechanisms of the PA-WAG process.

The research question associated with the first hypothesis states that: How can the model capture the impact of the main physical mechanisms, such as the displacement efficiency of CO_2 and mobility control of the polymer on improving the oil recovery in the PA-WAG process ? Regarding this question, the hypothesis states that the existing three-phase black oil model and the polymer flood model of MRST can be coupled to develop a model that effectively captures the intricate physical mechanisms of the PA-WAG process. The polymer model in MRST uses flow equations based on the black oil model. The underlying assumption is that polymer, transported in the aqueous phase, changes the viscosity of this phase without affecting the liquid, oleic, and gaseous phases. The physical effects of adding polymers, such as a change in effective viscosities, polymer adsorption, permeability reduction, inaccessible pore space and the non-Newtonian rheology of the polymer solution, are well accounted for in this model. Similarly, the three-phase black oil model is well equipped to simulate the flow of gaseous CO_2 through porous media in the presence of liquid and oleic phases within the system. The objective here would be to couple features of immiscible CO_2 flooding with polymer flooding so that the interaction of CO_2 with oil, water and polymer and its impact on the sweep efficiencies and overall hydrocarbon recovery can be effectively modelled.

(2) Mechanistic simulation of PA-WAG process replicates the core-flood experiments resulting in a successful history-match.
The research question related to the second hypothesis focuses on determining the most efficient workflow for matching the model to the core-flood experimental data. This research aims to replicate the laboratory conditions of the core-flood experiments, which were conducted under immiscible conditions where CO_2 behaves as a gas. To achieve this, the objective is to model the core-flood experiments in a step-by-step manner systematically. The first step involves investigating and understanding the recovery mechanisms of polymer and immiscible gas flooding by running separate simulations of each process. An understanding of the physical mechanisms involved in each case can be developed by studying these individual processes. Once the mechanisms of polymer flooding and immiscible gas flooding are understood, the next step is to model the PA-WAG injection. In this case, the PA-WAG process will be modelled as immiscible using the black oil model, which consists of dead oil and dry gas. In combination with the polymer flood model, the black oil model will allow for successful history-matching of the core-flood experiments and calibration of flow parameters. The outcome of this research will be a base case that can be used in future studies to simulate the PA-WAG process under varying conditions. Additionally, the base case can be applied to sector models for field-scale analysis. By developing an efficient workflow for matching the model to the core-flood experimental data, insights into the performance and effectiveness of the PA-WAG process can be gained, paving the way for further optimisation and application in the oil and gas industry.

1.3. Thesis Outline

This study models and simulates polymer flooding, gas (CO_2) flooding, and the PA-WAG injection process. Core-flood experiments performed by van Wieren et al. (2022) [65] are history-matched using MRST, which is a free, open-source software for reservoir modelling and simulation developed primarily by the Computational Geosciences group in the Department of Mathematics and Cybernetics at SINTEF Digital in Norway. This thesis investigates the physical mechanisms associated with PA-WAG injection by simulating the core-flood experimental results. This study analyses the methodology for modelling and simulating the PA-WAG injection aiming to provide insights into the underlying physical mechanisms involved in the process.

The thesis is structured into five chapters, which include the introduction, literature review, methodology, results and discussion, and conclusion. The introduction addresses the research objectives outlined in section 1.2. Chapter 2 comprehensively reviews previous studies and literature related to polymer behaviour, CO_2 behaviour, and PA-WAG application in EOR processes. Chapter 3 details the method for setting up and executing the core-flood simulations. This includes reviewing the experimental data to identify the critical parameters for consideration during the history-matching process, explaining the reservoir simulator's framework, understanding the models' governing equations, and outlining the procedure for simulating the individual core-flood experiments. Chapter 4 presents the results obtained from the simulations and provides a thorough analysis and discussion of the findings. The results are carefully examined, and their implications are discussed concerning the research questions. Finally, in Chapter 5, the research questions are addressed and answered, and the study's findings are drawn. Additionally, recommendations for future research work are provided. Overall, the thesis is structured to provide a comprehensive understanding of the research objectives, review the relevant literature, describe the methodology used, present and discuss the simulation results, and finally draw conclusions and propose future research directions.

2

Literature Review

2.1. Enhanced Oil Recovery

The primary goal of the EOR techniques is to achieve the best performance in terms of recovery and economic aspects. Several EOR techniques are applied throughout the industry to create a more efficient movement of displacing and displaced fluids in the reservoir. These techniques are primarily centred around maintaining a favourable mobility ratio (M < 1.0) and increasing the capillary number (N_{ca}). The mobility ratio is defined as:

$$M = \frac{\lambda_{displacing}}{\lambda_{displaced}} \tag{2.1}$$

The mobility ratio impacts both micro and macro sweep displacement efficiencies. It determines the relative ease of fluid movement within the reservoir. A favourable mobility ratio is achieved by ensuring the displacing fluid has a higher viscosity than the displaced fluid. The capillary number (N_{ca}) is given as:

$$N_{ca} = \frac{v\mu}{\sigma} \tag{2.2}$$

where σ is the interfacial tension (IFT) (N/m), μ is the viscosity of the displacing fluid ($Pa.s$), and v is the Darcy velocity (m/s). Apart from maintaining a favourable mobility ratio, one of the strategies is to increase the capillary number. By increasing the capillary number, the viscous forces can overcome the capillary forces more effectively. This leads to improved fluid flow and displacement efficiency within the reservoir. This is done by reducing the IFT using a surfactant or thermal energy. Increasing the capillary number by three orders of magnitudes decreases the residual oil saturation by 50% [54]. The performance of flooding processes such as water, gas, and WAG injection is highly dependent on the macroscopic (volumetric) and microscopic (displacement) efficiencies [54]. Displacement efficiency refers to the effectiveness of the injecting fluid in displacing oil from the pore spaces within the reservoir. It represents the portion of the oil initially in place (OIIP) produced by the displacing fluid. A higher displacement efficiency indicates that a larger fraction of the oil in the reservoir is effectively displaced and recovered. On the other hand, volumetric sweep efficiency relates to the extent of contact between the injected fluid and the oil within the reservoir. It measures the fraction of the reservoir volume swept by the injected fluid and is influenced by factors such as reservoir heterogeneity, fluid mobility, and the injection strategy employed. A higher volumetric sweep efficiency means that a larger portion of the reservoir has been in contact with the injected fluid and is more effectively swept of oil. The total oil recovery efficiency is a combination of both displacement (E_d) and volumetric efficiency (E_v) [58], as given below:

$$E = E_d \times E_v \tag{2.3}$$

where E is the total recovery efficiency (%). By optimising both displacement and volumetric sweep efficiencies, the total oil recovery efficiency can be maximised.

2.2. Polymer Flooding

Polymers play a vital role in EOR technology by significantly impacting reservoir dynamics. When polymers are added to the reservoir, they enhance water viscosity and decrease the relative permeability of water. This, in turn, boosts oil recovery by increasing the fractional flow. If the mobility ratio is close to one or slightly lower, the water displaces oil efficiently, resembling piston-like displacement [13]. Leveraging the mobility ratio principle, water-soluble polymers can be employed to increase the water phase viscosity and reduce the water permeability within the porous rock, thereby establishing a more effective and uniform front for displacing oil from the reservoir [29, 38].

2.2.1. Fundamentals of Polymer Flooding

Polymers are materials made up of multiple monomers connected in chains. A monomer can consist of one or more atoms and serves as the building block for the repeating units that form the long-chain structure of the polymer. In addition to polymers with single monomers, there are also copolymers with two or more distinct monomers. Water-soluble polymer agents used in polymer-based EOR can be classified into synthetic polymers and biopolymers [11]. Synthetic polymers, like hydrolysed polyacrylamide (HPAM), are artificially synthesised from acrylamide monomers and are commonly used due to their cost-effectiveness [48]. Biopolymers, derived from natural resources such as cellulose, xanthan gum, chitosan, or algae, are also used in EOR. Xanthan gum, produced by pseudoxanthomonas, is a widely used biopolymer in the petroleum industry due to its tolerance to salinity and temperature ranges [46]. Biopolymers improve mobility ratio, selectively plug thief zones, and redirect waterflood towards inaccessible oil pores. However, they are less utilised in field-wide applications due to ageing, microbial degradation, and formation damage from pore plugging. Microbial degradation affects both synthetic and biopolymers, but biopolymers are more prone to degradation. Additionally, biopolymers face injection issues due to biomaterial debris accumulation at the wellbore wall [15].

To enhance oil production, secondary flooding is commonly employed, during which water is injected into the reservoir to displace the oil towards the production well [57]. However, this approach is not always efficient due to the immiscibility of oil and water. With its low viscosity, water penetrates the oil and reaches the production well, while the oil remains trapped in the reservoir. This phenomenon, caused by the difference in viscosity, is known as the fingering effect [38]. To address this issue, polymers are added to the injected water, increasing its viscosity and thus lowering the mobility ratio between water and oil [11]. This prevents the fingering of water into the oil, allowing for a more uniform displacement and better sweep efficiency, thereby improving the flooding process and increasing oil recovery.

2.2.2. Macroscopic and Microscopic Sweep Efficiency Improvement

Mobility Ratio The main principle behind using polymers in oil recovery is to reduce the mobility ratio between water and oil. The mobility ratio (M) represents the difference in mobility between the two phases. When polymers are added to water, the resulting highly viscous water has lower mobility than oil, allowing it to act as a piston-like front that displaces the oil [11]. Buckley-Leverett Eq.2.4 shows this polymer flooding mobility ratio as:

$$f_w = \frac{\frac{k_{rw}}{\mu_w}}{\frac{k_{rw}}{\mu_w} + \frac{k_{ro}}{\mu_o}} = \frac{M}{1+M} = \frac{1}{1+\frac{1}{M}} \tag{2.4}$$

where k_{rw} and k_{ro} refer to the relative permeability of water and oil, respectively, whereas μ_w and μ_o denote the water and oil viscosity. According to Eq.2.4, when M is less than 1, the fractional flow curve indicates a piston-like flow, resulting in higher average water saturation. This leads to a reduction in residual oil remaining in the reservoir [26]. Therefore, $M \leq 1$ is considered favourable, while $M > 1$ creates an unfavourable mobility condition that can cause a viscous fingering effect.

Permeability Reduction Permeability reduction, also known as relative permeability modification, refers to the ability of polymers to decrease excessive water production while enhancing oil recovery [56]. It involves reducing the relative permeability of water by introducing a polymer gel, which blocks water permeability in the targeted region [50]. This reduction occurs in polymer flooding due to various factors, including wettability alteration, segregation of oil and water flow pathways, swelling and shrinkage of the polymer gel, and the formation of a polymer layer on pore walls through adsorption [71]. However, the primary reason for permeability reduction is polymer adsorption and the segregation of flow pathways, diverting the water drive away from vacant under-swept pores in the producing zone [50]. By plugging these high-permeability layers, the drive fluid is redirected into the oil-rich zone, further enhancing oil recovery. Significantly, the blockade effect of the polymer gel does not affect the recovery of residual oil since it can be easily removed compared to permanent plugging caused by cement [51].

Polymer Rheology Polymer solutions exhibit non-Newtonian behaviour, meaning the relationship between viscosity, shear stress, and shear rate is not linear. These solutions can display three types of rheological behaviour in a porous medium: Newtonian, shear thinning, and shear thickening. However, EOR polymers typically exhibit shear thinning characteristics, often analogous to the pseudoplastic behaviour observed in rheological studies. Shear thinning behaviour refers to the fluid's response to applied stress, decreasing viscosity as the shear rate increases [1]. The power law equation 2.5 describes the relationship of a shear-thinning polymer solution as it follows a shear-thinning pattern.

$$\tau = K(\gamma)^n \tag{2.5}$$

where K denotes the consistency index, γ symbolises the shear rate, τ is the shear stress, and n refers to the flow behaviour index. The rheological behaviour of power-law fluids is characterised by two parameters: K and n. The flow behaviour index (n) is dimensionless, while the dimension of K depends on the specific value of n. Pseudoplastic behaviour, or shear thinning, occurs when $n < 1$. In this case, the apparent viscosity of the fluid decreases as the shear rate increases. On the other hand, when $n > 1$, the fluid exhibits dilatant behaviour, which is a different type of non-Newtonian fluid where the apparent viscosity increases with the increase in shear rate [14, 66].

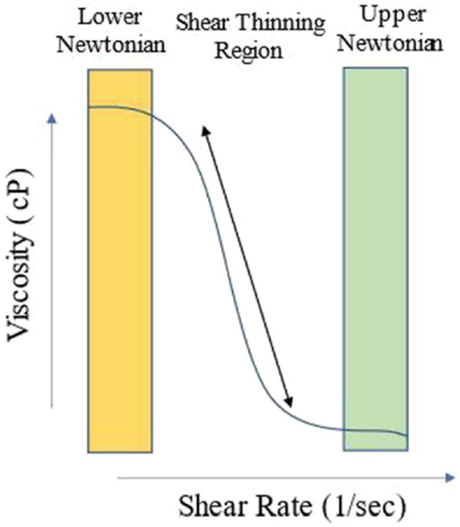

Figure 2.1: Shear rate dependency of polymers [15]

When a polymer solution flows through a series of pores, its molecules experience elongation and contraction stresses. As a result, the apparent viscosity of the polymer solution decreases with increasing shear rate (Figure 2.1). This phenomenon occurs due to the arrangement of polymeric molecules within the shear rate field, leading to reduced internal friction. The polymer solution exhibits a homogeneous behaviour at lower shear rates, resembling a lower Newtonian fluid. However, as the shear rate increases, the apparent viscosity of the polymer solution decreases, following a power law relationship (Figure 2.1). This region of decreasing viscosity with increasing shear rate is known as shear thinning. Shear-thinning improves polymer flow efficiency by reducing resistance, but the large size and broad molecular weight distribution of polymers used in EOR can lead to increased flow resistance and pore blockage, necessitating controlled chain scission (controlled pre-shearing) to enhance their flow efficiency in porous media and counteract time-dependent injectivity decline [35]. On the other hand, shear thickening behaviour can occur in polymer solutions during high-velocity flows when the molecules do not have enough relaxation time to recoil and adapt to the flow geometry. This behaviour can help rapidly displace mobile fluids but may still face challenges in effectively displacing hard-to-displace oil from small-scale heterogeneities [62].

2.2.3. Impact of Reservoir Properties

Reservoir Heterogeneity Reservoir heterogeneity significantly influences the success of oil recovery during polymer flooding. Heterogeneity is characterised by variations in reservoir quality, including porosity, permeability, capillary pressure, and water saturation. When polymers interact with fluids and the porous medium, they can alter specific rock properties. One of the effects of polymer flooding is an increase in viscosity and mobility ratio, which enhances oil recovery. Additionally, permeability reduction is introduced to decrease water production. However, this reduction in permeability can cause severe damage to the reservoir, which is irreversible and leads to increased oil production costs and reduced productivity. Due to the capillary effect, polymers can plug the pore walls and reduce the relative permeability of water while not significantly affecting the relative permeability of oil. This occurs as adsorption-entanglement polymer layers are formed, altering the flow characteristics within the reservoir (Figure2.2).

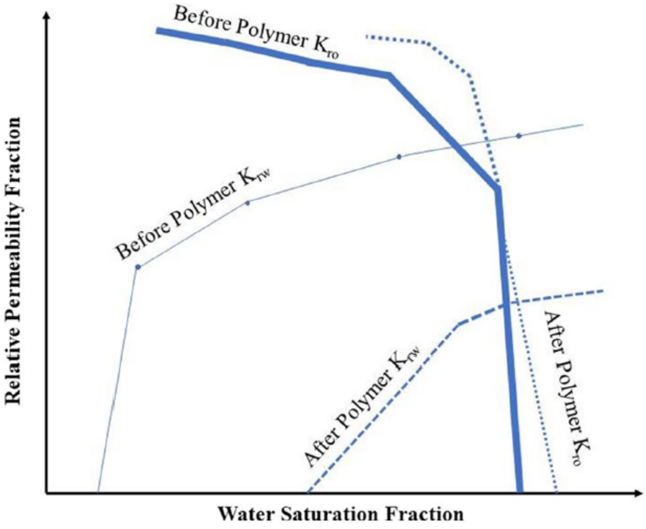

Figure 2.2: Effect of polymer adsorption on relative permeabilities of oil and water [69]

The resistance factor (RF) is the ratio of the mobilities of the brine and the polymer solution and is related to pressure drop according to the following equation:

$$RF = \frac{\lambda_{bo}}{\lambda_p} = \frac{\Delta P_p}{\Delta P_{bo}} \tag{2.6}$$

where λ and ΔP are the mobility and pressure drop, respectively and where the subscripts b_o and p refer to the brine before the polymer injection and polymer solution. In practice, RF shows an increase during the polymer injection due to the viscosity increase and a reduction in permeability [66]. The residual resistance factor (RRF) describes the permeability reduction after the polymer injection. It is the ratio of the brine mobility before the polymer injection (corresponding to subscript bo) to the brine mobility after the polymer injection (corresponding to subscript $b1$):

$$RRF = \frac{\lambda_{bo}}{\lambda_{b1}} = \frac{\Delta P_{b1}}{\Delta P_{bo}} \tag{2.7}$$

Inaccessible Pore Volume The fraction of the rock pore volume inaccessible to the polymer during flooding is known as the inaccessible pore volume (IPV). When the size of the polymer molecules is larger than the pore size in a porous medium, the polymer cannot pass through those pores. The IPV is influenced by factors such as the size and concentration of the polymer, the charge on the polymer, the concentration of divalent ions, salinity, the effect of the rock surface, temperature, and the pore size of the rock, including dead-end pores [59]. IPV plays a crucial role in polymer transport within porous media. It is one of several mechanisms affecting polymer behaviour. In situations where IPV is the dominant factor, it can lead to polymer acceleration [43]. Polymer acceleration occurs when the polymer solution is injected at a lower salinity than the reservoir salinity, creating a contrast in ionic strength and improving the transport efficiency of the polymer [1].

2.2.4. Impact of Fluid Properties

Polymer Retention and Relaxation Time The retention of polymeric molecules in porous media can occur when high flow rates push the polymers into cavities where they become trapped. Polymer retention is influenced by various factors, including polymer concentration, salinity, permeability, and injection velocity [6]. The polymer retention mechanism in the porous medium is based upon three mechanisms, as shown in figure 2.3.

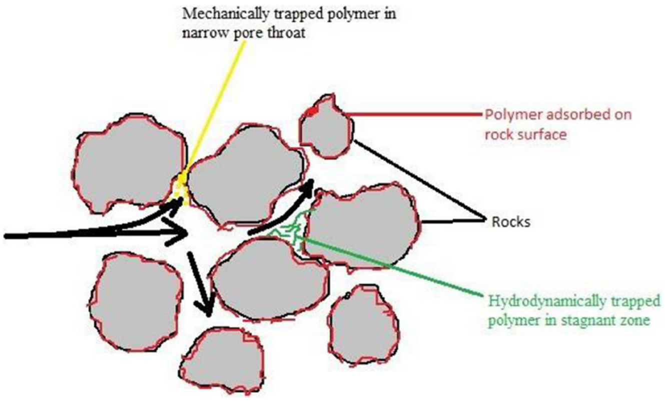

Figure 2.3: Schematic representation of the mechanism of polymer retention [69]

The retention mechanisms of polymers in porous media can be categorised into three factors. The first factor involves the physical interaction between the polymer molecules and the rock surface through hydrogen bonding or Van der Waals forces. The amount of polymer adsorbed is proportional to the available rock surface area. The second factor is the mechanical entrapment of polymer molecules in pores with outlet diameters smaller than the polymer molecule's diameter. In such cases, the polymer molecules become trapped within the pores and cannot flow through. The third mechanism, known as hydrodynamic retention, is influenced by the flow velocity of the polymer solution. After reaching equilibrium in polymer retention, a sudden increase in flow rate leads to additional polymer loss in the porous media due to the trapping of polymer molecules in stagnant flow regions because of hydrodynamic drag forces. Conversely, when the flow rate is reduced or completely stopped, the trapped polymer molecules may diffuse back to the main flow channels, and newly retained polymer molecules will be released [34]. Experiments by Vela et al. (1976) [61] demonstrated an indirect relationship between permeability and polymeric retention. The results showed that as permeability increased from 12 to 137 mD, there was a significant decrease in polymeric retention. In another study by Zaitoun and Kohler (1987) [70], it was reported that there was no significant change in retention when permeability was already high. This suggests that permeability plays a more substantial role as an essential reservoir property at the pore-scale and microscale levels when its values are below 100 mD. However, at higher permeabilities, the influence of permeability on polymeric retention becomes less important [61]. The relaxation time of the polymer is also an important consideration when evaluating oil recovery. As the relaxation time increases, the polymer molecules have more time to stabilise their structure, leading to a more pronounced effect of elasticity on the polymer's behaviour.

2.3. CO_2 Flooding

The CO_2-EOR process aims to recover oil trapped in the reservoir after primary and secondary recovery methods. It involves injecting CO_2 to contact and mobilise stranded oil, thereby improving E_v and E_d. The behaviour of CO_2 during the process depends on reservoir pressure, temperature, and oil properties and can be classified as miscible or immiscible. CO_2 can mix well with the oil (miscible) or remain separate from it (immiscible) when injected. Reservoir conditions and the presence of multiple phases, such as oil or aqueous solutions, influence the behaviour of CO_2. Therefore, a thorough understanding of CO_2 usage for flooding purposes and its behaviour under these conditions is crucial for effectively implementing CO_2-EOR processes.

2.3.1. CO_2 Properties

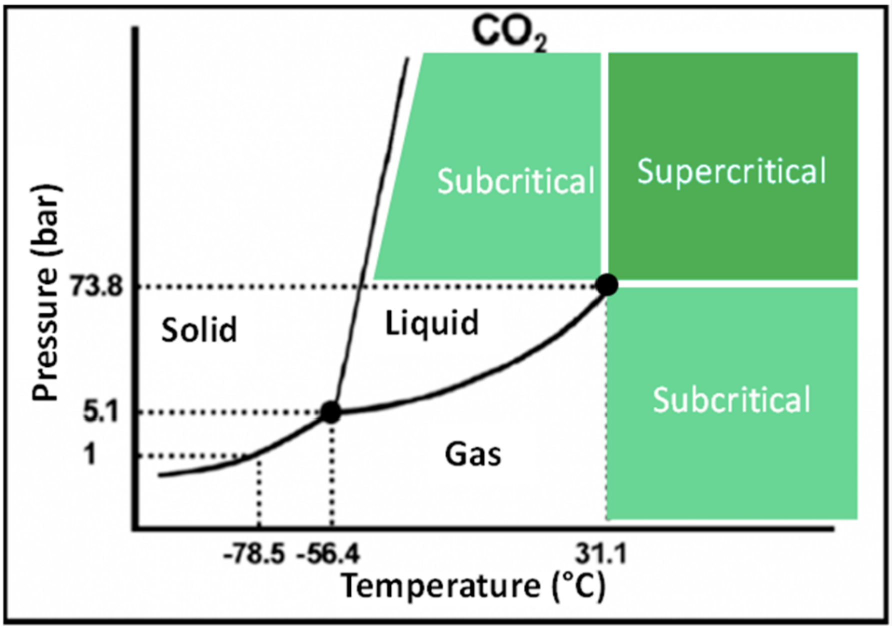

Figure 2.4: CO_2 Phase Diagram [25]

CO_2 is a colourless and odourless gas at atmospheric temperature and pressure. It is approximately 1.5 times denser than air. The critical pressure and temperature of CO_2 are 73.8 bar and 31.1°C, respectively. At these critical conditions, CO_2 exists in a phase where gas and liquid coexist. At higher pressures and temperatures beyond the critical point, CO_2 enters the supercritical state. In this state, the density of CO_2 is similar to that of a liquid, while its viscosity remains relatively low (0.05-0.08 cP). Supercritical CO_2 can extract hydrocarbon components from oil more effectively compared to gaseous CO_2 [25]. This supercritical state of CO_2 is utilised in CO_2-EOR processes. Although the low viscosity of CO_2 can limit its effectiveness in sweeping oil, the dissolution of CO_2 in oil reduces oil viscosity, which aids in improving oil recovery. Liquid CO_2 exists between its critical temperature and pressure and its triple-point temperature (-56.4°C) and pressure (5.1 bar). With its lower viscosity in the supercritical state compared to oil, CO_2 has an unfavourable mobility ratio (Equation 2.1), leading to less effective oil displacement and the formation of viscous fingering (Figure 2.5) through highly permeable layers. This results in an early CO_2 breakthrough at the outlet. Additionally, the lower density of CO_2 compared to oil leads to gravity segregation, placing CO_2 on top of the oil phase along the reservoir's length and causing early CO_2 production at the outlet. These phenomena result in an ineffective areal sweep of the oil in place (OIP) (Figure 2.5).

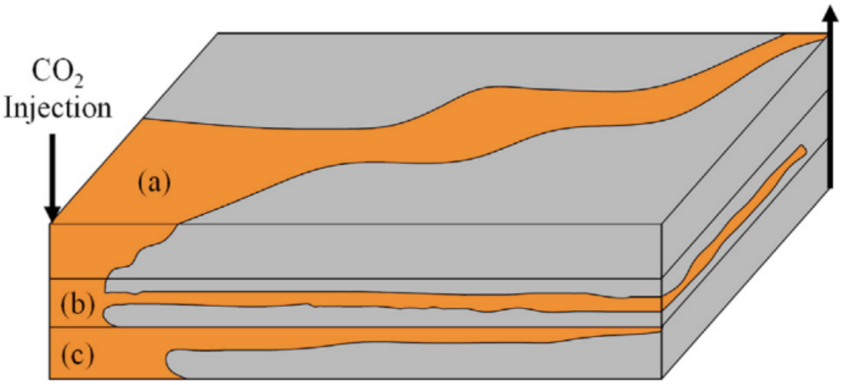

Figure 2.5: Problems caused by high CO_2 mobility in an oil reservoir: (a) poor areal sweep, (b) gas channelling, and (c) gravity override. [31]

2.3.2. CO_2 and Oil

Miscible CO_2 Injection The miscibility of injected CO_2 with oil depends on reservoir pressure, temperature, and oil properties. When the conditions are suitable, the pressure at which CO_2 and oil can mix thoroughly is known as the minimum miscibility pressure (MMP). In 1974, Holm and Josendal [16] defined MMP as the pressure at which more than 80% of the OIP is recovered when CO_2 breakthrough occurs. Recently, the rule-of-thumb for estimating MMP has evolved to consider achieving an oil recovery of at least 90% when injecting 1.2 times the hydrocarbon pore volume (HCPV) of CO_2. This criterion, proposed by Yellig and Metcalfe in 1980 [67], has been commonly used to estimate MMP. Therefore, the miscibility of CO_2 and oil and the determination of MMP play crucial roles in assessing the effectiveness of CO_2 injection for EOR. Oil recovery increases rapidly with increasing pressure, then flattens out when MMP is reached, as shown in Figure 2.6.

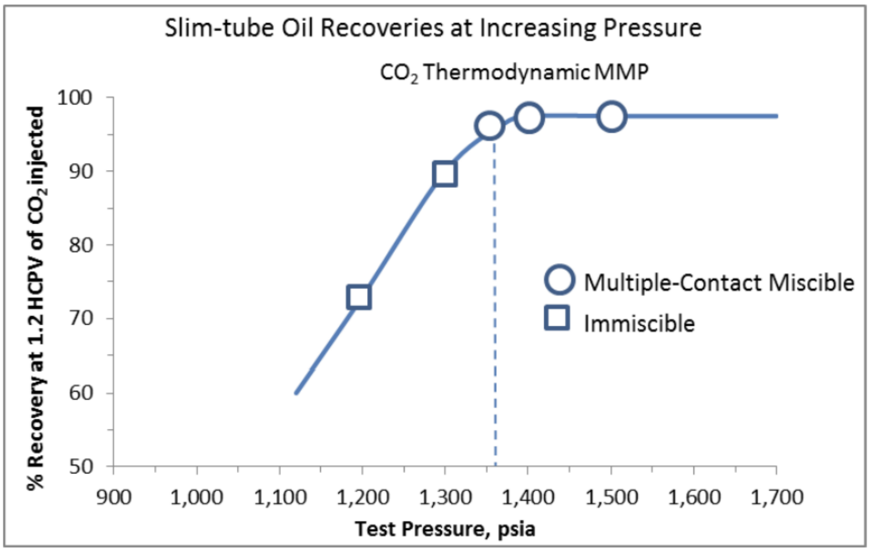

Figure 2.6: Slim-tube oil recoveries at increasing pressures for fixed oil composition and temperatures [67]

Three primary mechanisms for achieving hydrocarbon miscibility exist: first contact, vaporising gas drive, and condensing gas drive [55].

- First-contact miscible solvents mix with reservoir oil in any proportion, resulting in a single-phase mixture. However, solvents like CO_2 are not initially miscible but can develop miscibility with repeated contacts, known as dynamic miscibility. This dynamic miscibility significantly improves oil recovery.
- The vaporising gas drive process achieves dynamic miscibility by vaporising intermediate-molecular-weight hydrocarbons from the reservoir oil into the injected gas or CO_2.
- The condensing gas drive process achieves dynamic miscibility by transferring intermediate-molecular-weight hydrocarbons (or CO_2 in the case of CO_2-EOR) into the reservoir oil.

When the reservoir pressure exceeds the MMP, miscibility between CO_2 and reservoir oil is achieved over time through multiple contacts or dynamic miscibility. In the vaporisation gas drive process, intermediate and higher molecular weight hydrocarbons from the reservoir oil vaporise into CO_2. In contrast, in the condensation gas drive process, part of the injected CO_2 dissolves into the oil. This mass transfer between the oil and CO_2 allows complete miscibility between the two phases without any interface. This development of a transition zone, as illustrated in Figure 2.7, results in a miscible region with oil at the front and CO_2 at the back [32].

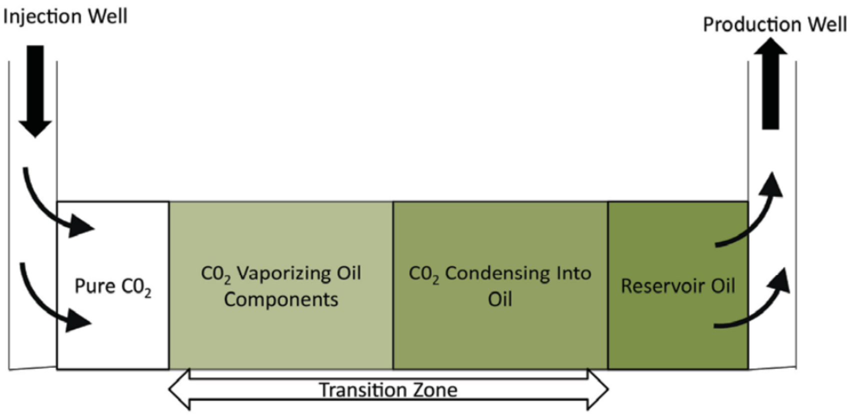

Figure 2.7: The schematic of the CO_2 miscible process shows the transition zone between the injection and production well. [21]

Immiscible CO_2 Injection The experiments modelled in this study were performed at reservoir conditions of 40°C and 20 bar. The experimental pressure during the core-flood experiments was maintained below the MMP for the CO_2/water/n-hexadecane system, as indicated in Table 2.1. Therefore, the experiments were conducted under immiscible conditions, where complete miscibility was not achieved between CO_2 and the other components.

Table 2.1: Minimum miscibility pressures of CO_2 at different pressures for the experimentally retrieved data and computed data, including the temperature condition of 40°C [65]

Temperature (°C)	$CO_2/H_2O/n\text{-}C_{16}H_{34}$ Experiment (MPa)	$CO_2/H_2O/n\text{-}C_{16}H_{34}$ Computed (MPa)
40.3	7.6	8.35
55.4	10.2	10.93
70	13	12.35

When the reservoir pressure is below the MMP or the reservoir oil composition is not favourable, CO_2 and oil will not mix to form a single phase and will not exhibit miscibility. However, CO_2 can still dissolve in the oil, leading to oil swelling and reduced viscosity. These effects improve sweep efficiency and facilitate additional oil recovery. Like hydrocarbon gases, the solubility of CO_2 in oil increases with increasing pressure and decreases with decreasing temperature. This relationship can be observed in Figure 2.8 [49, 64]. The figure demonstrates how changes in pressure and temperature impact the solubility of CO_2 in oil.

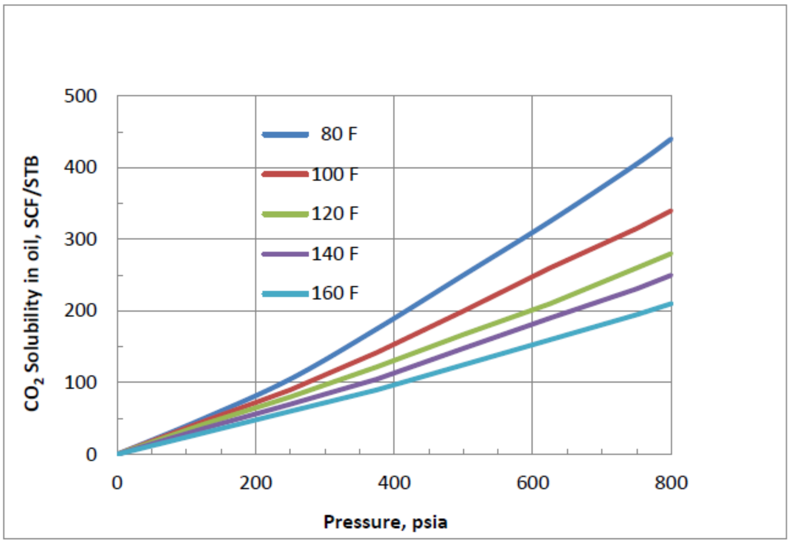

Figure 2.8: Solubility of CO_2 in crude oil from Moran field in Kansas as a function of pressure and temperature [64]

2.4. Polymer Assisted Water Alternating Gas

2.4.1. WAG v/s PA-WAG

WAG is an EOR process that involves the simultaneous or cyclic alternation of drainage (D) and imbibition (I) in the reservoir [39]. Initially, WAG injection was introduced as a means to enhance macroscopic sweep efficiency during gas injection. However, it is now widely applied in matured oil fields to improve recovery by re-injecting produced gas into water injection wells. WAG injection has proven to be an effective method for maximising oil recovery in these fields.

WAG recovery techniques offer a solution to the poor macroscopic sweep efficiency associated with gas injection due to the high mobility of gases [18]. By combining water and gas injection, WAG aims to maximise incremental oil production by utilising gas's high microscopic displacement efficiency and the large macroscopic swept volume achieved through water injection [24]. The simultaneous injection of water and gas shifts from the original oil-water two-phase system to a three-phase oil-gas-water system in the reservoir. During water flooding, the high relative permeability of water and low flow resistance facilitates easy water channelling through the porous medium. However, with the introduction of gas-water alternation, the relative permeability of water is significantly reduced, increasing flow resistance and reducing the likelihood of water channelling [47, 2]. At the same time, the relative permeability of the gas phase decreases compared to gas flooding, enabling better control of gas fingering and stabilising the gas front. This prolonged breakthrough time allows for improved sweep efficiency and overall recovery factor. Reduced residual oil saturation, hysteresis effects, and decreased IFT contribute to additional oil recovery during immiscible WAG injection [44]. Compared to water and oil, the low IFT between gas and oil allows gas to displace oil from small pore spaces that are not accessible to water alone. The co-injection of water and gas leads to gas trapping, mobilising oil at low saturations, and effectively reducing residual oil saturation. Compositional exchanges between the injected fluid and reservoir oil during WAG can also enhance oil recovery by inducing oil swelling and reducing oil viscosity, thereby improving oil mobility [12]. These mechanisms collectively contribute to increased oil recovery during WAG operations.

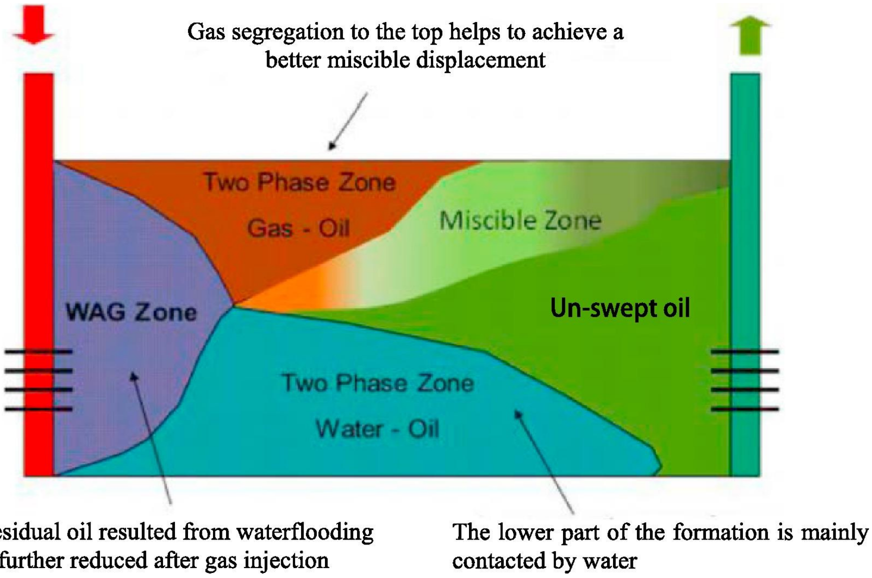

Figure 2.9: Schematic representation of WAG injection in a reservoir [3]

Despite its benefits, the WAG process still experiences limitations due to gravity segregation, particularly in reservoirs with high permeability zones or fractures. This can lead to early breakthroughs of CO_2 and water, leaving a significant portion of the reservoir untouched (Figure 2.9). A novel technique called PA-WAG was introduced to address this challenge and enhance sweep efficiency and oil recovery. The main feature of PA-WAG is that the polymer is injected with water throughout the WAG process.

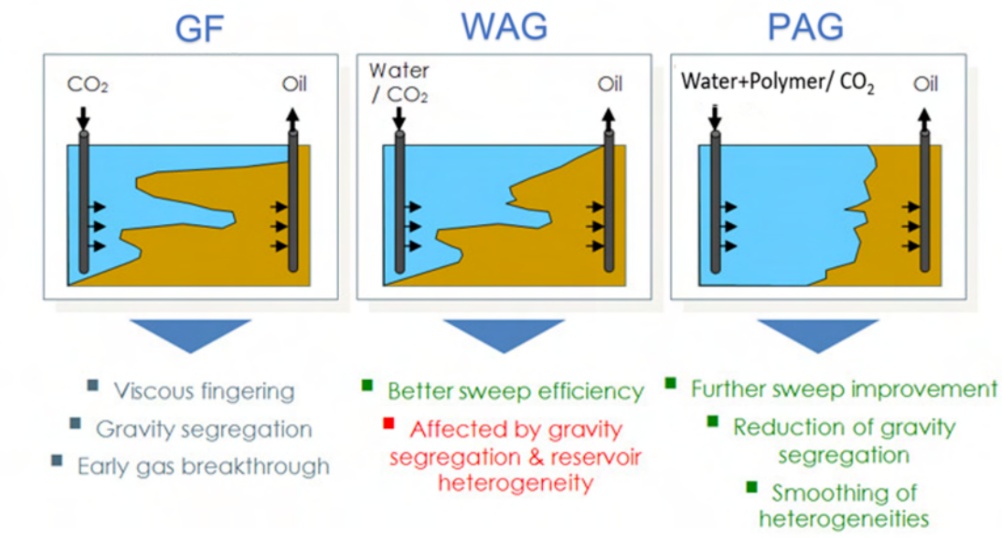

Figure 2.10: Schematic representation of the flooding front of gas flooding, WAG and PA-WAG. Altered from Sajad, Alexander, and Barron (2020) [45]

The PA-WAG method represents a novel approach that combines the advantages of CO_2 flooding (miscible or immiscible) and polymer flooding, resulting in a chemically enhanced WAG flood. By incorporating the solubility of CO_2 injection and the effective mobility control of polymer solutions, PA-WAG offers improved microscopic and macroscopic sweep efficiencies and helps to mitigate gravity segregation issues that can occur in traditional WAG and gas flooding processes. Importantly, the PA-WAG method achieves these benefits while reducing the overall usage of polymers compared to conventional polymer flooding techniques [63]. A recent study by Van Wieren et al. (2022) [65] reported successful implementation of PA-WAG injection, leading to reduced consumption of both CO_2 and water while significantly improving oil recovery.

2.4.2. Effects of CO_2 on Polymer

Understanding the interaction between the polymer and CO_2 phases in the PA-WAG process is crucial for evaluating and predicting its performance.

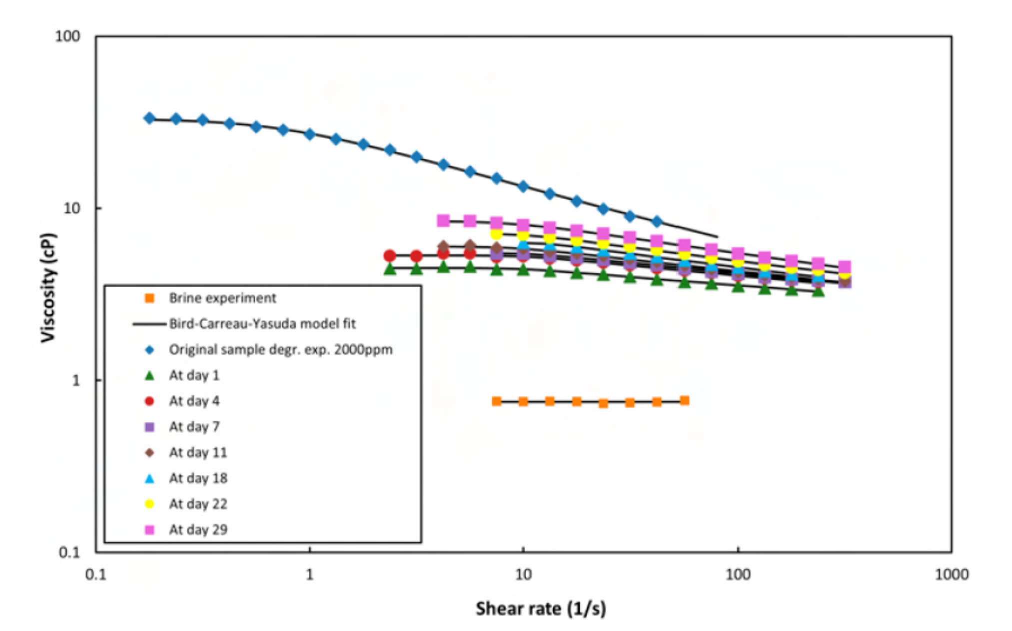

Figure 2.11: Stability of the polymer solution (2000 parts per million (ppm) SAV-10XV) with dissolved CO_2 at 40 °C and 20 bar. The polymer shows a decrease in overall viscosity. Over time, the viscosity recovers [65]

Ageing tests conducted by Tovar, Barrufet, and Schechter (2014) [60] showed that when the PAM-ATBS (Polyacrylamide - Acrylomido Tertiary Butyl Sulfonate) polymer was exposed to CO_2, there was an initial sharp increase in viscosity of around 30% within the first few days. Subsequently, the formation of carbonic acid due to the reaction between water and CO_2 resulted in a decrease in pH and viscosity. After 50 days, the viscosity recovered and stabilised at 104% of its initial viscosity. The low pH conditions induced by carbonic acid in the early stages of ageing promoted the hydrolysis reaction, leading to viscosity recovery. In a more recent study conducted by Van Wieren et al. (2022), [65], using the ATBS(AMPS(2-acrylamido-2-methyl propane sulfonic acid))-modified HPAM polymer SAV-10XV in combination with CO_2 as an EOR technique, it was observed that when the polymer was in contact with fully saturated CO_2 conditions, it experienced a loss in viscosity due to the formation of acids resulting from CO_2 dissolution in water. However, over time, the polymer underwent hydrolysis, catalysed by the acidic pH of the solution caused by carbonic acid. This led to the recovery of the polymer's viscosity, reaching 53.5 ± 5.5% of the initial viscosity at a shear rate of 80 s^{-1} after 29 days of ageing (Figure 2.11). The polymer demonstrated good stability when exposed to lower CO_2 molar concentrations, representing PA-WAG injection conditions. It did not experience a decrease in viscosity with exposure to these CO_2 concentrations and retained 100% of its initial viscosity after four days of ageing. Although the viscosity retained in the presence of CO_2 was slightly lower than that in the presence of nitrogen gas, the usage of CO_2 in the PA-WAG process was preferred due to its higher viscosity and density than nitrogen. However, it is important to note that the initial decrease in viscosity during ageing in CO_2 at reservoir conditions can negatively impact sweep efficiency during the early stages of flooding. To mitigate this, increasing the polymer concentration can enhance viscosity.

3

Methodology

3.1. Summary of Experimental Data

This study's primary source of experimental data is the work conducted by Van Wieren et al. (2022) [65]. Several core-flood experiments were performed on the Bentheimer sandstone cores, but here we will focus on the experiments considered for our work.

3.1.1. Procedure

The experimental procedures are outlined in Table 3.1, providing essential details for each experiment. In experiments, Exp. 1 and Exp. 2, polymer and CO_2 flooding were employed as secondary recovery modes, respectively. Both polymer and CO_2 were injected at the initial oil saturation (S_{oi}) established after the oil injection stage. Subsequently, continuous CO_2 injection followed polymer flooding at the residual oil saturation after polymer flooding ($S_{or,PF}$), and polymer flooding occurred after CO_2 injection at the residual oil saturation after CO_2 injection (S_{or,CO_2}). For experiment Exp. 3, a PA-WAG injection scheme was implemented in six cycles. Each cycle consisted of a polymer slug of 0.22 PVI followed by a CO_2 slug of 1.3 PVI, all at S_{oi}.

Table 3.1: Configuration for all core-flood experiments [65]. PF - Polymer Flood

Step	**Experiment**	**Procedure**	**Back Pressure (bar)**	**Flow Rate (cm^3/min)**	**CT-Scan**
1	All	CO_2 Flusihing	-	-	No
2	All	Vacuuming	-	-	No
3	All	Brine Saturation	20	2	No
4	All	Oil Injection	20	0.5	Yes
5	PF + CO_2 (Exp. 1)	-	20	Polymer: 0.5 , CO_2: 0.5	Yes
	CO_2 + PF (Exp. 2)	-	20	Polymer: 0.5 , CO_2: 0.5	Yes
	PA-WAG (Exp. 3)	-	20	Polymer: 2 , CO_2: 0.5	Yes

In this study, the focus will be solely on the polymer flooding part of Exp. 1 and the CO_2 flooding part of Exp. 2. The primary objective is to gain a deep understanding of the physics and intricacies associated with these individual flooding processes. This knowledge will be the starting point for the subsequent simulation and history-matching of Exp. 3, which involves the PA-WAG injection scheme in the Bentheimer sandstone core. The successful simulation and history-match of Exp. 3 are the main goals of this work, given its more complex nature compared to the previous experiments.

3.1.2. Fluid Properties

The oleic phase used in all experiments was n-hexadecane ($CH_3(CH_2)_{14}CH_3$) doped with 20 wt% 1-iododecane, which was chosen to enhance the CT contrast. The physical properties of this doped oleic phase and the gas phase, brine, and polymer solution utilised throughout the core-flood experiments are presented in Table 3.2. These physical properties play a crucial role in determining the behaviour and interactions of the different phases during the experiments. They are essential inputs for the simulations and history-matching processes.

Table 3.2: Physical properties of fluids used in all experiments reported at 40°C and atmospheric pressure [65].

Fluid	**Density (g/cm^3)**	**Viscosity (cP)**
Shell Brine	1.0184 ± 0.002	0.75 ± 0.02
Polymer Solution 2000 ppm SAV-10XV (15 s^{-1})	1.0256 ± 0.001	11.4 ± 0.2
Polymer Solution 2000 ppm SAV-10XV (60 s^{-1})	1.0256 ± 0.001	6.3 ± 0.2
n-hexadecane <0.0006 wt% Oil Red O 20 wt% 1-iododecan	0.8297 ± 0.001	2.26 ± 0.02
Carbon Dioxide Gas	1.839 ± 0.001 * 10^{-3}	1.46 ± 0.5 * 10^{-2}

All densities and viscosities presented in the table were reported at 40°C and atmospheric pressure. The viscosity of the polymer solution is influenced by its shear thinning behaviour under shear stress. Therefore, the viscosity values are provided at specific apparent shear rates corresponding to the core-flood injection conditions. For the polymer flood injection at 0.5 cm^3/min, the viscosity is given at an apparent shear rate of 15 s^{-1}. On the other hand, for the PA-WAG injection at 2 cm^3/min, the viscosity is provided at an apparent shear rate of 60 s^{-1}.

3.1.3. Core Properties

In this study, the primary material employed as a representative reservoir for the core-flood experiments was well-characterized Bentheimer sandstone. The core sample utilised in the experiments had a length of 17 cm and a diameter of 3.8 cm. The Table 3.3 summarises each core's porosity and permeability values and the calculated pore volume (PV).

Table 3.3: Properties of the Bentheimer sandstone cores used in all the experiments. [65]

Experiment	**Exp. 1**	**Exp. 2**	**Exp. 3**
Injection Scheme	PF + CO_2	CO_2 + PF	PA-WAG
Rock Type	Bentheimer	Bentheimer	Bentheimer
Porosity (%)	23.1 ± 0.10	21.6 ± 0.10	21.9 ± 0.10
Permeability (Darcy)	1.85 ± 0.07	2.69 ± 0.10	2.66 ± 0.10
Length (cm)	17.00 ± 0.10	17.00 ± 0.10	17.00 ± 0.10
Diameter (cm)	3.80 ± 0.10	3.80 ± 0.10	3.80 ± 0.10
PV (cm^3)	44.24 ± 1.20	41.60 ± 1.20	42.22 ± 1.24

3.2. Reservoir Simulator

3.2.1. Overview of the MATLAB Reservoir Simulation Toolbox

MRST-AD is a freely available open-source framework that is an integral part of the MATLAB Reservoir Simulation Toolbox. Its main objective is to facilitate rapid prototyping and experimentation for reservoir simulation problems. The software is divided into two components, as illustrated in Figure 3.1. The relatively compact core module provides data structures and basic routines for configuring, solving, and visualising incompressible single and two-phase models on structured and unstructured grids.

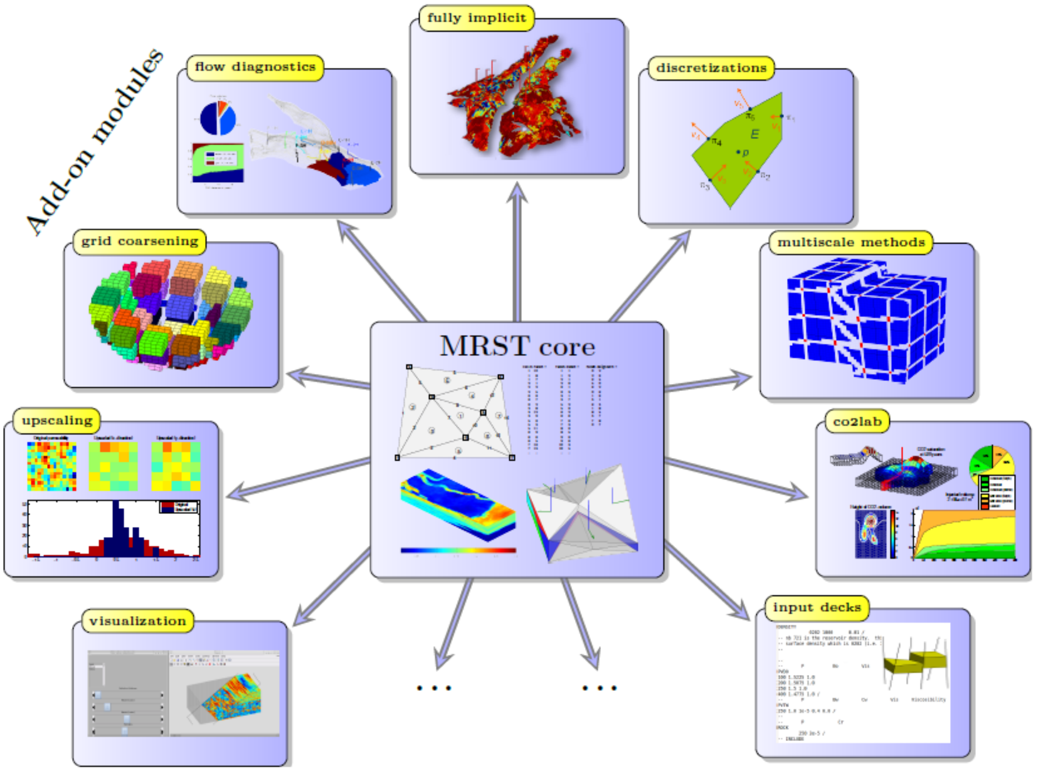

Figure 3.1: MRST is structured with a core module that offers fundamental data structures and simplified solvers. Additionally, it comprises a collection of add-on modules that provide more sophisticated models, solvers, viewers, and workflow tools for advanced simulations [23].

The second part of the MRST-AD software comprises a series of add-on modules that expand, complement, and enhance the functionalities available in MRST-core. Other modules also offer convenient features like reading and processing industry-standard input decks and interactive visualisation tools, among other useful capabilities. Combining the core module and these add-on modules empowers researchers with a comprehensive set of tools for tackling various challenges in reservoir simulation while promoting flexibility and efficiency in their work.

3.2.2. MRST v/s Commercial Simulators

MRST and commercial reservoir simulators offer different features in reservoir simulation. MRST is an open-source framework, providing unrestricted access to its source code for customisation, making it well-suited for academic research. In contrast, commercial simulators are proprietary software with pre-defined features and licensing fees. MRST requires programming knowledge in MATLAB, while commercial simulators have user-friendly interfaces and comprehensive documentation. Commercial simulators offer dedicated support and regular updates, whereas MRST relies on user contributions. MRST is free, making it advantageous for research and education, while commercial simulators undergo validation and obtain industry certifications for real-world applications.

The main objective of MRST is to expedite the period from generating a new idea to demonstrating its viability in realistic reservoir engineering problems. To address the challenges of slow prototyping and validation of mathematical models and computational methods, MRST was introduced as a powerful open-source toolbox written in MATLAB. The framework facilitates rapid prototyping of black oil-type models through automatic differentiation, vectorisation, and abstract operators for spatial discretisations, streamlining the implementation of new models. Additionally, the framework includes state-of-the-art methods for time-step control, preconditioning methods (CPR), and algebraic multigrid solvers for high numerical efficiency. MRST also supports reading and parsing industry-standard input decks describing the reservoir, the wells, and the simulation schedule, enhancing its practicality in realistic scenarios.

3.2.3. MRST Workflow

MRST's functionality is organised into three main modules, each serving a specific aspect of reservoir simulation. The Core Module is central as it provides essential data structures, including grids, petrophysics, wells, and boundary conditions. The Utility Module is another vital component, offering a graphical interface that facilitates interactive visualisation of simulation results. Through visual representations, researchers can analyse and interpret the simulation output, gaining deeper insights into the behaviour of the reservoir. Additionally, this module includes deck format, a tool that simplifies the input of eclipse simulation decks, streamlining the process of integrating external data and setting up simulations. Figure 3.2 gives an overview of how the different modules in MRST are used to implement a fully implicit simulator.

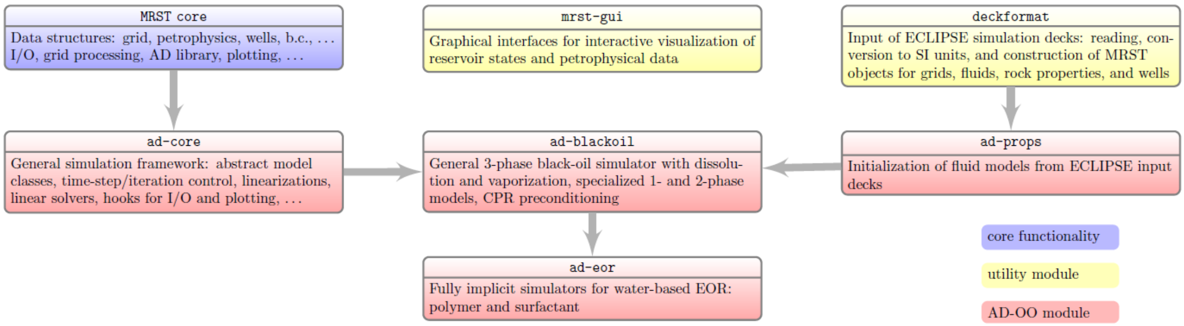

Figure 3.2: Modules from MRST used to implement a fully implicit polymer simulator. [7].

The ad-core module of MRST provides an object-oriented framework known as AD-OO (Automatic Differentiation Object-Oriented), which enables rapid prototyping of new reservoir simulators. This framework simplifies modifying existing simulation models in MRST or creating entirely new models. In MRST versions 2019a and later, the AD-OO framework is further enhanced by introducing state functions and state function groups. These class objects facilitate the evaluation of fluid properties, discretised fluxes, and other crucial properties during flow simulation. State functions in MRST treat the governing equations of a model as an interconnected graph of functions, making it easier to handle spatial variations in functional relationships, variable phases and components, and the redefinition of discrete equations. This streamlined approach enables the implementation of new mathematical equations in a compact form closely aligned with the mathematical formulation. Once the discrete equations are implemented, MRST automatically generates the necessary discretisations and linearisations to create a functional simulator. By default, the simulator is designed to operate on general unstructured grids, enhancing its adaptability to various scenarios. Figure 3.3 gives an overview of how components in the object-oriented AD framework are organised to implement a black oil simulator.

To evaluate the performance of a new simulator, the functionality to read and parse commercial input decks can be utilised and then conduct proper validation on test cases that mirror the real-world complexities encountered in reservoir engineering scenarios. Figure 3.4 demonstrates the function of the input parser.

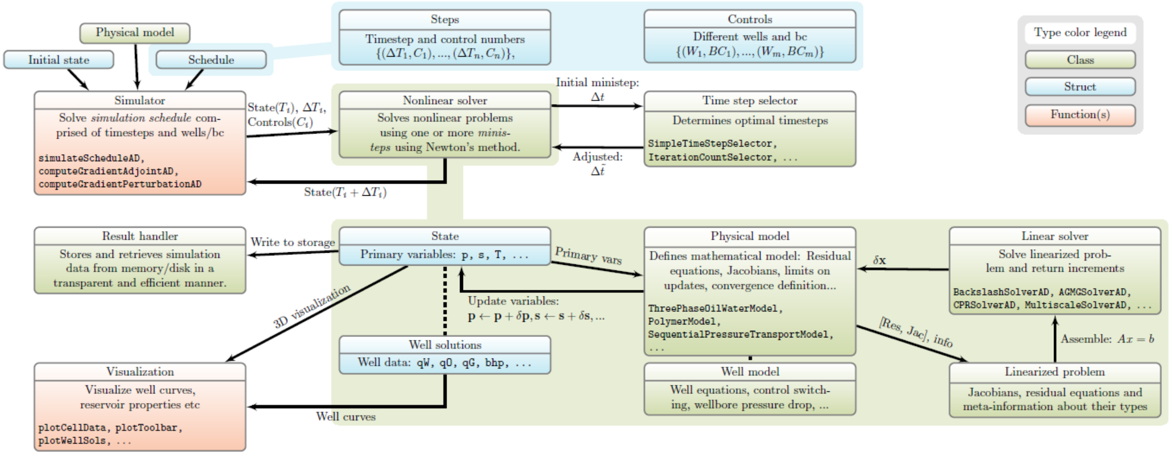

Figure 3.3: The object-oriented AD framework in MRST is structured to efficiently implement a black oil simulator, with different components colour-coded based on their corresponding construct types (classes, structs, or functions) [7].

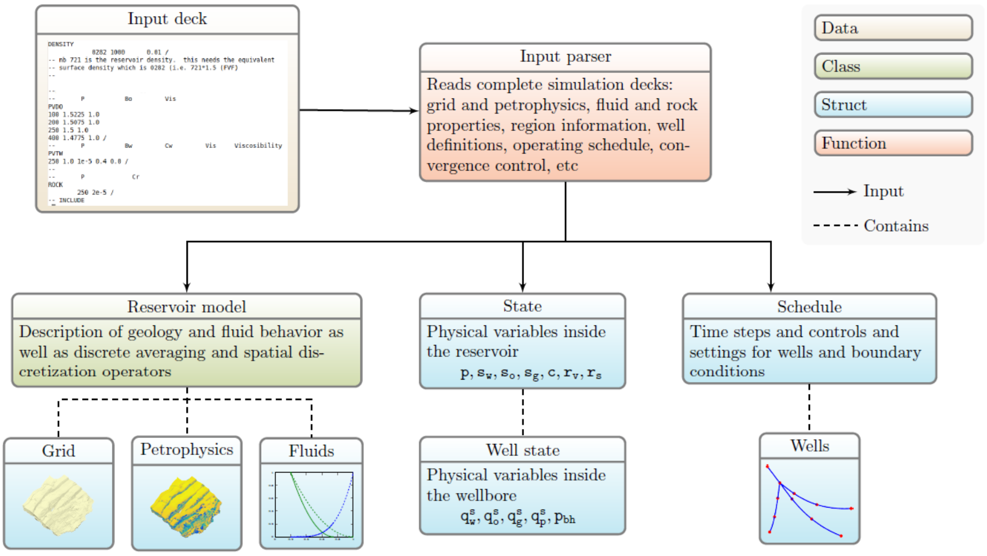

```
DENSITY
            0282 1000      0.01 /
-- nb 721 is the reservoir density.  this needs the equivalent
-- surface density which is 0282 (i.e. 721*1.5 (FVF)
--

--
--       P           Bo         Vis
PVDO
100 1.5225 1.0
200 1.5075 1.0
250 1.5 1.0
400 1.4775 1.0 /
--       P           Bw         Cw          Vis     Viscosibility
PVTW
250 1.0 1e-5 0.4 0.0 /
--
--       P             Cr
ROCK
        250 2e-5 /
-- INCLUDE
```

Reads complete simulation decks: grid and petrophysics, fluid and rock properties, region information, well definitions, operating schedule, convergence control, etc

Description of geology and fluid behavior as well as discrete averaging and spatial discretization operators

Physical variables inside the reservoir

$p, s_w, s_o, s_g, c, r_v, r_s$

Time steps and controls and settings for wells and boundary conditions

Physical variables inside the wellbore

$q_w^s, q_o^s, q_g^s, q_p^s, p_{bh}$

Figure 3.4: The AD-OO framework's input parser allows instantiating data structures for simulations from industry-standard input decks [7].

3.3. The Three-Phase Black Oil Model

The central focus of this study is the three-phase black oil model, which holds a key role, as highlighted in the research objectives. The goal is to use this simple model to simulate complex recovery processes. This section explores the governing equations of the three-phase black oil model, which are the foundation for creating additional modules to simulate polymer flooding, CO_2 flooding, and PA-WAG injection in this study.

The generic black oil Model derived from the three-phase black oil model represents a multicomponent, multiphase flow system without diffusion among fluid components. It assumes hydrocarbon species can be grouped into two components at surface conditions: a heavy hydrocarbon component known as 'oil' and a light component called 'gas.' In reservoir conditions, these components can wholly or partially dissolve in each other, creating a liquid oleic phase and a gaseous phase based on pressure. Additionally, there is an aqueous phase, assumed to be composed solely of water. The continuity equations corresponding to this model are as follows:

$$\delta_t(\phi b_w S_w) + \nabla \cdot (b_w v_w) - b_w q_w = 0 \tag{3.1}$$

$$\delta_t[\phi(b_o S_o + b_g r_v S_g)] + \nabla \cdot (b_o v_o + b_g r_v v_g) - (b_o q_o + b_g r_v q_g) = 0 \tag{3.2}$$

$$\delta_t[\phi(b_g S_g + b_o r_s S_o)] + \nabla \cdot (b_g v_g + b_o r_s v_o) - (b_g q_g + b_o r_s q_o) = 0 \tag{3.3}$$

In this context, the symbol ϕ represents the rock porosity, while S_α refers to the saturation, p_α denotes the phase pressure, and q_α represents the volumetric source of phase α. The user-specified functions of phase pressures include the inverse formation-volume factors b_α, which indicate the ratio between the bulk volumes of a fluid component occupied at surface and reservoir conditions. Additionally, the gas-oil ratio r_s and oil-gas ratio r_v measure the volumes of gas dissolved in the oleic phase and oil vaporised in the gaseous phase, respectively. The phase fluxes v_α are determined using Darcy's law.

$$v_\alpha = -\lambda_\alpha k(\nabla p_\alpha - \rho_\alpha g \nabla z) \ ; \alpha = o, w, g \tag{3.4}$$

In the given context, k represents the absolute permeability of the reservoir rock, while λ_α = $k_{r\alpha}/\mu_\alpha$ denotes the mobility of phase α. Here, $k_{r\alpha}$ represents the relative permeability, and μ_α represents the phase viscosity. The model is completed by assuming that the fluids fully occupy the pore space, satisfying the equation $S_o + S_w + S_g = 1$. Saturation-dependent capillary functions are also provided to establish the relationship between the phase pressures. The equation system comprises three primary unknowns. In the presence of only the aqueous and liquid phases, r_s is chosen, while r_v is chosen when only the aqueous phase is present. When all phases are present, r_s and r_v depend on pressure, and S_g is selected as the final unknown. Appropriate initial and boundary conditions must be specified to form a comprehensive model. In this case, no-flow conditions are assumed at the outer boundaries, and the initial condition is supplied by the user, typically in the form of a hydrostatic pressure and fluid distribution. Additionally, extra well equations are required to compute the volumetric source terms q_α.

$$q_\alpha = \lambda_\alpha W_I (p_w - p) \tag{3.5}$$

In the described reservoir simulation, p represents the reservoir pressure within a grid cell, and p_w represents the pressure within the wellbore. The well index W_I considers various rock properties and geometric factors influencing the flow. The flow inside the wellbore is assumed to be instantaneous, meaning that fluids injected at the surface immediately enter the reservoir. Wells are typically controlled by either surface rates or bottom-hole pressures, and these controls are implemented as extra equations that impose target values for fluid rates and bottom-hole pressures. Operational constraints are also considered, determining the response if computed rates or pressures violate predefined limits. For instance, a well may switch from rate control to pressure control or shut in if hydrocarbon rates become too low.

The three-phase black oil model will serve as the fundamental basis for the simulations conducted in this study. The three-phase black oil model has derived the simulators for modelling different processes, such as polymer flood, CO_2 flood, and PA-WAG. The selection of specific derivatives of the three-phase black oil model will depend on the process under investigation and the composition of phases and components within the system. Detailed explanations of these derivatives is provided in the subsequent sections.

3.3.1. Polymer Flooding Simulator

The polymer model in MRST, known as the generic surfactant polymer model, is based on the extension of the generic black oil model. It is designed explicitly for polymer and surfactant flooding simulations. However, since we are only interested in polymer flooding in this context, we will omit the details of the surfactant properties and solely focus on the polymer part of the model. The model assumes that polymers are transported in the aqueous phase and that the presence of polymers alters the viscosity of this phase, leaving the liquid oleic and gaseous phases unaffected. The corresponding continuity equation for the polymer model is as follows:

$$\delta_t(\phi(1 - s_{ipv}b_w S_w c) + \delta_t(\rho_r c^a(1 - \phi)) + \nabla \cdot (b_w v_p c) - b_w q_w c = 0 \tag{3.6}$$

In the polymer model, the polymer concentration (c) is defined within the range [0, c^*], where c^* represents the maximum possible concentration. The polymer adsorption concentration, denoted by c^a = c^a(c), characterises the interaction between the polymer and the reservoir rock. The density of the reservoir rock is given by ρ_r, and s_{ipv} represents the inaccessible pore volume. To account for the effects of the polymer on the fluid mixture, the model introduces effective mixture viscosities $\mu_{w,eff}$ and $\mu_{p,eff}$, which depend on the polymer concentration. These viscosities play a crucial role in describing the reduced mobility of the mixture of pure water and diluted polymer during the polymer flooding. This gives modified Darcy equations of the form,

$$v_w = -\frac{k_{rw}(S_w)}{\mu_{w,eff}(c)R_k(c)}k(\nabla p_w - \rho_w g \nabla z) \tag{3.7}$$

$$v_p = -\frac{k_{rw}(S_w)}{\mu_{p,eff}(c)R_k(c)}k(\nabla p_w - \rho_w g \nabla z) \tag{3.8}$$

The function R_k(c) captures the phenomenon of reduced permeability experienced by the water-polymer mixture due to polymer adsorption onto the surface of the reservoir rock. It is a non-decreasing function that quantifies the impact of polymer adsorption on the flow behaviour within the reservoir.

In modelling polymer flood, several effective properties are utilised to capture the flow physics involved in the process. These properties are essential for simulating the behaviour of polymers within the reservoir and their impact on fluid flow. The underlying flow physics of these effective properties will be detailed in the following subsections, providing a comprehensive understanding of how these properties contribute to the overall simulation of polymer flooding in the reservoir.

Inaccessible Pore Volume

The faster propagation of polymers through a porous medium compared to an inert chemical tracer dissolved in the polymer solution can be attributed to two main reasons. Firstly, the larger size of polymer molecules restricts their entry into narrow pore throats and dead-end pore channels, limiting their access to certain areas of the reservoir. Secondly, the free-tumbling motion of polymer molecules is feasible only at the centre of the pore channels, away from the surface of the pore walls. As a result, the polymer solution can only flow through a fraction of the total pore space. Equation 3.6 models this effect through the scalar rock parameter s_{ipv}, representing the volume of the pore space that remains inaccessible to the polymer solution.

Polymer Adsorption

The attachment of the polymer to the rock surface occurs through physical adsorption, leading to a reduction in polymer concentration and introducing resistance to flow, which subsequently decreases the effective permeability of water. This adsorption process is assumed to be instantaneous and reversible, and its representation in Equation 3.6 includes the accumulation term $\rho_r c^a(1-\phi)$. The polymer adsorption parameter c^a is modelled using an approach based on Langmuir isotherms, where the adsorbed concentration is a function of the polymer concentration. The specific form of this relationship is:

$$c^a(c) = \frac{a(c - c^a)}{1 + b(c - c^a)} \quad c = min(c, c^*) \tag{3.9}$$

Here, a and b are constants, c^* is the maximum polymer concentration and $c - c^a$ represents the equilibrium concentration in the rock-polymer solution system.

Permeability Reduction

The permeability reduction factor R_k, which accounts for the reduction in the rock's effective permeability to water due to polymer adsorption and the entrapment of polymer molecules in narrow pore throats, is given by the equation:

$$R_k(c, c_{max}) = 1 + (RRF - 1)\frac{c^a(c, c_{max})}{c^a_{max}} \quad ; c_{max}(x, t) = maxc(x, s); s <= t \tag{3.10}$$

The maximum adsorbed concentration is denoted by c^a_{max}, and the RRF is a parameter greater than or equal to 1, defined as the ratio between the brine (water) mobility measured before and after polymer flooding. Both c^a_{max} and RRF are rock-type dependent quantities.

Effective Viscosity

The Todd-Longstaff mixing model is employed to determine the effective viscosities of the water-polymer mixture. This model utilises a mixing parameter, denoted by ω, which ranges between 0 and 1 and represents the degree of mixing of polymer into water. If ω = 1, water and polymer are fully mixed, while ω = 0 indicates complete segregation of the polymer solution from pure water. The viscosity of a wholly mixed polymer solution is represented as μ_{fm} = $\mu_{fm}(c)$. The effective polymer viscosity is computed as follows:

$$\mu_{p,eff} = \mu_{fm}(c)^{\omega} \cdot \mu_p^{1-\omega} \tag{3.11}$$

where μ_p = $\mu_{fm}(c^*)$. The viscosity multiplier, $m_\mu(c)$, is a user-prescribed function used to define μ_{fm}, typically represented as μ_{fm} = $m_\mu(c)\mu_w$. The partially mixed water viscosity is determined similarly as follows:

$$\mu_{pm} = \mu_{fm}(c)^{\omega} \cdot \mu_w^{1-\omega} \tag{3.12}$$

The effective water viscosity is obtained by combining the contributions from the polymer solution and pure water viscosities.

$$\mu_{w,eff} = \frac{m_\mu(c)^{\omega}\mu_w}{1 - c' + \frac{c'}{m_\mu}(c^*)^{1-\omega}} \quad ; c' = c/c^* \tag{3.13}$$

Two-Phase Relative Permeability

When simulating the primary drainage and polymer flood process, the system consists of two phases: oil and water. As a result, each phase ($\alpha = o, w$) experiences an effective permeability $k_{r\alpha}$ that is lower than the absolute permeability k. The presence of another phase introduces additional obstacles to flow. To represent this reduced permeability, the concept of relative permeability is introduced, defined as:

$$k_{r\alpha} = k_\alpha / k \tag{3.14}$$

Where k is the absolute permeability of the rock, and k_α is the permeability to phase $\alpha = o, w$ (for a two-phase system). The two-phase relative permeability for an oil-water system is modelled using the Brooks-Corey equation [8] as follows:

$$k_{row} = (k_{roe})_{S_{wr}}[\frac{S_o - S_{orw}}{1 - S_{orw} - S_{wr}}]^{n_o} \tag{3.15}$$

$$k_{rw} = (k_{rwe})_{S_{orw}}[\frac{S_w - S_{wr}}{1 - S_{orw} - S_{wr}}]^{n_w} \tag{3.16}$$

Here, k_{row} and k_{rw} represent the relative permeabilities of oil and water, respectively. The parameters k_{roe} and k_{rwe} correspond to the end-point relative permeabilities of oil and water, determined from experimental measurements. S_o and S_w denote the oil and water saturations, while S_{orw} and S_{wr} represent the residual oil and water saturation obtained from CT-scan saturation data. The curve shape coefficients, n_o and n_w, are fine-tuned as history-matching parameters.

Capillary Pressure

The Leverett-J function is utilised to compute capillary pressures in the model. It scales the capillary pressure functions based on the rock porosity and permeability. The dimensionless J-function values are used instead of specifying the capillary pressure values in the saturation function tables (using either the SWOF or SGOF keywords in the input deck). Subsequently, the capillary pressure can be calculated using the expression:

$$P_c = J(S_w) \cdot S_f \tag{3.17}$$

where the scaling factor S_f is defined as

$$S_f = ST \cdot \frac{\phi^\alpha}{k^\beta} \cdot U_{const} \tag{3.18}$$

where $J(S_w)$ represents the J-function value, ST is the user-defined surface tension for the oil-water system, ϕ and k are the cell porosity and permeability, respectively, and α and β are the porosity and permeability powers. U_{const} is set to 0.32 for the metric system of units.

The function J needs to be obtained as a tabulated function of S_w by fitting re-scaled observed S_w to a strictly monotone J-shaped function [28]. To set up a multiphase flow simulation, the saturation distribution inside the core is provided with the keyword SWCR and enabling endpoint scaling using the keyword ENDSCALE.

3.3.2. CO_2 Flooding Simulator

Immiscible Gas Injection

The CO_2 flooding simulator is specifically designed to model the CO_2 flooding process. Introducing CO_2 into the system creates an additional gaseous phase, making it suitable to utilise the generic black oil model. The governing equations of the three-phase generic black oil model discussed in section 3.3 will not be reiterated here to maintain conciseness. However, it is essential to note that CO_2 behaves as a gas under experimental conditions, making it unfavourable for a miscible displacement. Consequently, the process is modelled as an immiscible injection with dead oil and dry gas, meaning that the oil does not contain any dissolved gas, and the gas does not contain any vaporised oil. For further reference, Table 3.4 and Figure 3.5 illustrate the relevant properties and conditions.

Table 3.4: Properties of the gaseous, liquid and oleic phases at experimental conditions

Component	Ref. Pressure (bar)	Ref. Temp (°C)	FVF	Viscosity (cP)
Dry Gas (CO_2)	20	40	0.041	0.0146
Dead Oil			1.175	2.28
Water			1	0.73

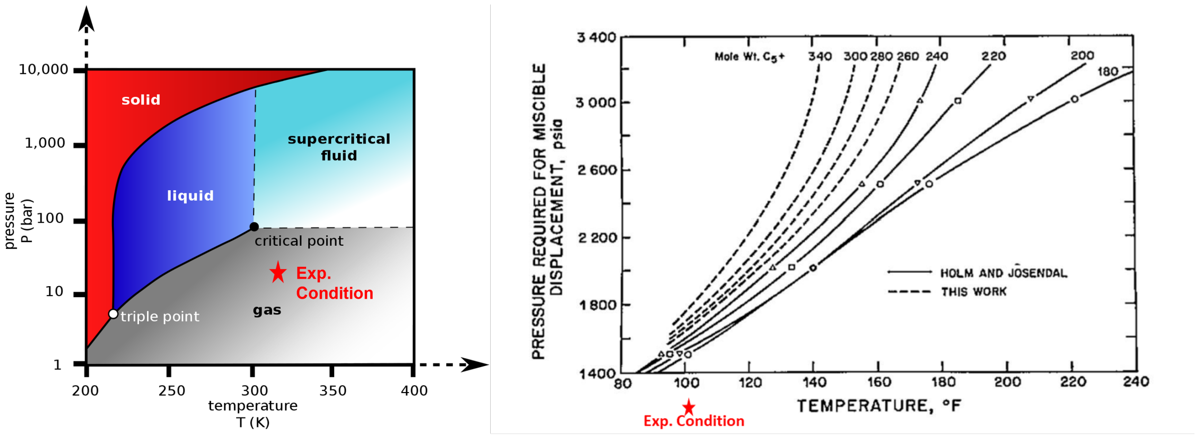

Figure 3.5: Left: Phase diagram of CO_2 showing that it behaves as a gas at the experimental conditions. Right: Plot showing the conditions needed for miscible displacement in CO_2 flooding [36].

Three-Phase Relative Permeability and Capillary Pressure

The default model for calculating three-phase oil relative permeability in MRST shares the fundamental concept with the Stone I model. However, unlike the Stone I model, which utilises a nonlinear relationship to interpolate the two-phase curves, the default model uses a simpler linear relationship. The model assumes complete segregation of water and gas within each cell, leading to the fluid distribution shown in Figure 3.6.

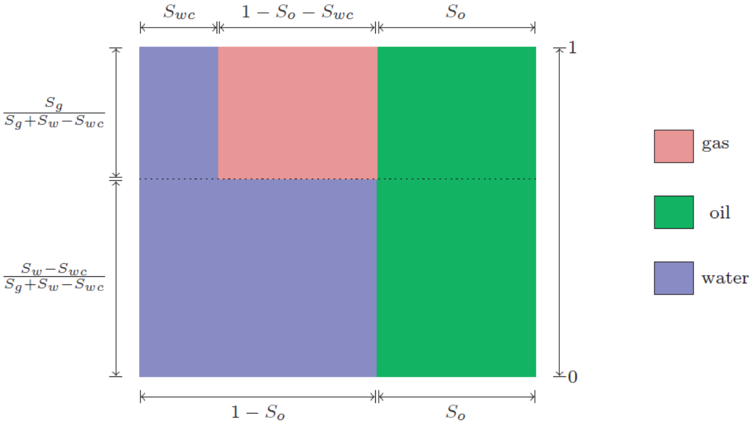

Figure 3.6: Fluid distribution inside each cell assumed by the default method for computing three-phase oil relative permeability in MRST [28].

In the two zones of each cell, the fluid distribution is as follows: In the upper gas zone, oil and gas flow, with oil saturation (S_o), water saturation (S_{wr}), and gas saturation (S_g + S_w - S_{wr}). In the lower water zone, oil and water flow, with oil saturation (S_o), water saturation (S_g + S_w), and gas saturation (0). The three-phase oil relative permeability is then linearly interpolated from the two-phase relative permeabilities [28] using the following equation:

$$k_{ro}(S_g, S_w) = \frac{S_g k_{rog}(S_o)}{S_g + S_w - S_{wr}} + \frac{(S_w - S_{wr}) k_{row}(S_o)}{S_g + S_w - S_{wr}} \tag{3.19}$$

The two-phase relative permeability tables for the oil-water system are generated and provided as input using the relations 3.15 and 3.16. The relative permeabilities in the gas-oil system are calculated using the following Corey type set of relations [4]:

$$k_{rog} = (k_{roe})_{S_{gr}} [\frac{1 - S_g - S_{lr}}{1 - S_{lr} - S_{gr}}]^{n_o} \quad ; S_{lr} = S_{wr} + S_{org} \tag{3.20}$$

$$k_{rg} = (k_{rge})_{S_{wr}} [\frac{S_g - S_{lr}}{1 - S_{lr} - S_{gr}}]^{n_g} \quad ; S_{lr} = S_{wr} + S_{org} \tag{3.21}$$

The relative permeabilities of oil and gas are denoted as k_{rog} and k_{rg}, respectively. k_{roe} and k_{rge} represent the endpoint relative permeabilities of oil and gas. S_{lr}, S_{gr} and S_{org} are the residual liquid, gas and oil saturations in the three-phase system obtained from the CT-scan data. The shape coefficients n_o and n_g are used as history-matching parameters.

In the CO_2 flooding simulator, the capillary pressure is modelled using the Leverett-J function, similar to the approach described in section 3.3.1. However, in this case, the gas-oil surface tension is also considered an additional input to calculate the capillary pressures for the gas-oil system.

3.3.3. PA-WAG Injection Simulator

The PA-WAG injection simulator effectively combines the capabilities of the polymer flooding and CO_2 flooding simulators by utilising the generic surfactant polymer model. As previously mentioned, the generic surfactant polymer model expands upon the three-phase black oil model, incorporating specific equations that accurately represent the flow physics of polymers in the porous media. This feature enables it to simulate three-phase scenarios involving polymers, making it well-suited for modelling the alternating injection of polymer and CO_2 during the oil recovery.

As PA-WAG injection involves a three-phase system, the inputs for relative permeability and capillary pressure follow a similar process to the ones described in section 3.3.2. However, implementing them in the PA-WAG injection simulator is more intricate than the CO_2 flooding simulator. The reason is the alternating cycles of gas and polymer injections, which lead to gas trapping and hysteresis, requiring adjustments to the relative permeabilities during different cycles. This necessitates running segmented simulations to model the PA-WAG process accurately. Further details about the segmentation and its impact will be discussed in sections 3.4.5 and 4.4.

3.4. Core-Flood Simulations

This section details the methodology implemented in setting up the grid and selecting the input parameters for the simulations in this study. As stated in previous chapters, the numerical simulation tool used for the analysis was MRST. All the matches were developed under a 2-Dimensional (2D) configuration. For primary drainage and polymer flooding, a two-phase scheme was preferred. Once the CO_2 flooding was implemented, an additional gas phase was involved. Finally, the three-phase generic surfactant polymer model built upon the generic black oil model included in MRST was used to analyse the PA-WAG injection scheme where the alternate injection of polymer and CO_2 was implemented as an EOR technique.

3.4.1. Grid Setup

A 2D grid was established using CT-scan data in all experiments. The initial step in setting up this grid involved considering a 1-Dimensional (1D) displacement along the horizontal (x-direction) of the core's length. The number of grid cells in this direction varied depending on the resolution of the CT scan employed. For Exp. 1, the CT scan had a resolution of 2 mm. This resolution resulted in 81 available data points considering an average core length of 16 cm. In contrast, Exp. 2 and Exp. 3 utilised a higher resolution of 0.6 mm. Consequently, with an average core length of 16.5 cm, these experiments had access to 275 data points. However, while all the data points were utilised for Exp. 1, a decision was made in the case of Exp. 2 and Exp. 3 to balance the grid configuration regarding simulation time and quality. The grid was coarsened by selecting a ratio of 3 original fine cells per coarse cell in the x-direction to achieve this. As a result, Exp. 2 had 92 coarse cells, while Exp. 3 had 91 in the x-direction.

To generate the 2D grid, the ImageJ software was employed in the subsequent step. For each CT slice image, 17 cells were drawn perpendicular to the core's length in the z-direction. This approach ensured coverage of the core's maximum cross-sectional area. This procedure was repeated for all the images in sequence, ensuring the construction of the 2D grid structure for each core. Details about the specific steps implemented in ImageJ can be found in appendix A. Figure 3.7 illustrates the distinction between a fine cell, which represents the initial discretisation of the CT scan, and a coarse cell, which is a cluster of fine cells used for scaling purposes along the core section. Additionally, the figure showcases the overlay of the grid on the CT image, demonstrating the process of obtaining the 2D grid.

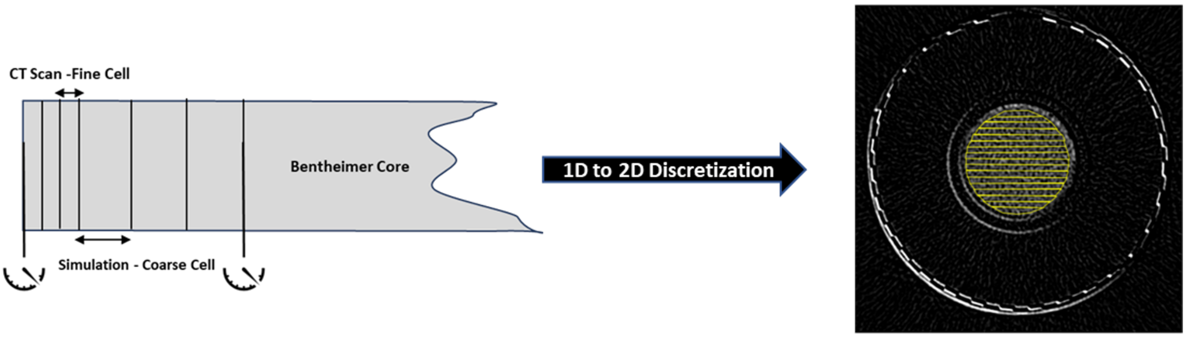

Figure 3.7: Left: Relationship between the core section, fine and coarse cells. Right: Vertical Grid Overlay on the CT image used to transform the 1D grid to 2D.

Table 3.5 summarises the grid configuration for each experiment. The total PV was calculated considering the porosity estimation in the coarse grid, resulting in a slightly different value compared to the reported PV. However, this difference is acceptable given the inherent uncertainty, also reported in Table 3.3. The subsequent Pore Volumes Injected (PVI) values were also recalculated to maintain consistency. It was observed that the variation between the recalculated PVI and the reported PVI is not significant.

Table 3.5: Grid Properties for all the experiments

Experiment	Number of Cells (x,y,z)	Δx (m)	Δy (m)	Δz (m)
Exp. 1	81,1,17	0.0020	0.038	0.0022
Exp. 2	92,1,17	0.0018	0.038	0.0022
Exp. 3	91,1,17	0.0018	0.038	0.0022

After discretising the grid, porosity values were obtained for individual fine cells using ImageJ. To determine the porosity at the coarse cell level, the arithmetic average of the porosity values of the corresponding fine cells was calculated for each coarse cell. Similarly, permeability values were determined for each fine cell and then averaged to obtain the permeability at the coarse cell level. The permeability was calculated as a function of porosity using the Carman-Kozeny relation [10]. The Carman-Kozeny relation correlates porosity and permeability in fluid flow through porous media.

$$k = \frac{{D_p}^2 \phi^3}{\alpha(1-\phi)^2} \tag{3.22}$$

In the mentioned expression, D_p represents the average grain diameter, which was determined as 0.27 mm based on the study by Peksa et al. (2015) [41]. The constant factor α is specific to each core section and depends on its properties. The value of α for each core section was determined using Equation 3.22. This step involved calculating the porosity as the average porosity of the fine cells within each core section. On the other hand, the absolute permeability to brine for each core was obtained during the experiments. This was accomplished by measuring the flow rates, the pressure drop across the core, and utilising Darcy's law,

$$q_w = \frac{Ak}{\mu_w} \nabla P \quad ; \quad \nabla P = \frac{\Delta P}{\Delta l} \tag{3.23}$$

Where k is the absolute permeability, A is the cross-sectional area of the core, q_w and μ_w the water injection rate and viscosity, and ∇P, ΔP and Δl the pressure gradient, pressure differential and length of the core, respectively. Figure 3.8 shows the 2D grid structure populated with the porosity and permeability values for Exp. 3. Similar porosity and permeability maps were obtained for Exp. 1 and Exp. 2 can be visualised in figures B.1 and B.3 in appendix B.

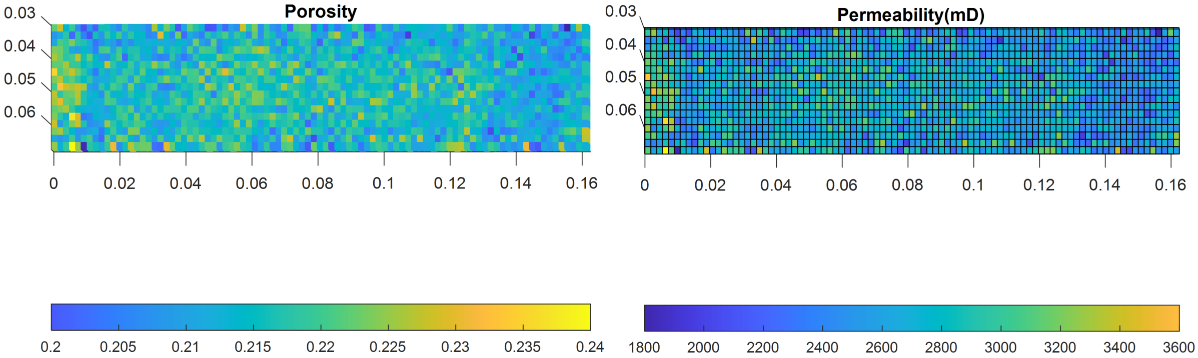

Figure 3.8: 2D Grid consisting of 91 and 17 grid cells in the x and z directions, respectively, populated with porosity and permeability, representing the Bentheimer sandstone core in Exp. 3. Grid coarsening is applied in the x-direction by selecting a ratio of 3 fine cells per coarse cell, reducing 272 discrete CT slices to 91 grid cells

3.4.2. Simulation of Primary Drainage

The simulation of the primary drainage process consists of only two phases: The liquid oleic and aqueous phases. Consequently, the generic black oil model derived from the three-phase black oil model in MRST is employed to simulate this process. Identifying the correct relative permeability curves is crucial for the success of the primary drainage and subsequent flooding stages. Figure 3.9 showcases the relative permeability curves for water and oil during the primary drainage phase in Exp. 3. These curves offer valuable insights into the relative permeability behaviour of water and oil as a function of water saturation levels, enabling a better understanding of fluid flow dynamics within the core sample. The primary drainage relative permeability curves for Exp. 1 and Exp. 2 are represented in Figures C.1 and C.5 in appendix C.

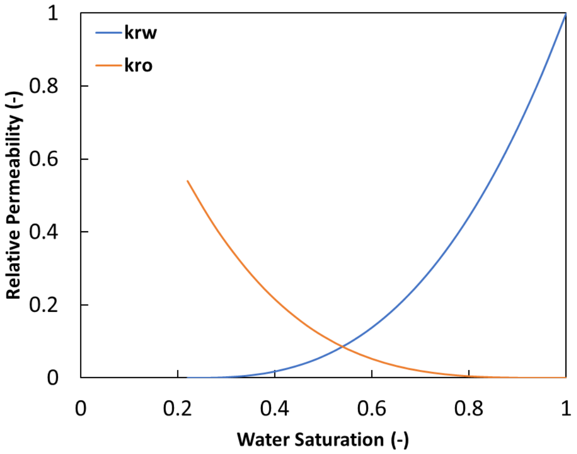

Figure 3.9: Relative Permeability curves for the primary drainage stage in Exp. 3. k_{rw} and k_{ro} represent the water and oil relative permeability curves, respectively.

Table 3.6 summarises the relative permeability parameters for primary drainage in all the experiments. S_{wr} values were determined for each experiment based on the CT-scan saturations. On the other hand, the end-point relative permeabilities used in the simulations were obtained from the permeability tests conducted during the experiments. It is crucial to highlight that the end-point relative permeabilities denote the values obtained at the maximum saturation of the respective phases observed during the experiments rather than the values at 100% phase saturations.

Table 3.6: Primary drainage relative permeability parameters for Exp. 1, Exp. 2 and Exp. 3. S_{wr} values were determined for each experiment based on the CT-scan saturations. In contrast, the end-point relative permeabilities were obtained from the permeability tests conducted during the experiments.

Parameter	Exp. 1	Exp. 2	Exp. 3
S_{wr}	0.249	0.300	0.219
S_{orw}	0.000	0.000	0.000
k_{rwe}	1.000	1.000	1.000
k_{roe}	0.570	0.570	0.540
n_w	2.700	2.700	2.750
n_o	5.700	2.900	3.500

In addition to relative permeabilities, two other crucial parameters required for a successful history match are the initial water saturation distribution (S_{wi}) and capillary pressures. Before the primary drainage stages, the core is completely saturated with brine; thus, S_{wi} is assumed to be 100%. For subsequent stages, the initial saturation distribution is determined by the final saturation distribution output obtained from the simulation of the previous stage. This ensures a continuous simulation process that accounts for the saturation changes over time. To calculate the capillary pressures, the Leverett-J function is implemented, as discussed in section 3.3. The function J is obtained by fitting the re-scaled observed data (S_w) to a strictly monotone J-shaped function, typically represented as a tabulated function of S_w. This function characterises the capillary pressure-saturation relationship and is essential for accurate multiphase flow simulation. The CT-scan-based S_w distribution at the end of the primary drainage stage within the core is provided using the SWCR to incorporate the capillary end effect in the simulation results. The SWCR keyword defines the critical water saturation, the highest water saturation at which each grid cell's relative permeability becomes zero. Calculating water flow across each grid face involves using a transformed water relative permeability curve. This curve is created by linearly scaling the tabulated relative permeability data between the newly defined critical water saturation based on the SWCR keyword and the new maximum water saturation. The scaling feature is enabled using the keyword ENDSCALE. This approach ensures the inclusion of the capillary end effect, which is important for capturing the behaviour of fluid displacement and redistribution within the reservoir during subsequent simulation stages. The input parameters for simulating the primary drainage phase in all the experiments are summarised in Table 3.7.

Table 3.7: Summary of primary drainage input parameters for experiments Exp. 1, Exp. 2 and Exp. 3. The densities, viscosities, and flow rate were derived from experimental data. The porosity and permeability values presented in this table represent the average of the respective individual grid cell values used in the simulation

Parameter	Exp. 1	Exp. 2	Exp. 3
Simulation Time (PVI)	5		
Initial Water Saturation	S_w=1		
Porosity (ϕ_{avg})	0.23 ± 0.0036	0.21 ± 0.0071	0.215 ± 0.0047
Permeability (k_{avg})	1820.5 ± 102.11	2711.1 ± 313.15	2651.6 ± 204.8
Density - Oil / Water (kg/m^3)	829.7 / 1018.4		
Viscosity - Oil / Water (cP)	2.28 / 0.73		
Oil Injection Rate (m^3/day)	0.00072		

3.4.3. Simulation of Polymer Flooding

With the inclusion of the polymer in the system, the generic surfactant polymer model of MRST is used to simulate the polymer flood process. As explained in section 3.3.1, MRST considers the effect of polymer injection by modifying the viscosity of the aqueous phase using the viscosity multiplier parameter. This parameter is a function of the polymer concentration at any given time. Consequently, the relative permeability curves used for the polymer flooding process in the simulation resemble a typical waterflood (forced imbibition) process in a water-wet Bentheimer sandstone core. These relative permeability curves are modified using polymer-specific parameters during the simulation run, detailed later in this section. These adjustments adequately represent the polymer's impact on the flow behaviour during the flooding process. Figure 3.10 illustrates the relative permeability curves used for the polymer flooding process in Exp. 1.

In addition to utilising accurate relative permeability curves, it is crucial to scale them based on the critical water and oil-in-water saturations obtained from the CT scans. This scaling process is achieved using the ECLIPSE keywords SWCR (for critical water saturation) and SOWCR (for critical oil in water saturation), along with enabling endpoint scaling. By implementing this approach, the relative permeabilities are adjusted to properly account for the observed capillary effects within the core samples. Furthermore, as discussed in previous sections, it facilitates the accurate calculation of capillary pressures using the Leverett-J function.

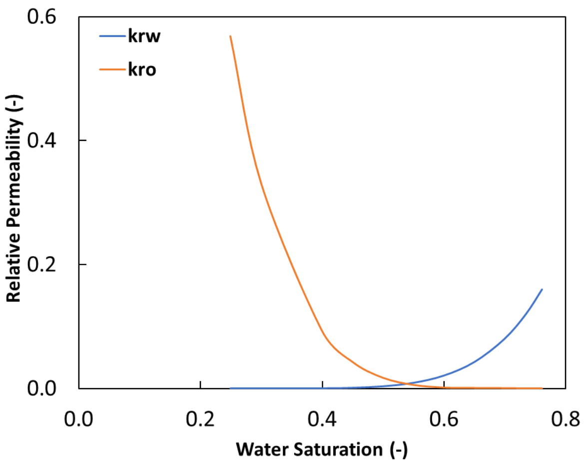

Figure 3.10: Relative Permeability curves for the polymer flood, Exp. 1. k_{rw} and k_{ro} represent the water and oil relative permeability curves, respectively. The relative permeability of water is modified upon the addition of polymer using the polymer-specific parameters.

Table 3.8 summarises the relative permeability parameters for the polymer flood process in Exp. 1. S_{wr} values were determined for each experiment based on the CT-scan saturations. The end-point relative permeability for oil was obtained from the permeability tests conducted during the experiments. However, it is worth noting that the measurement of the end-point relative permeability of water/polymer was affected by the formation of emulsions towards the end of the experiment, rendering it unsuitable for direct use. To address this limitation, a decision was made to use a value for the end-point relative permeability of water based on an extensive literature review of the waterflooding process in a water-wet Bentheimer core. The literature provided a range of values between 0.13 and 0.18 [19, 42, 40, 30]. These values were determined through steady-state two-phase relative permeability tests, considered more reliable than unsteady-state tests, and extensive simulation results in these studies supported them. For this work, a value was selected within that range to match the experimental data well. It is crucial to highlight that the end-point relative permeabilities denote the values obtained at the maximum saturation of the respective phases during the experiments rather than the values at 100% phase saturations.

Table 3.8: Polymer Flood relative permeability parameters for Exp. 1. The end-point relative permeability of water during the waterflooding process in a water-wet Bentheimer sandstone is employed because the formation of emulsions adversely impacted the experimental measurements for polymer end-point relative permeability.

Parameter	**Exp. 1**
S_{wr}	0.249
S_{orw}	0.238
k_{rwe}	0.160
k_{roe}	0.570
n_w	5.400
n_o	5.700

The most critical parameters for history matching Exp. 1 are the polymer-specific parameters summarised in Table 3.9. All these polymer-specific parameters, except for the RRF, were available from the experiments. The RRF was utilised as a history-matching parameter to improve the simulation's agreement with the experimental data. The IPV was determined using the measured radius of gyration from the experimental data, and further information about these calculations can be found in appendix D. Only a single value at a concentration of 2000 ppm was available for polymer adsorption from the experiments. To account for adsorption at various concentrations, a correlation was constructed using data from the literature on a similar HPAM polymer [68]. This correlation allowed for the estimation of adsorption values at different concentrations and facilitated the construction of a Langmuir-type isotherm for the simulations. The Langmuir-type isotherm, as seen in Figure 3.11, characterises the adsorption behaviour of the polymer.

Table 3.9: Summary of input parameters for polymer flood, Exp. 1. All polymer parameters are determined from experiments except for RRF, which is used as a history-matching parameter.

Parameter	Exp. 1
Simulation Time (PVI)	5
Initial Water/Oil Saturation	Saturation distribution output of primary drainage stage
Density - Oil / Polymer (kg/m^3)	829.7 / 1025.6
Viscosity - Oil / Polymer (cP)	2.28 / 11.68
Polymer Injection Rate (m^3/day)	0.00072
Polymer Viscosity Multiplier	16
IPV	0.25
RRF	3.4
Max. Adsorption (kg/kg)	9.96E-05
Max. Polymer Conc. (kg/m^3)	2
Mixing Parameter	1

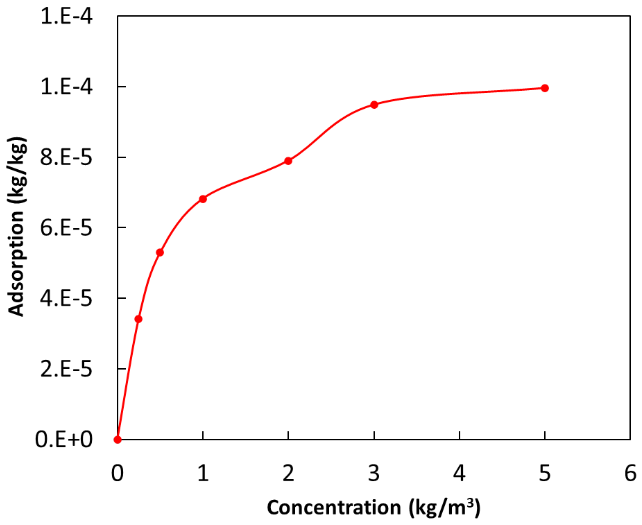

Figure 3.11: Langmuir-type isotherm for polymer adsorption in Exp. 1 derived from the work of Yerramilli et al. (2013) [68] on HPAM polymers.

3.4.4. Simulation of CO_2 Flooding

The simulation of the CO_2 flooding process introduces an additional gaseous phase into the system. The generic black oil model of MRST is utilised to history-match this process. Including the gaseous phase leads to a three-phase system, which necessitates the input of an additional gas-oil relative permeability curve in addition to the water-oil relative permeability. To estimate the three-phase relative permeabilities, a process of transforming the two-phase relative permeability curves was followed, as detailed in section 3.3.2. This transformation accounts for the interactions among the three phases in the system, enabling a more comprehensive representation of fluid flow behaviour during the CO_2 flooding process. Figure 3.12 illustrates the relative permeability curves for the water-oil and gas-oil systems.

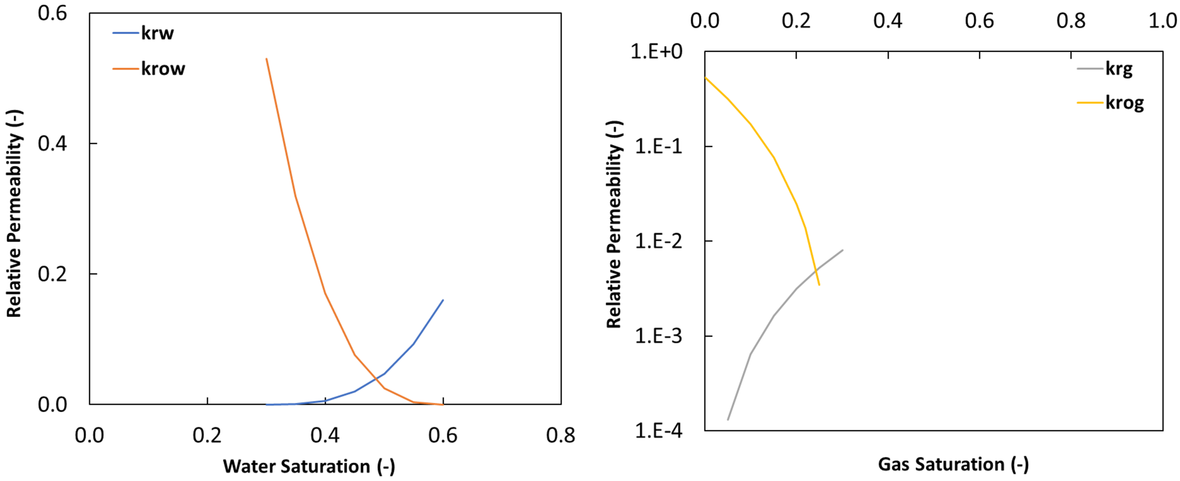

Figure 3.12: CO_2 Flood Relative Permeability curves for water-oil (left) and gas-oil (right) systems, Exp. 2. k_{row} and k_{rog} represent the oil in water and oil in gas relative permeabilities, whereas k_{rw} and k_{rg} are the relative permeabilities of water and gas. Due to the S_{lr} of 0.7, the experiments are constrained, and the maximum gas saturation achieved is limited to 0.3.

Table 3.10 summarizes the relative permeability parameters for the CO_2 flooding process in Exp. 2. The residual saturation values were determined for each experiment based on the CT-scan saturations. The end-point relative permeability for oil was obtained from the permeability tests, while the ones for water during the imbibition process as described in 3.4.3 were used. However, the experiment did not provide the gas end-point relative permeability measurements. Therefore, a value was selected based on data found in the literature on immiscible gas flooding in the Bentheimer sandstone core. These values were observed to be in the range of 0.02 to 0.08 [19, 5, 22]. As stated in previous sections, the end-point relative permeabilities refer to the relative permeabilities values obtained at the highest phase saturations (oil, water, gas) achieved during the experiments rather than at 100% phase saturations.

Table 3.10: CO_2 flood relative permeability parameters, Exp. 2. Since there were no end-point relative permeability measurements for gas, its value was determined based on literature focusing on immiscible gas flooding in Bentheimer sandstone [19, 5, 22].

Parameter	S_{wr}	S_{orw}	S_{org}	S_{gr}
	0.300	0.400	0.400	0.000
Parameter	k_{rwe}	k_{rowe}	k_{rge}	k_{roge}
	0.160	0.530	0.010	0.530
Parameter	n_w	n_{ow}	n_g	n_{og}
	3.000	2.800	2.300	2.800

In addition to the relative permeability curves, the saturation distribution output from the primary drainage stage is used as input for the CO_2 flood simulation. To scale the relative permeability curves and capillary pressure, the critical water and oil in gas saturations are input using the SWCR and SOGCR keywords, respectively. During all the experiments, a mass flow controller was utilised for CO_2 injection, which required converting the desired flow rate in cm^3/min of CO_2 to mL/min of CH_4. These converted flow rate values were used as input for the simulation. However, before reporting the PVI in the results, these values were converted back to their original flow rate values. The final input parameters for the CO_2 flood simulation are summarised in Table 3.11

Table 3.11: Summary of input parameters for CO_2 flood, Exp. 2. All simulation parameters were established using experimental measurements as the basis.

Parameter	Exp. 2
Simulation Time (PVI)	5
Initial Water/Oil Saturation	Saturation output of primary drainage stage
Density(Oil/Water/Gas) (kg/m^3)	829.7 / 1018.4 / 1.839
Viscosities ((Oil/Water/Gas) (cP)	2.28 / 0.73 / 0.0146
Gas Injection Rate (m^3/day)	0.0142

3.4.5. Simulation of PA-WAG

The PA-WAG simulation utilises the generic surfactant polymer model, involving six injection cycles with alternating polymer and CO_2 injections. Initially, a single set of relative permeability curves was used for all cycles, leading to unsatisfactory history-matching results. The simulation runs were divided into segments to address this issue, with each cycle modelled separately using independent relative permeabilities. The saturation distribution from the previous cycle served as input for the subsequent one, ensuring continuity in the injection process and a more accurate representation of the fluid flow behaviour. To address the phenomenon of gas trapping and its influence on the polymer injection process, the initial two cycles were subdivided into half-cycles of polymer and CO_2 injections. These segments were independently simulated during the initial two injection cycles, employing distinct relative permeability curves for each half-cycle. Figure 3.13 illustrates the gas-oil and water-oil relative permeability curves employed in these initial cycles, with a decrease in gas relative permeability from cycle 1 to cycle 2, reflecting the gas trapping effect. Table 3.12 lists the relative permeability curve parameters. The complete set of relative permeability curves used in each cycle can be found in the appendix F.

In addition to employing reduced relative permeabilities, the simulation incorporated gas saturation data obtained from CT scans after polymer injection in the second cycle. This gas saturation data was utilised to estimate the trapped gas within the reservoir. To incorporate this information into the model, the SGCR keyword was employed, which scales the gas relative permeability curves in each grid cell based on the critical gas saturation. The critical gas saturation represents the gas saturation threshold at which the trapped gas begins to affect the relative permeability of gas in the reservoir.

During the simulation of each cycle, all other polymer and CO_2 related parameters were handled in a manner similar to how they were used independently in the simulation of the respective processes. The details of these parameters and their specific application for each cycle can be found in appendix E.

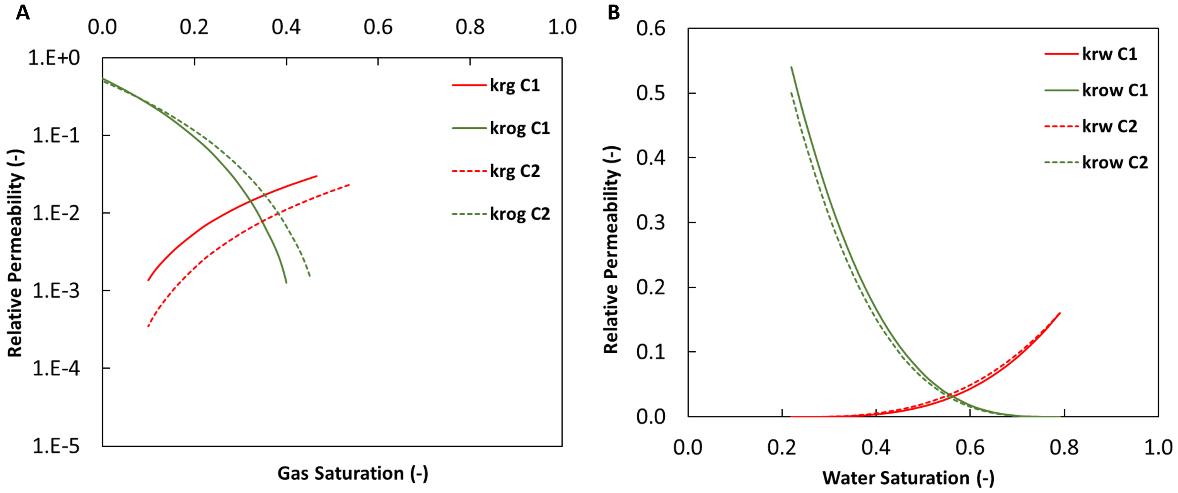

Figure 3.13: (A) Decreasing gas relative permeability from cycle 1 to cycle 2 due to gas trapping, Exp. 3. (B) Water-oil relative permeability for cycle 1 and cycle 2, Exp. 3. C1 and C2 denote the first and second cycles, respectively.

Table 3.12: PA-WAG relative permeability parameters for Exp. 3. Cn represents the cycle number. No gas-specific parameters are utilised during the simulation of C1 - Polymer, as gas is only introduced into the system during the simulation of C1 - CO_2.

Parameter	C1 - Polymer	C1 - CO_2	C2 - Polymer	C2 - CO_2	C3	C5	C6
S_{wr}	0.22	0.22	0.22	0.22	0.22	0.22	0.22
S_{orw}	0.21	0.21	0.21	0.21	0.21	0.21	0.21
S_{org}	-	0.314	0.245	0.234	0.226	0.22	0.22
S_{gr}	-	0.0	0.0	0.0	0.0	0.0	0.0
k_{rwe}	0.16	0.16	0.16	0.16	0.16	0.16	0.16
k_{rge}	-	0.03	0.023	0.023	0.03	0.03	0.03
k_{roe}	0.54	0.54	0.50	0.50	0.50	0.50	0.50
n_w	3.20	3.20	2.90	1.70	3.75	3.00	2.65
n_g	-	2.00	2.50	2.50	2.60	2.60	2.60
n_o	3.10	3.10	3.15	1.95	3.80	3.05	2.70

4

Simulation Results and Discussion

The history-matching procedure for Exp. 1, Exp. 2 and Exp. 3 included simulating the primary drainage process to determine the initial distribution of oil and water in each experiment. These saturation values were subsequently utilised as inputs for the following stages to simulate the oil recovery process. The results of this process are presented and discussed in this chapter. Figure 4.1 summarises the simulated flooding sequence for each experiment.

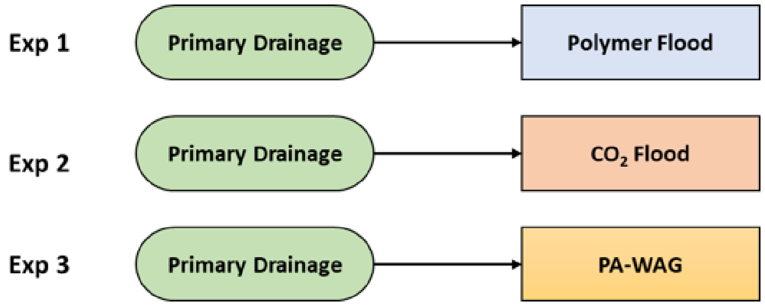

Figure 4.1: Summary of simulation sequence for each experiment. In each experiment, primary drainage was simulated before the recovery process to establish the initial oil (S_{oi}) and the connate water (S_{wr}) saturation.

Each sequence was simulated independently, meaning the simulations for Exp. 1, Exp. 2, and Exp. 3 were carried out separately. This approach allowed for a focused analysis of each experiment and provided insights into the system's behaviour under different conditions.

The history-matching process aimed to numerically reproduce the observed pressure drop along the core, the oil recovery evolution during each flood and the saturation distribution at various injection times (PVI).

By comparing the simulated results with the actual experimental data, the history-matching process facilitated the calibration of the model. It ensured that it accurately represented the observed behaviour of the system. This involved adjusting various model parameters or properties to minimise the mismatch between the simulated and observed data.

The discussion of the results in this chapter involves analysing the accuracy of the history-matched model, identifying areas of improvement or uncertainty, and interpreting the implications of the findings.

4.1. Primary Drainage

The primary drainage stage was simulated and analysed in the history-matching process before simulating the EOR processes in each experiment. This stage involved injecting oil into the modelled core to establish the S_{wr} and S_{oi}. The results of the history-matching process for the primary drainage stage are presented in this section. Since all the core-flood experiments were conducted on Bentheimer sandstone cores, similar results were observed in each case, albeit with slight variations depending on the specific properties of each core. Therefore, the results from a representative primary drainage stage of Exp. 3 are presented to illustrate the findings. Nevertheless, the results from Exp. 1 and Exp. 2 can be found in appendix C. These results primarily focus on the pressure drop and oil saturation profiles.

4.1.1. Pressure Drop Profile

The results indicate that the pressure drop profiles obtained from the simulations match well with the experimental data in terms of the breakthrough times and maximum pressures observed in each experiment. Figure 4.2 shows the obtained match between the simulated and experimental pressure drops for Exp. 3.

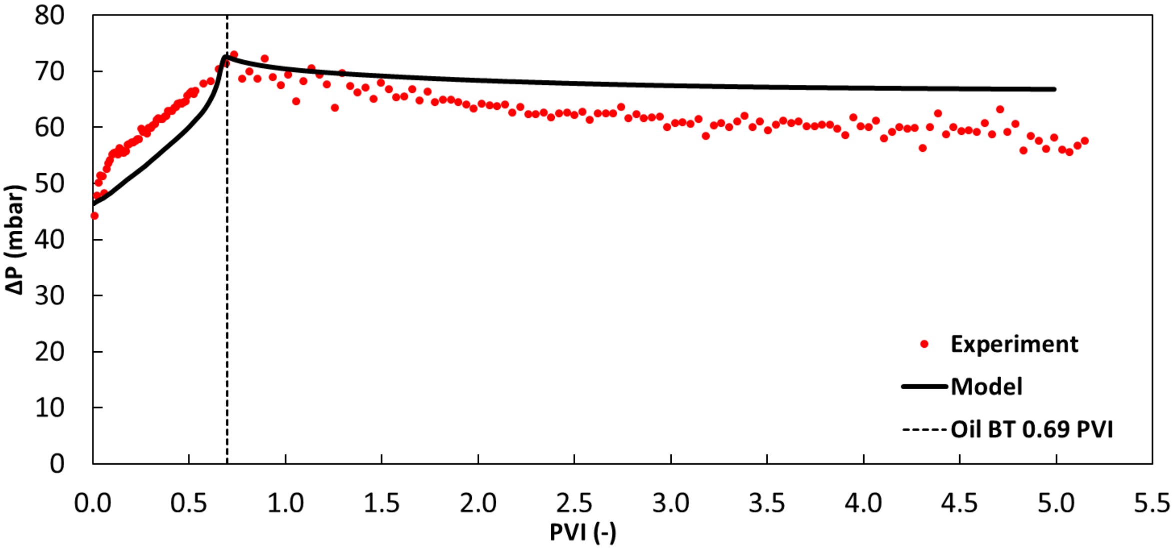

Figure 4.2: Pressure drop match for primary drainage before PA-WAG injection in Bentheimer sandstone, Exp. 3. The breakthrough time for the oil phase was 0.69 ± 0.04 PVI.

One significant observation is the persistent increase in pressure drop when the oil comes into contact with the core. This increase is attributed to the displacement of the less viscous brine by the more viscous oil. It is indicated by a capillary entry pressure of approximately 45 ± 3 mbar for all the Bentheimer sandstone experiments. However, it is important to note that an artificial correction of 45 mbar was added to the simulated pressure drops to achieve a match for the capillary entry pressure. This correction was necessary because the experimental setup involved constant back pressure, which is difficult to replicate accurately in simulations. Despite this correction, the pressure drop trend in the simulations still aligns with the experimental results, indicating that the model effectively captures the flow physics.

As the oil phase front continues to propagate through the core, the pressure drop steadily increases until the breakthrough of oil at the producing side of the core, which occurs at approximately 0.69 ± 0.04 PVI. The maximum pressure drop during this steady increase is around 75 mbar. After the oil breakthrough, the simulated pressure drop shows a steadily decreasing trend, unlike the experimental data, which exhibits fluctuations with a general decreasing trend until an overall stable pressure drop is reached. This difference can be attributed to the oil flow through the core at or near the S_{wr}. In the experiments, some of the remaining displaced phase, i.e., water, is still being mobilised and produced at the outlet, which delays the establishment of the S_{wr} leading to the fluctuation in pressure drop until a stable trend is achieved. In contrast, the simulation setup experiences different dynamics, where the S_{wr} is established quickly after the oil breakthrough. Overall, while the simulated pressure drop profiles accurately capture the breakthrough times and maximum pressures observed in the experiments, there are some differences in the post-breakthrough behaviour. These differences can be attributed to the complexities of replicating the experimental setup. The pressure drop profiles for the primary drainage phase of Exp. 1 and Exp. 2 showed similar results as can be seen from the figures C.2 and C.6 in appendix C

4.1.2. Saturation Profile

Matching the saturation profiles is another crucial aspect of the modelling process, and this is made possible due to the availability of robust CT-Scan data obtained from the experiments. Figure 4.3 shows the match for the oil saturation obtained during the primary drainage phase of Exp. 3, while Figure 4.4 visualises the oil saturation at different stages of the primary drainage process.

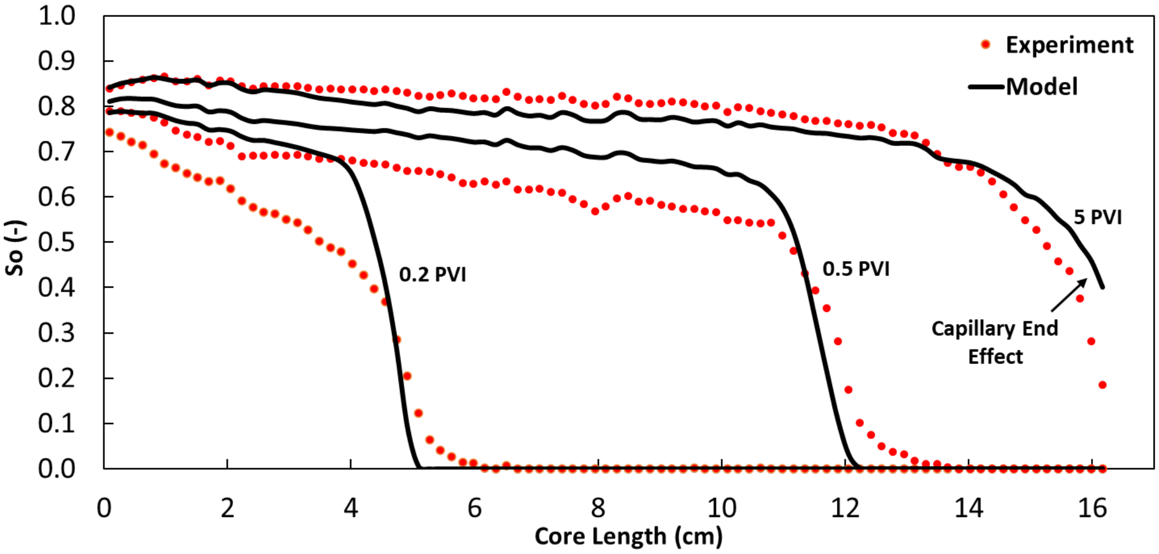

Figure 4.3: Oil saturation match at several PVI during primary drainage in Exp. 3. Buckley-Leverett displacement at 0.2 and 0.5 PVI. The capillary-end effect was observed at the end of primary drainage at 5 PVI.

In all the experiments, a good match between the simulated and observed data for the oil saturation during the primary drainage stage was achieved at different PVI. The primary drainage stage is characterised by the displacement of water by injected oil, and the results indicate the presence of a shock front and an upstream rarefaction wave, which are typical features of a Buckley-Leverett displacement process [9]. In addition to the Buckley-Leverett displacement, the capillary-end effect is another important phenomenon observed during the primary drainage stage. The capillary-end effect refers to the accumulation of brine at the core outlet, which arises from the discontinuity of capillarity in the wetting phase during primary drainage; in this case, brine at the outlet end of the core sample [17]. This effect is responsible for the lower S_o at the outlet end of the core, which can be observed in the last 2 cm of the core section at 5 PVI in Figures 4.3 and 4.4. Both the experimental and simulated data demonstrate the presence of the capillary-end effect in the final saturation profile of the primary drainage stage. The Leverett-J function is a fundamental tool to relate the capillary pressure distribution to the saturation profile, as discussed in section 3.4.2. In this simulation, the Leverett-J function was scaled to the S_w distribution obtained from the CT-scan data at the end of the primary drainage process. This scaling allowed for determining the capillary pressure distribution, which generates the observed capillary-end effect. By incorporating the CT-scan data and leveraging the Leverett-J function, the simulation accurately reproduces the capillary pressure distribution and the resulting capillary-end effect during the primary drainage stage. The correlation between the S_w distribution and the capillary pressure along

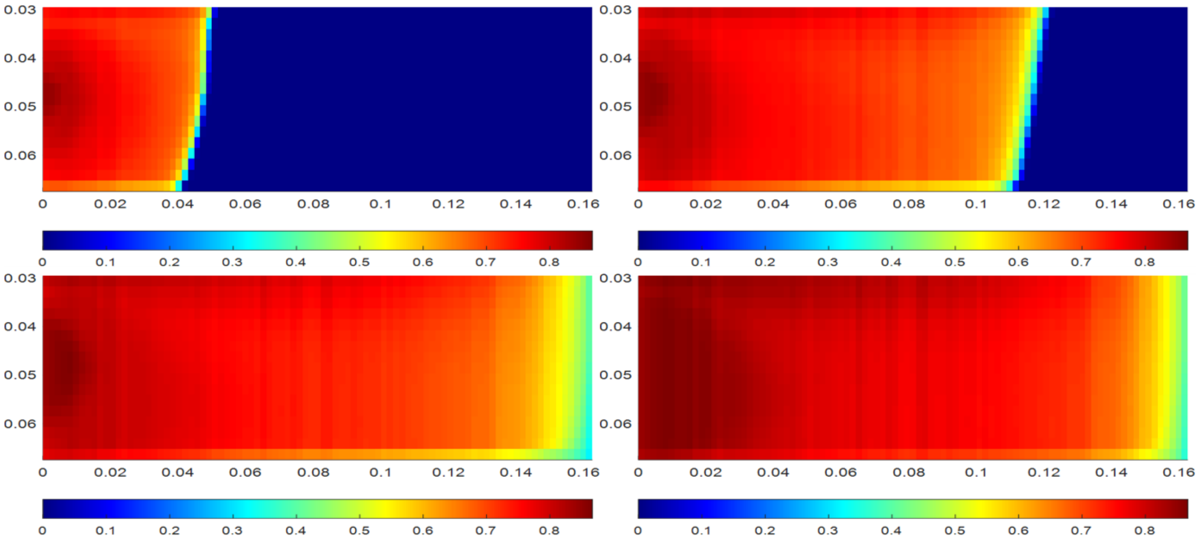

Figure 4.4: Simulation visuals of primary drainage, Exp. 3 in MRST. Clockwise from top left - Oil saturation at 0.2, 0.5, 1 and 5 PVI Oil. The capillary-end effect is visible from the low oil saturation at 5 PVI in the last 2 cm of the core.

the length of the core, as well as the capillary pressure curves derived from each experiment using this approach, are illustrated in Figures G.1, G.2, and G.3 in appendix G. These figures show that the elevated water saturation towards the core's end leads to increased capillary pressure demand for the displacement of water by oil. This phenomenon contributes to the observed capillary end effect at the core outlet. Similarly, good matches for S_o were also obtained for Exp. 1 and Exp. 2, as shown in the Figures C.3 and C.7 of appendix C. This demonstrates the effectiveness of this approach in capturing the complex fluid behaviour and flow dynamics involved in the displacement process.

4.2. Polymer Flooding

In Exp. 1, the process of recovering oil through polymer flooding as a secondary recovery method was simulated. The polymer injection phase commenced after establishing the S_{oi} and S_{wr} during the primary drainage stage. The results of the polymer flood are presented and discussed in this section, focusing on various key outcomes, including pressure drops, oil saturation, and the oil recovery factor.

4.2.1. Pressure Drop Profile

The pressure drops generated during the polymer flood provide insights into the resistance encountered by the flowing fluids and the efficiency of the displacement process, which can help assess the effectiveness of the polymer flooding technique. Figure 4.5 shows the obtained match between the simulated and experimental pressure drops for Exp. 1.

During the polymer flooding of the core, a consistent rise in pressure drop is evident until reaching the breakthrough point. This pressure increase stands out prominently compared to the primary drainage stage, primarily due to the higher viscosity of the polymer in contrast to the oil. This elevated viscosity value is linked to the effective viscosity of the water-polymer mixture, as determined by the Todd-Longstaff mixing model. In this model, viscosity rises with increasing polymer concentration. The effective water viscosity, which encompasses contributions from both water and polymer, is computed through Equation 3.13, taking the mixing parameter and viscosity multiplier at the final polymer concentration as inputs. Furthermore, the polymer molecules present in the injected slug lead to a reduction in water permeability. This reduction is mainly influenced by polymer adsorption and the entrapment of polymer molecules in narrow pore throats. The Langmuir adsorption relation 3.9 and the permeability reduction Equation 3.10 are employed to incorporate this effect into the model. The interplay between these factors, namely effective viscosity and permeability reduction, results in a substantial pressure drop until the breakthrough point is reached, as described by the modified form of the Darcy law for polymer flooding given by Equation 3.8. After the breakthrough, a steady state of polymer flow is established, reflected in the simulated pressure drop by a gradual decline in pressure, eventually stabilising

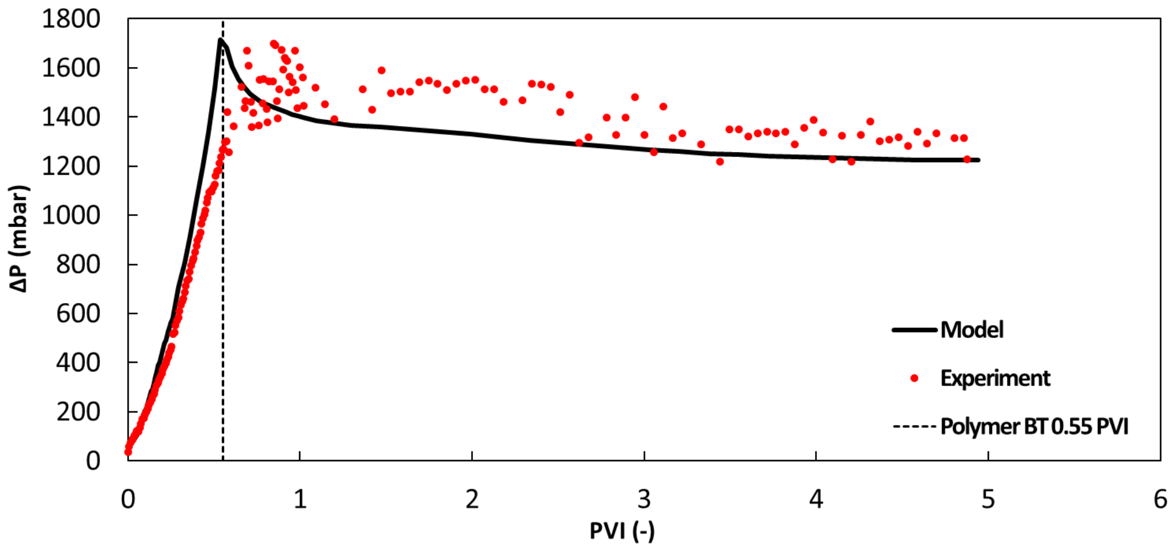

Figure 4.5: Pressure drop match for Polymer Flood, Exp. 1 at an injection rate of 0.5 cm^3/min. A breakthrough occurs earlier at 0.55 ± 0.04 PVI in the simulation compared to the observed data. Pressure drop rises to 1700 ± 20 mbar and stabilises at 1300 ± 50 mbar after breakthrough.

towards the end of the injection process. However, there is a slight mismatch between the decline trends of the model and the experiment at the breakthrough, with the latter exhibiting fluctuations. This can be attributed to the formation of emulsions at the polymer breakthrough. While the emulsions are not explicitly incorporated into the model, the model strives to account for their impact on the pressure drop profile. This is done by using the RRF as a history-matching parameter to account for the additional permeability reduction due to the formation of emulsions. As a result of the history-matching, a high value of 3.4 for RRF was found to be suitable, which caused the pressure to spike up to 1700 ± 20 mbar (according to the Equations 3.10 and 3.8) before gradually decreasing to 1300 ± 50 mbar after the polymer breakthrough. It is important to note that these emulsions can introduce additional pressure fluctuations in the experimental setup, leading to the observed discrepancy between the simulated and observed pressure drop. Despite this difference, there is a good match between the observed and simulated pressure drop profiles. However, the breakthrough of the polymer occurs slightly earlier at 0.55 ± 0.04 PVI in the simulations, resulting in a mismatch of approximately 0.04 ± 0.01 PVI. This mismatch could be attributed to the differences in adsorption trends between the experiments and the model. The polymer model employed in MRST adheres to a Langmuir adsorption isotherm, as discussed in 3.3.1. This isotherm necessitates adsorption data at different polymer concentrations. Since only one polymer adsorption value at 2000 ppm was accessible from the experimental data, adsorption values at various concentrations from literature about a similar HPAM polymer [68] were employed to construct a Langmuir isotherm for the simulations. It is crucial to note that employing this approach may result in estimated adsorption parameters yielding a lower adsorption rate in the simulations compared to the actual experimental conditions. Consequently, this discrepancy could prompt an earlier polymer breakthrough in the simulations. Furthermore, the mismatch in breakthrough could also arise from the assumption of a constant value for the IPV in the model. At the same time, there might be actual variability in this parameter. This variability could contribute to the observed difference in breakthrough timings.

4.2.2. Saturation Profile

The simulated saturation profiles align with the observed profiles in the experiments, as seen in Figure 4.6. This is particularly evident in the saturation profiles accurately depicting the polymer front propagation at different injection times. As the saturation distribution from the primary drainage stage is used as input for the polymer flood stage, the saturation profiles ahead of the polymer front also show excellent correspondence. The model captures the characteristics of a sharp, stable piston-like front during the polymer flood, leading to a favourable displacement caused by the reduction in the end-point mobility ratio from 0.9 to 0.05. The impact of lowered mobility ratio can be seen on the fractional flow curve (Figure 4.8) as it resembles a piston-like displacement front in accordance with the Equation 2.4 after adding polymer. The propagation of the polymer front at different injection stages from the start until the establishment of S_{orw} can be visualised with the simulation results as seen in Figure 4.7.

The capillary end effect, observed in the saturation profiles near the outlet, is prominent until approximately 0.7 PVI, following the breakthrough of the polymer at 0.55 ± 0.04 PVI. This effect reflects the influence of capillary forces and is accurately represented in the model's saturation profiles. After injecting 5 PVI, the simulation reaches the residual oil saturation, indicating that the maximum oil recovery has been achieved.

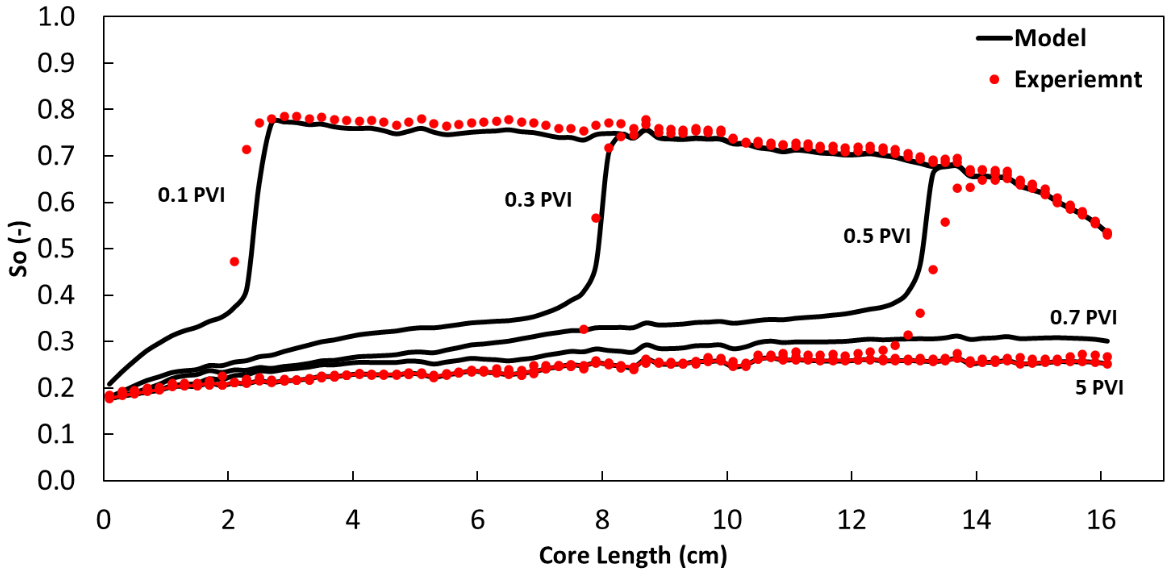

Figure 4.6: Oil saturation profile during polymer flood, Exp. 1 showing the match for the position of the polymer front at several PVI.

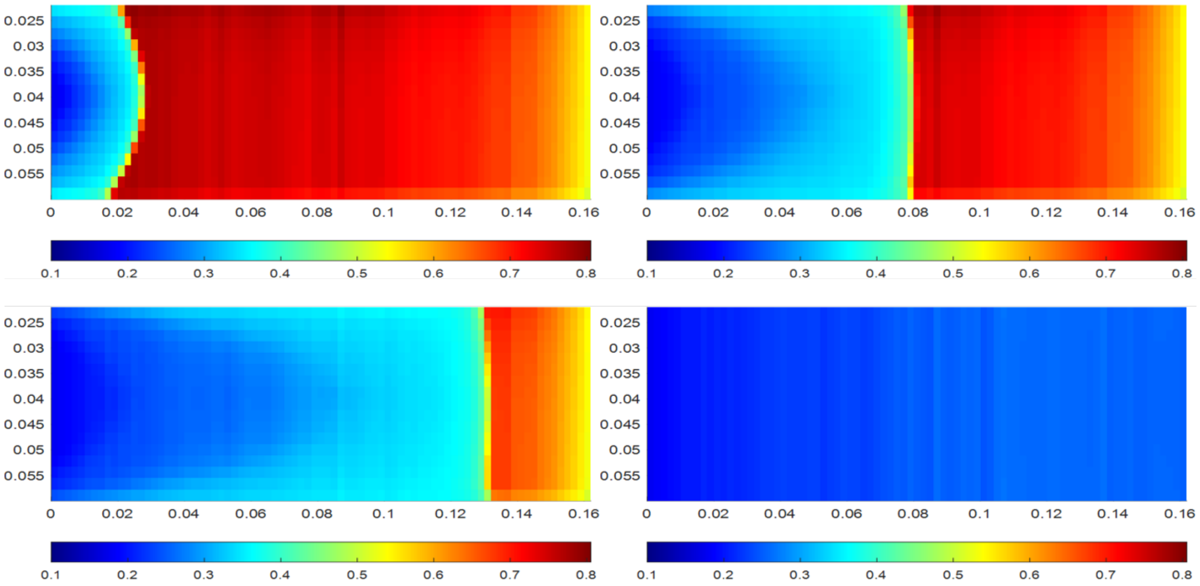

Figure 4.7: Simulation visuals from MRST of propagation of the polymer front (clockwise from top left) at 0.2, 0.3, 0.5 and 5 PVI, respectively.

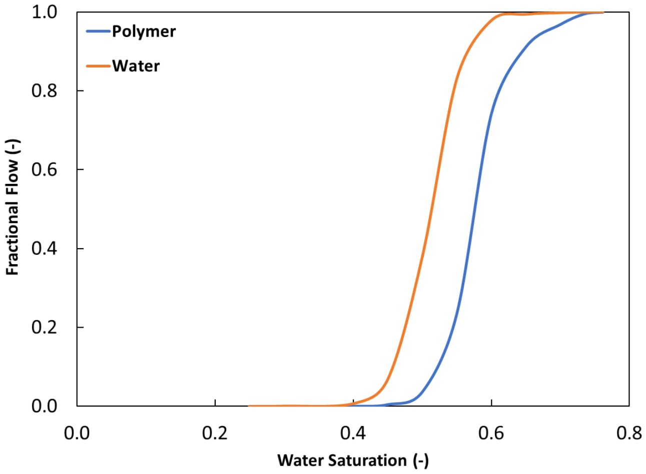

Figure 4.8: Increase in the fractional flow of water to resemble a piston-like displacement front due to the reduction in end-point mobility ratio upon adding polymer. The fractional flow during waterflood is derived from the work of Janssen et al. (2020) [19]

4.2.3. Oil Recovery Factor

The modelling of the oil recovery factor was achieved by history-matching the simulated curves with the experimental recovery factor data points obtained through CT scans. The match for the recovery factors for the polymer flood process can be seen in Figure 4.9. The simulated recovery factor aligns well with the observed data. Typically, in polymer flooding, most oil recovery occurs before the breakthrough, with minimal recovery afterwards. However, the simulated curves indicate continued recovery after the breakthrough at 0.55 ± 0.04 PVI. This slight difference can be attributed to the modifications made to the relative permeabilities used in the model as discussed in 4.2.1.

A mismatch is observed at the breakthrough, wherein the simulated recovery factor falls short of the value observed in the experimental data. This can be attributed to the difference between the simulated and experimental profiles for S_o at 0.7 and 5 PVI. Specifically, the model reflects a higher amount of remaining oil than the experiment, as illustrated in Figure 4.6 resulting in lower simulated recovery.

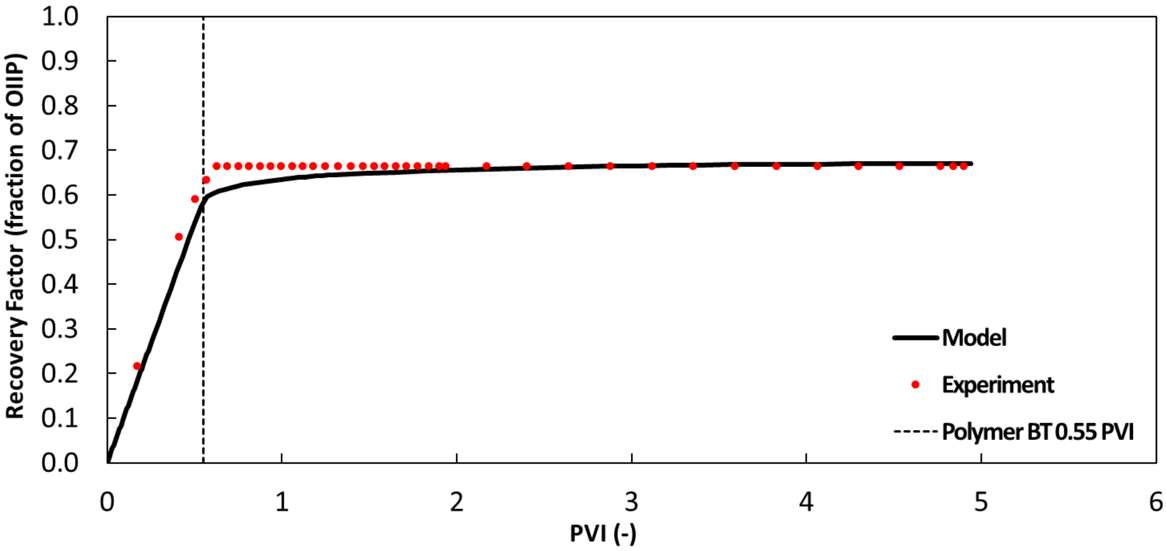

Figure 4.9: Simulated Oil Recovery Factor match with CT-based experimental recovery factor for polymer flood, Exp. 1.

4.3. CO_2 Flooding

Exp. 2 focuses on oil recovery through CO_2 flooding as a secondary oil recovery method. Like Exp. 1, the CO_2 injection phase in Exp. 2 began after establishing the S_{oi} during the primary drainage stage. The results of the CO_2 flooding simulation are presented and discussed in this section, encompassing key parameters such as pressure drops, oil, water and gas saturation, and the oil recovery factor.

4.3.1. Pressure Drop Profile

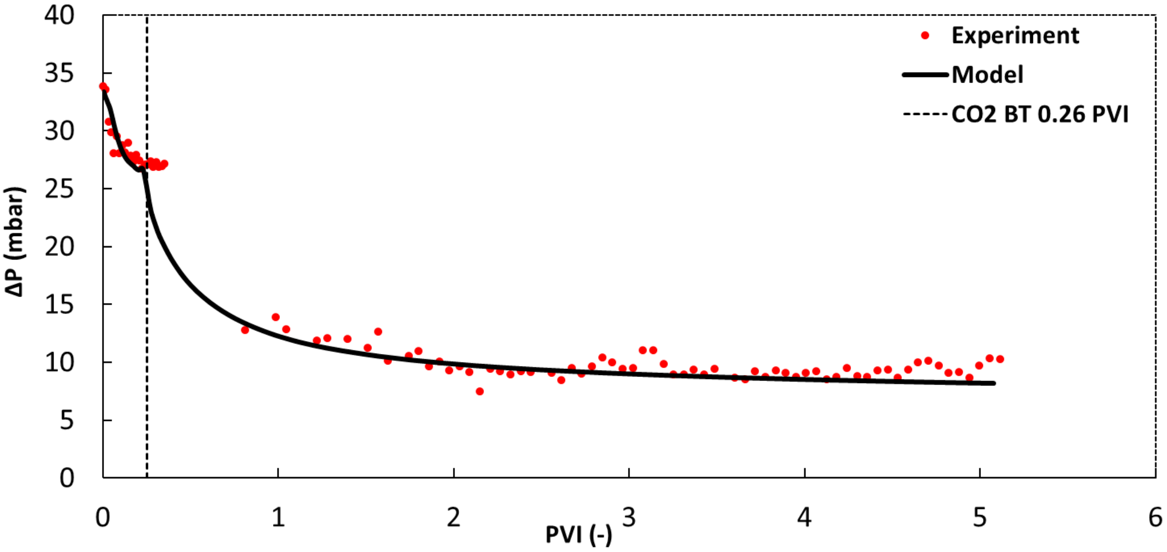

Figure 4.10: Pressure drop match for CO_2 Flood, Exp. 2. The breakthrough occurs at 0.26 ± 0.05 PVI, where the pressure drops from 32 ± 3 mbar to 26 ± 3 mbar and stabilises at 10 ± 3 bar after the breakthrough.

The pressure drop profile observed during the CO_2 flooding experiment (Figure 4.10) as a secondary oil recovery method exhibits a decreasing trend from the beginning of injection. This decrease is primarily due to the rapid breakthrough of CO_2. The pressure declines from the initial capillary entry pressure of 32 ± 3 mbar to 26 ± 3 mbar at breakthrough. Several factors contribute to this rapid breakthrough. Gravity segregation constitutes the initial factor, stemming from the substantial density contrast between CO_2 and oil, which positions CO_2 atop the oil within the core. This placement along the core is particularly pronounced due to the horizontal orientation of the core. This horizontal orientation allows for a more extensive manifestation of the gravity segregation effect than the vertical orientation. The second factor arises from the lower viscosity of CO_2 relative to oil, resulting in an unfavourable mobility ratio. Consequently, CO_2 tends to channel through the highly permeable layers. The last factor involves immiscible injection conditions, where the CO_2 and oil remain distinct in phases rather than forming a unified phase. The lack of miscibility prevents the formation of a single phase, accelerating the breakthrough process of CO_2. Overall, the simulation results exhibit a good match with the observed data.

Shortly after the breakthrough, the pressure drop sharply declines and exhibits distinctive fluctuations due to the co-production of different fluid phases. These fluctuations arise from the simultaneous production and interaction of oil, water, and gas within the core. The general decreasing trend in pressure drop after the breakthrough eventually flattens out, reaching a steady-state pressure of 10 ± 3 mbar.

4.3.2. Saturation Profile

Figure 4.11 depicts S_g and S_o profiles at various times (PVI) during CO_2 flooding. These profiles exhibit a favourable correspondence with experimental data. Figure 4.12 presents changes in S_o due to CO_2 injection at different time intervals. The model captures the gravity segregation phenomenon driven by the contrasting densities of oil and CO_2. Specifically, CO_2 selectively displaces the upper section of the core right from the initial injection phase, leading to a swift CO_2 breakthrough. After the breakthrough, the CO_2 progressively sweeps through a more significant portion of the core's lower segment. However, a section of the core remains unswept by CO_2 at the conclusion of the injection process. Using a black oil-type model to simulate this process overlooks the potential compositional changes arising from CO_2 dissolution in oil. Nonetheless, using CT scan saturation data to calibrate relative permeability curves compensates for this limitation and yields a commendable agreement with observed data.

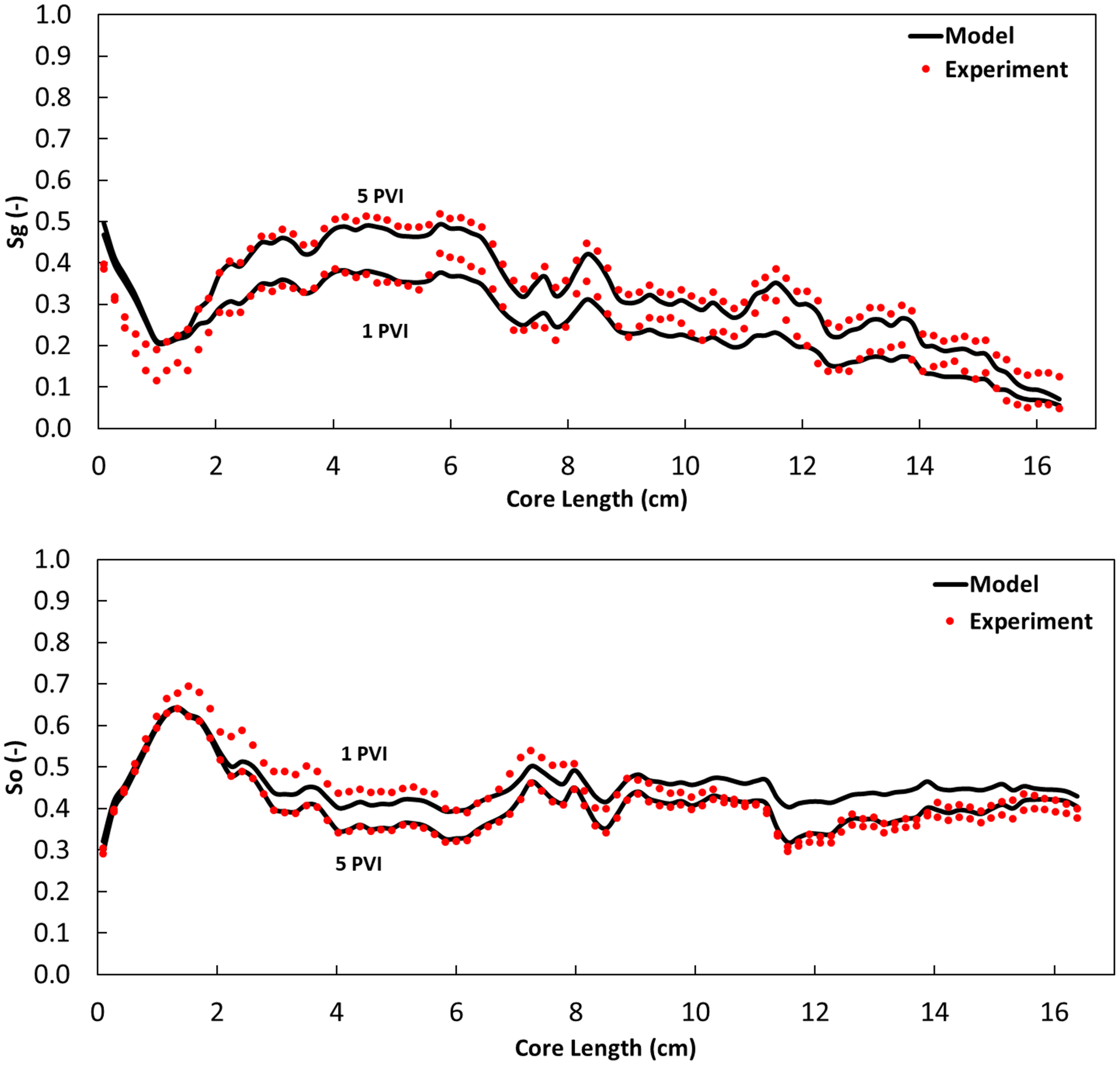

Figure 4.11: Gas (top) and Oil (bottom) saturation match at several PVI during CO_2 flood, Exp. 2.

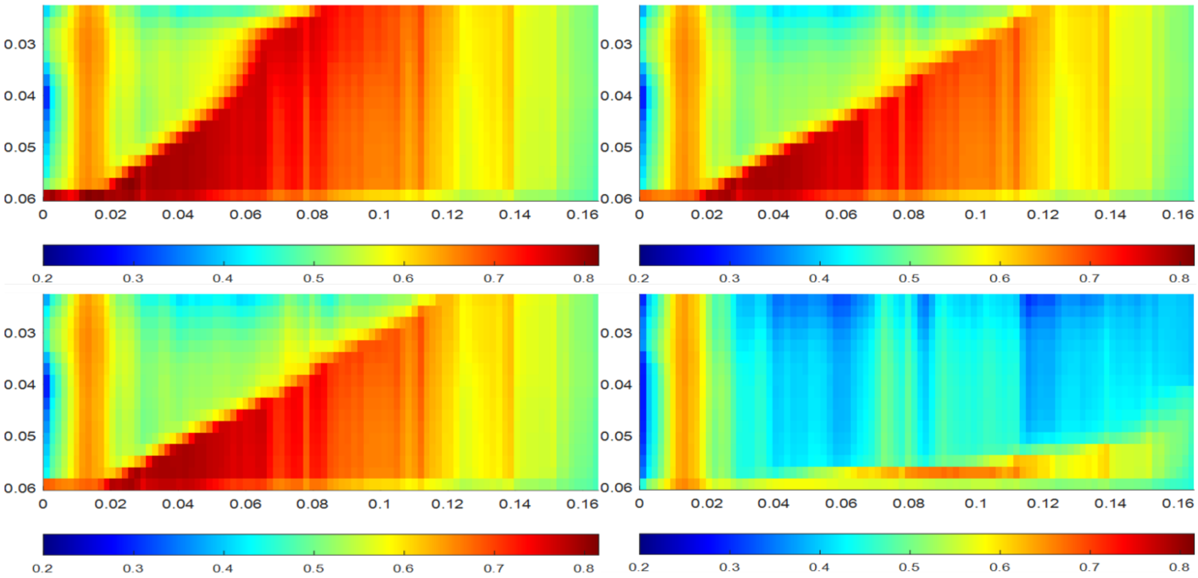

Figure 4.12: Changes in oil saturation and the effect of gravity segregation with the injection of CO_2 (clockwise from top left) at 0.1, 0.15, 0.25 and 1 CO_2 PVI, respectively, visualised in the MRST simulation runs. CO_2 initially sweeps the upper section of the core. After the breakthrough at 0.26 ± 0.05 PVI, starts sweeping the lower section.

4.3.3. Oil Recovery Factor

The oil recovery factor for the CO_2 flood process is illustrated in figure 4.13. The simulated recovery factor closely aligns with the observed data. Before the CO_2 breakthrough, approximately 22% of the OIIP is recovered. In contrast, the remaining oil is recovered up to 5 PVI of CO_2, resulting in a total recovery factor of 40%. This recovery trend corresponds with the changes in saturation observed in figure 4.12, where a substantial portion of the oil is recovered from the upper part of the core before the CO_2 breakthrough. After the breakthrough, the remaining recovery occurs as CO_2 sweeps through the lower section of the core, displacing the oil and facilitating further recovery.

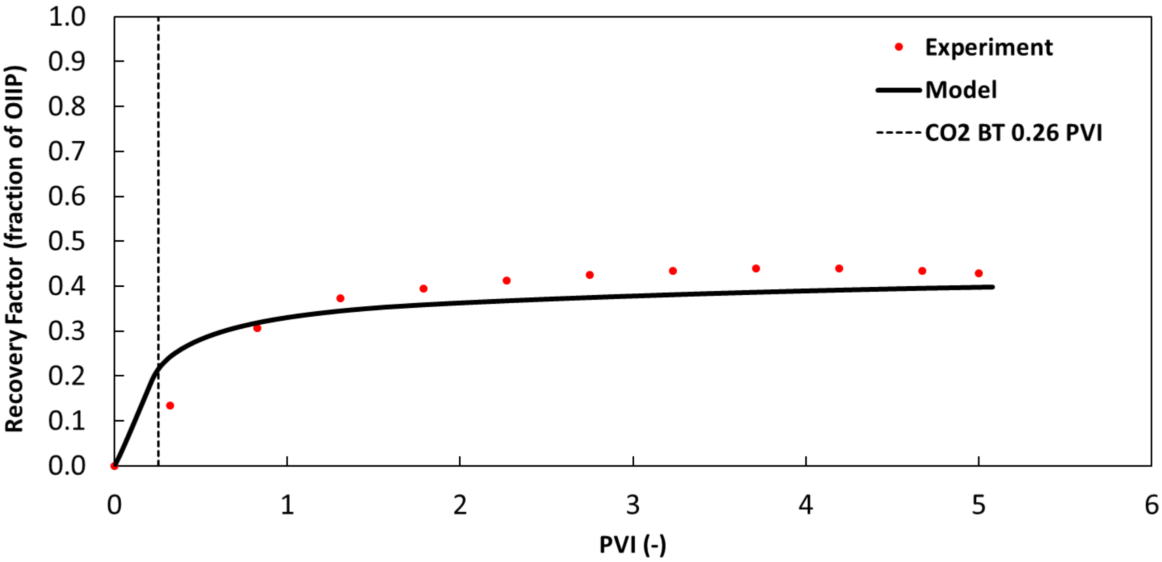

Figure 4.13: Simulated Oil Recovery Factor match with CT-based experimental recovery for the CO_2 flooding, Exp. 2. A continued recovery is observed after the breakthrough at 0.26 ± 0.05 PVI as the CO_2 sweeps the lower section of the core.

4.4. PA-WAG Injection

This experiment combined the polymer and CO_2 flood simulators to model the PA-WAG injection scheme and investigate its impact on oil recovery mechanisms. The experiment involved a total of 6 PA-WAG cycles. Each cycle comprised two stages: injecting polymer at 2 cm^3/min for 0.22 PVI followed by the injection of CO_2 at 0.5 cm^3/min for 1.2 PVI. The analysis and discussion of the results are based on the pressure drops, saturation profiles, and recovery factors obtained during the process

4.4.1. Pressure Drop Profile

Figure 4.14 illustrates the match obtained for the pressure drop profiles for the PA-WAG injection.

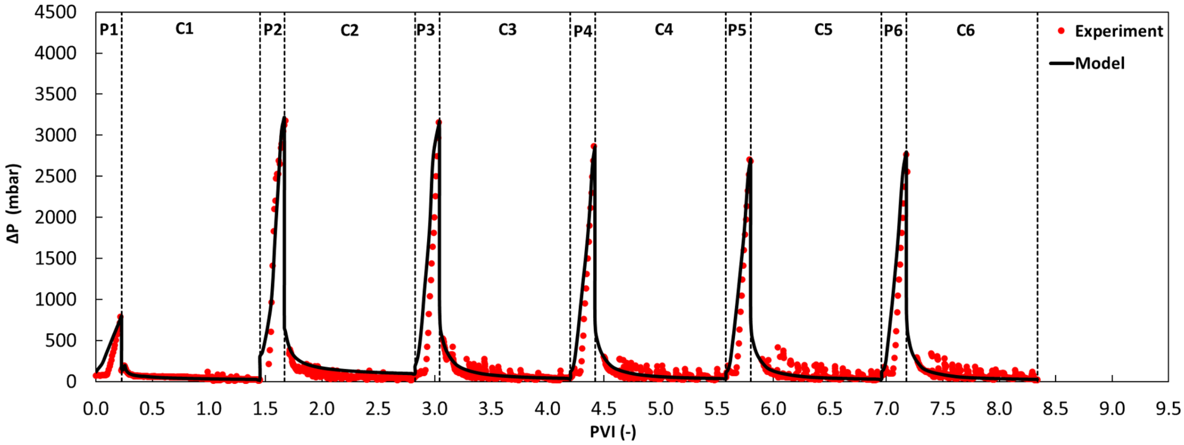

Figure 4.14: Pressure drop match for the PA-WAG injection with alternating slug size and injection rate for polymer (0.22 PVI at 2 cm^3/min) and CO_2 (1.2 PVI at 0.5 cm^3/min). Pn and Cn (n = 1 - 6) indicate each cycle's polymer and CO_2 injection phases, respectively.

The pressure drop profile observed during the polymer slug injection in the first cycle of the PA-WAG experiment closely resembles the pressure drop profile from the polymer flood, Exp. 1, as illustrated in Figure 4.5. Upon evaluating the pressure drop at the same PVI, it was found that the pressure drop at the end of the polymer slug for PA-WAG reaches 790±5 mbar, nearly two times higher than Exp. 1. The higher pressure drop in PA-WAG can be attributed to the injection rate, which is four times higher than that of Exp. 1. This increased injection rate reduces the polymer viscosity by approximately 0.5 times due to shear thinning behaviour at higher flow rates resulting in higher pressure drop values than Exp. 1. Furthermore, an increased RRF value, which is 1.5 times greater than Exp. 1, results in an additional decrease in permeability. This contributes significantly to the observed pressure drop. This observed pressure behaviour aligns with Darcy's law (Equation 3.8). During the transition to CO_2 slug injection, the pressure experiences a sharp decline from 790 ± 5 mbar to 85 ± 5 mbar. This drop is attributed to the notably lower viscosity of CO_2 compared to that of the polymer and oil. Additionally, the rapid breakthrough is facilitated by gravity segregation and the channelling of CO_2 along the path of least resistance.

In the second cycle of the PA-WAG process, there is a significant increase in pressure drop as polymer injection commences. This notable rise in pressure can be attributed to several factors. Firstly, the increase in injection rate when transitioning from CO_2 to polymer injection leads to higher flow rates, resulting in elevated pressure responses. Moreover, during this phase, gas trapping occurs due to the reduction in gas relative permeability caused by increased water saturation above the connate water saturation, resulting from the aqueous phase's injection. The phenomenon of gas trapping in the presence of higher water saturation has been previously reported by Skauge & Larsen (1994) [52] in their gas displacement experiments carried out under varying wettability conditions. Consequently, a simulation approach was implemented that involved segmenting the run. The half-cycles of polymer and CO_2 were individually simulated during the initial two injection cycles. This was achieved by utilising independent relative permeability curves for each half-cycle. The primary goal was to precisely model the effect of gas trapping in reducing the relative permeability of gas. Figure 3.13 depicts the contrast between the relative permeability curves of cycle 1 and cycle 2, illustrating the decline in gas relative permeability from cycle 1 to cycle 2 as a result of the influence of gas trapping leading to an elevated pressure response during polymer injection. This approach to incorporate the effect of gas trapping was also successfully implemented in the simulation of the WAG process by Janssen et al. (2020) [19].

During the injection of the second CO_2 slug, the overall trend of the pressure drop showed a slight increase, primarily attributed to trapped gas and enlarged S_w. This steady-state pressure drop was sustained in the subsequent cycles. The trapped gas and increased S_w continued to impact the pressure response throughout the subsequent cycles, contributing to the observed steady trend. In contrast, a distinct behaviour was observed during the injection of the polymer slug in the following cycles. After the breakthrough of the polymer at approximately 1.65 ± 0.05 PVI, the maximum pressure drop during polymer injection started to decrease. From cycle four onwards, the peak of pressure drop stabilised, indicating that the injection process reached a relatively steady state during the polymer slug injection in the later cycles of the PA-WAG process.

On the whole, the strategy of segmenting the simulation run to replicate the injection cycles effectively captured the impact of gas trapping and resulted in a remarkable alignment between the simulated and observed pressure drops.

4.4.2. Saturation Profile

This section presents the saturation profiles for oil, gas, and water observed during the various injection stages throughout the PA-WAG process. Alongside the observed data, simulation visuals generated by MRST are included. The simulation visuals depict the positions of the polymer front and the gravity segregation of CO_2 due to density contrast. This demonstrates the model's effectiveness in capturing these essential features of the PA-WAG process.

In Figure 4.15, at the end of polymer injection (0.22 PVI) during the first cycle, S_o profile exhibits a piston-like displacement behaviour of polymer, where the injected polymer effectively displaces oil in the first half of the core. As the injection shifts to CO_2, the influence of gravity becomes apparent, and the CO_2 starts displacing the oil from the upper section in the second half of the core, resulting in a significant reduction in oil saturation in that region. However, at this point, the CO_2 has not yet begun displacing the polymer, as indicated by the minimal change in the polymer front (reflected in the S_w profile in Figure 4.15) at the end of CO_2 injection during the first cycle.

Moving to the second cycle, gas trapping becomes evident. The S_g profile (Figure 4.16) at the end of polymer injection (0.22 PVI) in cycle 2 shows the occurrence of trapped gas, of which a certain amount remains immobile and cannot be displaced by the polymer injection. This trapped gas affects the characteristic piston-like displacement behaviour of the polymer, as it is less pronounced in the S_w profile (Figure 4.16). Despite the presence of trapped gas and the alteration in the polymer's displacement pattern, there is continued oil recovery. This recovery can be observed from the difference in S_o at the end of cycle 1 and the end of polymer injection in cycle 2. Upon injecting CO_2 in the second cycle, S_o is further reduced, approaching very close to the residual values, indicating significant oil displacement and recovery during this stage.

In subsequent cycles from 3 to 6, the saturation profiles for oil, water, and gas demonstrate a similar pattern. To illustrate this, only the results for cycle 6 are presented in this section. As shown in Figure 4.17, S_o for both polymer and CO_2 injection phases overlaps, indicating that S_o does not change significantly compared to S_o at the end of cycle 2 (Figure 4.16). This observation points to negligible incremental oil recovery in these cycles. Furthermore, a constant trapped gas saturation is also established at the end of polymer injection in cycle 3, as evident from the retention of the gas saturation trend until the end of the complete PA-WAG injection process. The saturation profiles for the PA-WAG cycles 3 and 5 can be visualised from the figures F.8 and F.10 in appendix F. The saturation profiles in these cycles are consistent with the trend observed in cycle 6, indicating negligible incremental oil recovery after cycle 2.

While the simulation results show a good overall match with the observed data, some minor mismatches are observed in S_w and S_g in cycles 3 to 6. Specifically, the simulated S_g is lower, and the simulated S_w is higher than the observed data. These discrepancies can be attributed to using a simple black oil model in the simulation. The black oil model does not account for compositional changes or viscosity reduction caused by oil swelling due to gas dissolution in the oleic and aqueous phases, which might occur in the actual experiments. However, despite these minor mismatches, the model's incorporation of saturation data from CT scans enables it to match the observed data well.

4.4.3. Oil Recovery Factor

Figure 4.18 displays the match for the oil recovery factor throughout the PA-WAG injection process. The majority of incremental recovery occurs until the polymer breakthrough in cycle two, which takes place around 1.65 ± 0.05 PVI. Following the polymer breakthrough, minimal to no additional recovery is observed in the subsequent cycles. This trend in the oil recovery factor is consistent with the saturation profiles, indicating that most of the oil was recovered towards the end of cycle 2, with negligible incremental recovery in the subsequent cycles. To ensure an accurate comparison between the simulated and observed recoveries, it was crucial to account for the no-flow conditions during the experiments, which caused a delay of approximately 0.2 ± 0.03 PVI in oil production. Appropriate corrections were applied to the experimental recovery data to visualise the simulated and observed recoveries at the exact injection times. After incorporating these necessary modifications, the simulated recovery factors aligned well with the observed data, confirming the model's accuracy in capturing the PA-WAG injection process's oil recovery behaviour.

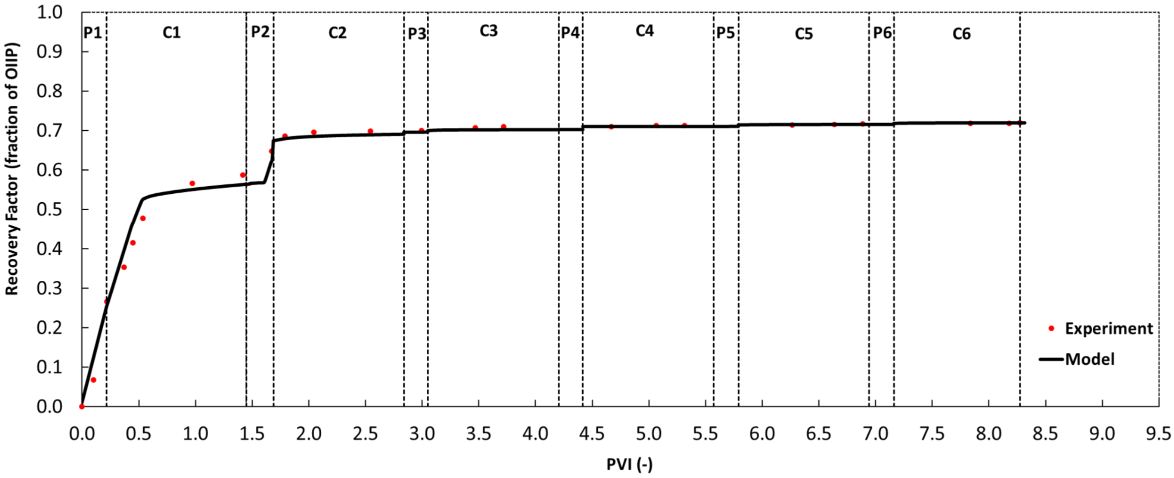

Figure 4.18: Oil Recovery Factor match for PA-WAG injection, Exp. 3. Pn and Cn (n = 1 - 6) indicate each cycle's polymer and CO_2 injection phases, respectively. The majority of incremental recovery occurs until the polymer breakthrough in cycle 2 at around 1.65 ± 0.05 PVI. Following the polymer breakthrough, minimal to no additional recovery is observed in the subsequent cycles.

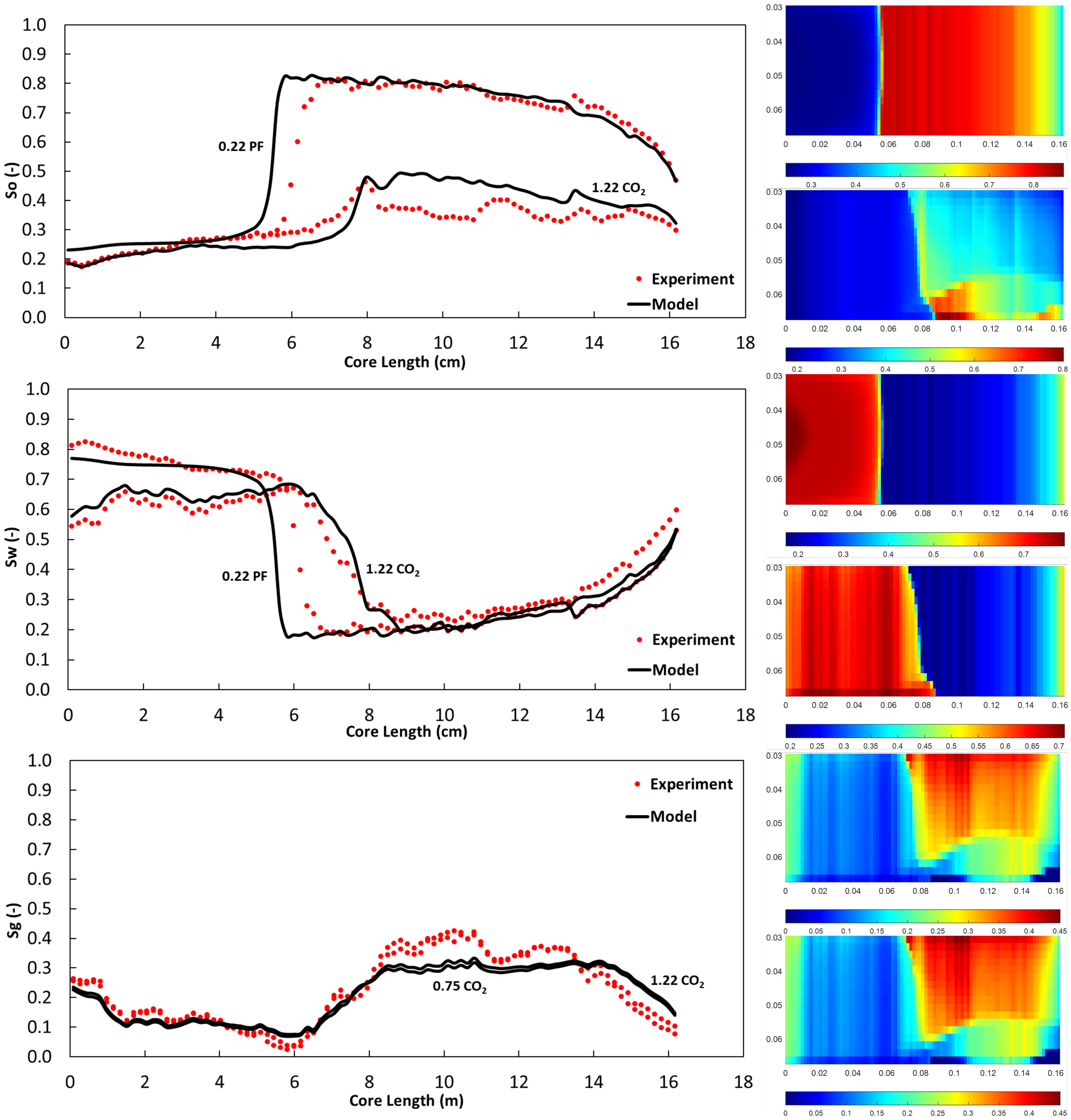

Figure 4.15: Saturation profiles for oil (top), gas (middle) and water (bottom) at the end of cycle 1 after the completion of the polymer slug injection (0.22 PF) and CO_2 slug injection (1.22 CO_2) along with the corresponding MRST simulation. For Cycle 1, gas saturations are only presented for the CO_2 injection phase since there is no gas initially in the system at the start of the PA-WAG injection. Gas saturation becomes relevant only during the CO_2 injection stage.

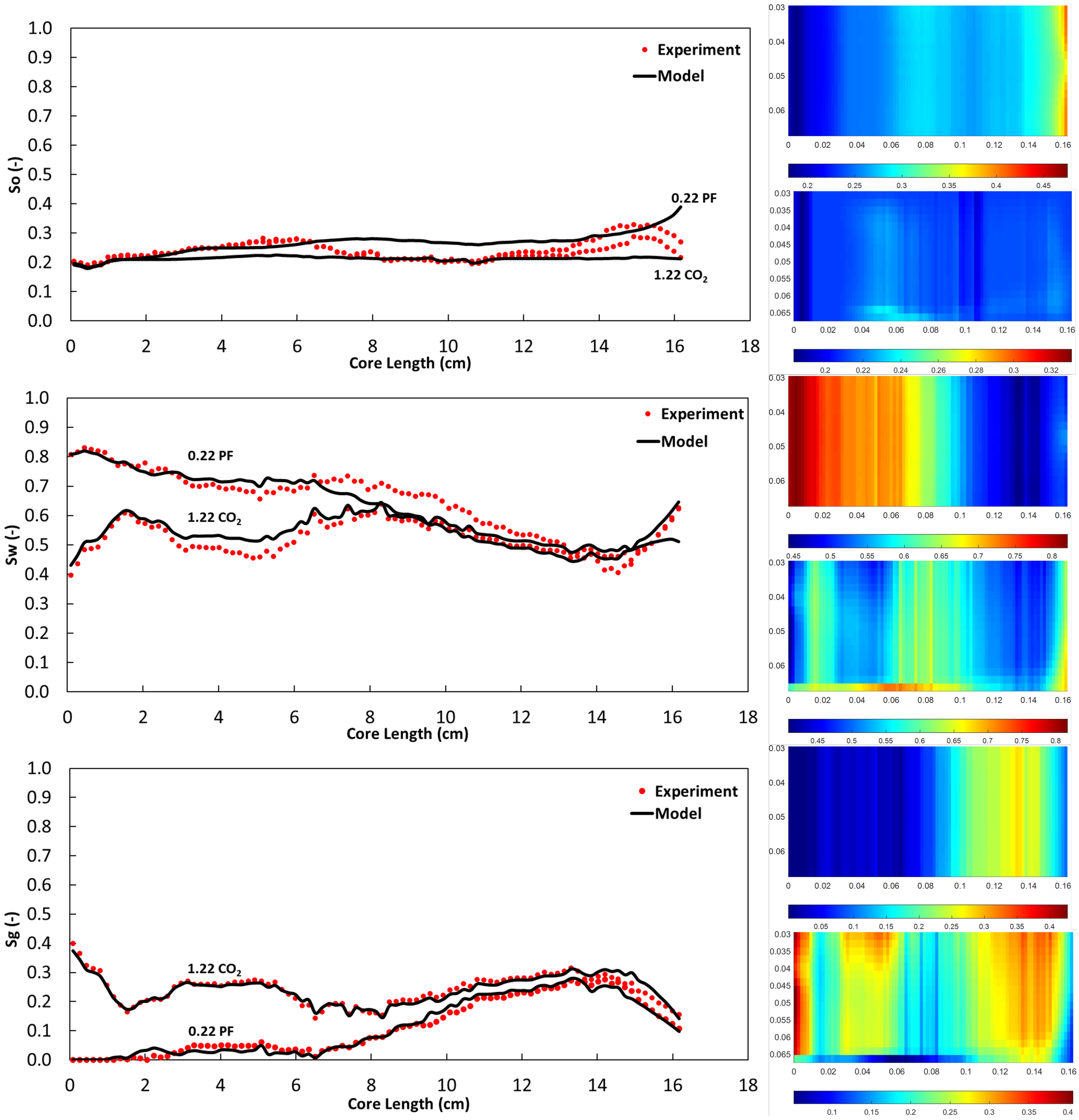

Figure 4.16: Saturation profiles for oil (top), gas (middle), and water (bottom) after the polymer slug injection (0.22 PF) and CO_2 slug injection (1.22 CO_2) in cycle 2 with the corresponding MRST simulation visuals during this stage. Gas trapping becomes evident at the end of polymer injection in this cycle.

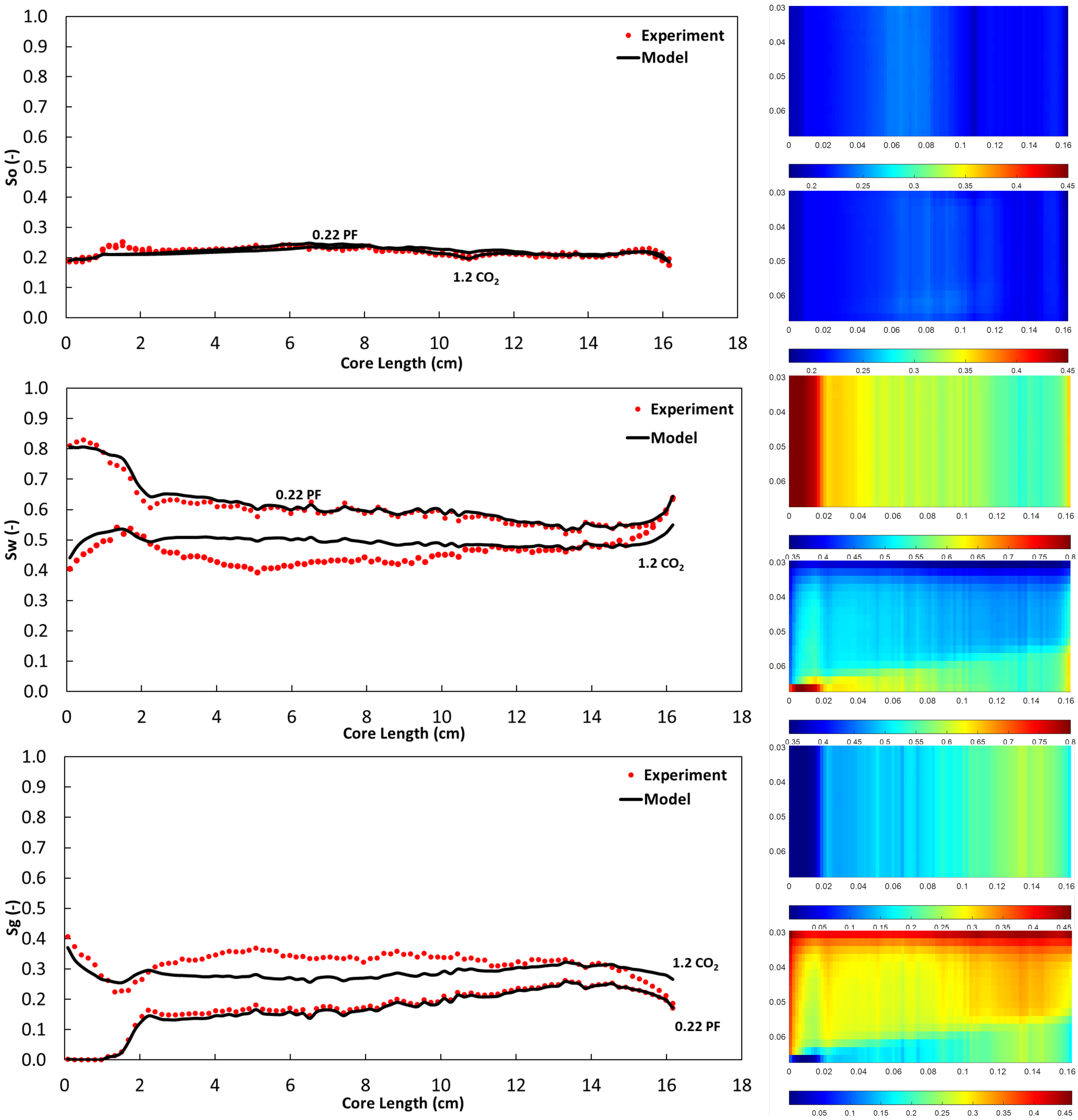

Figure 4.17: Saturation profiles for oil (top), gas (middle), and water (bottom) after the polymer slug injection (0.22 PF) and CO_2 slug injection (1.22 CO_2) in cycle 6 with the corresponding MRST simulation visuals during this stage. For cycle 6, the oil saturations resulting from both polymer and CO_2 injection are identical and overlap each other due to negligible incremental recovery after the end of cycle 2.

5

Conclusions and Recommendations

The successful execution of a modelling study examined three out of the five experiments conducted by van Wieren et al. (2022). These experiments included polymer injection, CO_2 flooding, and PA-WAG injection. CT scan data was highly valuable in discerning the primary mechanisms underlying the intricate recovery processes investigated in this research. This chapter presents the conclusions drawn from this research and recommendations for future work.

A modelling study was conducted using the black oil model to history-match core-flood experiments and examine the physical mechanisms governing the oil recovery process in the PA-WAG injection. The core-flood experiments of van Wieren et al. (2022) were modelled step-by-step. Initially, the primary drainage process was simulated using the generic black oil model in MRST. Subsequently, separate simulations were performed for the polymer injection process using the generic surfactant polymer model and the CO_2 flooding process using the generic black oil model in different runs. The understanding of the physical mechanisms from these individual processes was then used to create the PA-WAG injection model by combining the polymer and CO_2 models. The simulation results, including pressure drops, saturation profiles, and oil recovery factors, were compared and matched with the experimental data. The following conclusions can be drawn based on this research:

5.1. Conclusions

- The grid configuration employed in this study, encompassing the chosen cell quantities and dimensions, effectively showcased its capability to deliver a sturdy depiction of porosity and permeability distributions within the modelled Bentheimer sandstone core sample. The presence of saturation data based on CT scans and relative permeability measurements obtained from pressure drops measured across core sections was pivotal in precisely estimating parameters for the relative permeability curve at various experimental phases. These parameters were pivotal in aligning with observed pressure drops, oil recovery trends, and the progression of saturation distribution.

- The successful replication of the primary drainage process is of utmost importance as it serves as a critical foundation for understanding and establishing the initial conditions required for polymer and gas injection. In this study, the matches achieved for these stages of the experimental sequence were considered satisfactory. The capillary end effect, which significantly impacts fluid flow behaviour, was accurately represented by scaling relative permeabilities to the saturation distribution within the core.

- The success of the polymer flooding history-match is attributed to the use of high-quality CT-scan saturations and experimental data. These data were instrumental in determining polymer-specific input parameters, such as viscosity multipliers, IPV, and polymer adsorption. Despite facing challenges related to emulsion formation and its impact on relative permeability measurements, an effective solution was identified by modifying waterflooding relative permeability using polymer-specific inputs and introducing the RRF as a history-matching parameter. The simulation results revealed that emulsion formation caused a significant increase in pressure drop. Consequently, a high RRF value of 3.4 was adopted to accurately model the effect of permeability reduction on the pressure response. Furthermore, the excellent alignment of the saturation profiles indicated the robustness of the polymer-specific parameters derived from experimental data, enabling an accurate representation of the polymer front's propagation. The robust modelling of pressure drops and saturation profiles also yielded a satisfactory match for oil recovery.

- The history-match of the CO_2 flood as a secondary recovery technique demonstrated that it could be effectively modelled as an immiscible injection process in MRST using the black oil model. Despite the core-flood experiment results indicating CO_2 dissolution in oil and water, the model produced good matches using relative permeability curves scaled to the CT-scan saturations without compositional simulation. Furthermore, implementing a 2D grid in the model allowed for capturing the effect of gravity segregation, which played a crucial role in controlling the oil displacement during the CO_2 flood recovery process. The study also concluded that under immiscible conditions, the end-point relative permeability of CO_2 was relatively low, with a value of approximately 0.01 ± 0.002. This finding is consistent with what others have reported in previous research.

- The history-matching process of the PA-WAG experiments proved to be the most challenging aspect of this study. The simulation runs had to be segmented into separate cycles with independent relative permeabilities to accurately visualise the reduced gas relative permeability resulting from gas trapping and hysteresis effects. Nevertheless, the result was a successful history-match using the PA-WAG injection simulator, which was developed by combining the Polymer and CO_2 flood simulators.

The results obtained from this study were in line with the hypotheses outlined in section 1.2. They demonstrated that an approach utilising the black oil model to create a PA-WAG injection simulator, which integrates the functionalities of both polymer and CO_2 flooding simulators, effectively captured the intricate physical mechanisms involved in the PA-WAG injection process. The model successfully conducted a thorough simulation of the PA-WAG process, accurately reproducing and history-matching the core-flood experiments. This validation of the workflow and methodology underscores the potential of a simplified black oil model as a robust tool for comprehending the complexities of the PA-WAG process. The consistency between the results and initial hypotheses strongly affirms the model's reliability, validating the chosen research approach for investigating the PA-WAG process.

5.2. Recommendations

This thesis answers questions posed at the start of this research and developments along the process, contributing to a better understanding of the physical mechanisms of the PA-WAG recovery method using the black oil model. However, the study encountered some limitations, and several aspects still need further attention. Based on the insights provided by this research, the following recommendations are made for future research to consider:

- It is noteworthy that the study acknowledges the confinement of the simulations to a 2D setup. To heighten precision and capture the inherent variations in porosity, permeability, and phase distributions within the porous medium, the study advocates for integrating a 3-Dimensional (3D) stage with finer grid dimensions. Such a 3D approach would furnish a more extensive portrayal of the core's heterogeneities, thus facilitating a more robust analysis of the recovery processes under investigation.

- It is recommended to design injection schemes for simulations that closely mirror the experimental procedures. By doing so, the need for artificially imposed pressures to align simulation results with experimental data can be minimised or even eliminated.

- For the polymer injection process, it is advisable to collect adsorption data at various concentrations and implement spatially varying IPV. Doing so would enhance breakthrough time matches and overall simulation accuracy.

- For future research, it is suggested to make further enhancements by adopting a compositional simulation model. This approach would provide a more accurate representation of the interaction of CO_2 with the aqueous and oleic phases, considering factors such as dissolution in water and the reduction of oil viscosity due to oil swelling, thereby reducing the model's dependency on CT-scan saturations. Additionally, obtaining more precise gas relative permeability measurements from experimental data would significantly enhance the modelling results.

- To avoid the need for segmented simulations, it is recommended to incorporate a hysteresis model into MRST, which is currently not present, enabling the modelling of the entire PA-WAG process in a single run.

Bibliography

[1] Richard O Afolabi et al. “Hydrophobically associating polymers for enhanced oil recovery–Part A: A review on the effects of some key reservoir conditions”. In: *Journal of petroleum science and engineering* 180 (2019), pp. 681–698.

[2] Shokufe Afzali et al. “Mathematical modeling and simulation of water-alternating-gas (WAG) process by incorporating capillary pressure and hysteresis effects”. In: *Fuel* 263 (2020), p. 116362.

[3] Shokufe. Afzali, Nima. Rezaei, and Sohrab Zendehboudi. “A comprehensive review on Enhanced Oil Recovery by Water Alternating Gas (WAG) injection”. In: *Fuel 227* (2016), pp. 218–246. DOI: `https://doi.org/10.1016/j.fuel.2018.04.015`.

[4] Tarek. Ahmed. *Reservoir Engineeering Handbook*. 5th ed. Cambridge, M.A: Gulf Professional Publishing, 2006.

[5] Emmanuel Ajoma et al. “Water-saturated CO2 injection to improve oil recovery and CO2 storage”. In: *Applied energy* 266 (2020), p. 114853.

[6] Abdulkareem M AlSofi, Jinxun Wang, and Ziyad F Kaidar. “SmartWater synergy with chemical EOR: Effects on polymer injectivity, retention and acceleration”. In: *SPE EOR Conference at Oil and Gas West Asia*. OnePetro. 2018.

[7] Kai Bao et al. “Fully implicit simulation of polymer flooding with MRST”. In: *Computational Geosciences* 21.5-6 (2017), pp. 1219–1244.

[8] RH Brooks and AT Corey. “Hydraulic properties of porous media. Hydrology Paper No. 3”. In: *Civil Engineering Department, Colorado State University, Fort Collins, CO* (1964).

[9] Se E Buckley and MCi Leverett. “Mechanism of fluid displacement in sands”. In: *Transactions of the AIME* 146.01 (1942), pp. 107–116.

[10] Philip Crosbie Carman. “Fluid flow through a granular bed”. In: *Trans. Inst. Chem. Eng. London* 15 (1937), pp. 150–156.

[11] Harry L Chang. “Polymer flooding technology yesterday, today, and tomorrow”. In: *Journal of Petroleum Technology* 30.08 (1978), pp. 1113–1128.

[12] Jes Reimer Christensen, Erling Halfdan Stenby, and Arne Skauge. “Review of WAG field experience”. In: *SPE Reservoir Evaluation & Engineering* 4.02 (2001), pp. 97–106.

[13] “Dilute solution behaviour of polyacrylamides in aqueous media”. In: *European Polymer Journal* 35.3 (1999), pp. 517–525. ISSN: 0014-3057. DOI: `https://doi.org/10.1016/S0014-3057(98)00152-9`. URL: `https://www.sciencedirect.com/science/article/pii/S0014305798001529`.

[14] Pauline M Doran. *Bioprocess engineering principles*. Elsevier, 1995.

[15] Ali Mohsenatabar Firozjaii and Hamid Reza Saghafi. “Review on chemical enhanced oil recovery using polymer flooding: Fundamentals, experimental and numerical simulation”. In: *Petroleum* 6.2 (2020), pp. 115–122.

[16] LW Holm and VA Josendal. “Mechanisms of oil displacement by carbon dioxide”. In: *Journal of petroleum Technology* 26.12 (1974), pp. 1427–1438.

[17] David D Huang and Matt M Honarpour. “Capillary end effects in coreflood calculations”. In: *Journal of Petroleum Science and Engineering* 19.1-2 (1998), pp. 103–117.

[18] Odd Steve Hustad and Torleif Holt. “Gravity stable displacement of oil by hydrocarbon gas after waterflooding”. In: *SPE Improved Oil Recovery Conference?* SPE. 1992, SPE–24116.

[19] Martijn T. G. Janssen, Fabian A. Torres Mendez, and Pacelli L. J. Zitha. “Mechanistic Modeling of Water-Alternating-Gas Injection and Foam-Assisted Chemical Flooding for Enhanced Oil Recovery”. In: *Industrial & Engineering Chemistry Research* 59.8 (2020), pp. 3606–3616. DOI: `10.1021/acs.iecr.9b06356`. eprint: `https://doi.org/10.1021/acs.iecr.9b06356`. URL: `https://doi.org/10.1021/acs.iecr.9b06356`.

[20] Martijn. Janssen, Fardin. Azimi, and P.L.J. Zitha. “Immiscible Nitrogen Flooding in Bentheimer Sandstones: Comparing Gas Injection Schemes for Enhanced Oil Recovery”. In: *SPE Improved Oil Recovery Conference*. 108. DOI: `10.2118/190285-MS`.

[21] Perry M Jarrell et al. “Practical aspects of CO2 flooding: Richardson, Tex”. In: *Society of Petroleum Engineers Monograph Series* 22 (2002), p. 220.

[22] Fatemeh Kamali, Furqan Hussain, and Yildiray Cinar. “A Laboratory and Numerical-Simulation Study of Co-Optimizing CO2 Storage and CO2 Enhanced Oil Recovery”. In: *SPE Journal* 20 (June 2015). DOI: `10.2118/171520-PA`.

[23] Stein Krogstad et al. “MRST-AD–an open-source framework for rapid prototyping and evaluation of reservoir simulation problems”. In: *SPE Reservoir Simulation Conference?* SPE. 2015, D022S002R004.

[24] Madhav M Kulkarni and Dandina N Rao. “Experimental investigation of miscible and immiscible Water-Alternating-Gas (WAG) process performance”. In: *Journal of Petroleum Science and Engineering* 48.1-2 (2005), pp. 1–20.

[25] Laurent Laboureur, Mario Ollero, and David Touboul. “Lipidomics by Supercritical Fluid Chromatography”. In: *International Journal of Molecular Sciences* 16.6 (2015), pp. 13868–13884. ISSN: 1422-0067. DOI: `10.3390/ijms160613868`. URL: `https://www.mdpi.com/1422-0067/16/6/13868`.

[26] Larry W Lake et al. *Fundamentals of enhanced oil recovery*. Vol. 1. Society of Petroleum Engineers Richardson, TX, 2014.

[27] Larry. W. Lake. *Enhanced Oil Recovery*. 1st ed. Englewood Cliffs, N.J.: Prentice Hall, 1989.

[28] Knut-Andreas Lie. *An introduction to reservoir simulation using MATLAB/GNU Octave: User guide for the MATLAB Reservoir Simulation Toolbox (MRST)*. Cambridge University Press, 2019.

[29] Wolfgang Littmann. *Polymer flooding*. Vol. 24. Elsevier, 1988.

[30] Nina Loahardjo, _ Winoto, and Norman R Morrow. “Oil recovery from Bentheim sandstone by sequential waterflooding and spontaneous imbibition”. In: *Petrophysics* 54.06 (2013), pp. 547–553.

[31] Osama Massarweh and Ahmad S. Abushaikha. “A review of recent developments in CO2 mobility control in enhanced oil recovery”. In: *Petroleum* 8.3 (2022), pp. 291–317. ISSN: 2405-6561. DOI: `https://doi.org/10.1016/j.petlm.2021.05.002`. URL: `https://www.sciencedirect.com/science/article/pii/S2405656121000420`.

[32] David H Merchant. “Life beyond 80: A look at conventional WAG recovery beyond 80% HCPV injection in CO2 tertiary floods”. In: *SPE International Conference on CO2 Capture, Storage, and Utilization*. OnePetro. 2010.

[33] Mohsen Mirzaie Yegane, Elisa Battistutta, and Pacelli Zitha. “Mechanistic Simulation and History Matching of Alkaline-Surfactant-Polymer ASP Core Flooding Experiment at Optimum vs. Under-Optimum Salinity Conditions”. In: SPE Europec featured at EAGE Conference and Exhibition (2019). DOI: `10.2118/195564-MS`. URL: `https://doi.org/10.2118/195564-MS`.

[34] Mohsen Mirzaie Yegane, Pouyan E. Boukany, and Pacelli Zitha. “Fundamentals and Recent Progress in the Flow of Water-Soluble Polymers in Porous Media for Enhanced Oil Recovery”. In: *Energies* 15.22 (2022). ISSN: 1996-1073. DOI: `10.3390/en15228575`. URL: `https://www.mdpi.com/1996-1073/15/22/8575`.

[35] Mohsen Mirzaie Yegane et al. “Flow Enhancement of Water-Soluble Polymers through Porous Media by Preshearing”. In: *Industrial & Engineering Chemistry Research* 60.8 (2021), pp. 3463–3473. DOI: `10.1021/acs.iecr.1c00099`. eprint: `https://doi.org/10.1021/acs.iecr.1c00099`. URL: `https://doi.org/10.1021/acs.iecr.1c00099`.

[36] Necmettin Mungan. “Carbon dioxide flooding-fundamentals”. In: *Journal of Canadian Petroleum Technology* 20.01 (1981).

[37] M. Muskat. *Physical principles of oil production*. 1st ed. New York: McGraw-Hill Book Co., 1949.

[38] Riley B. Needham and Peter H. Doe. “Polymer Flooding Review”. In: *Journal of Petroleum Technology* 39.12 (1987), pp. 1503–1507. ISSN: 0149-2136. DOI: `10.2118/17140-PA`. URL: `https://doi.org/10.2118/17140-PA`.

[39] SAT Nezhad et al. “Experimental study on applicability of water-alternating-CO2 injection in the secondary and tertiary recovery”. In: *SPE International Oil Conference and Exhibition in Mexico*. SPE. 2006, SPE–103988.

[40] P-E Øren, Stig Bakke, and Ole Jakob Arntzen. “Extending predictive capabilities to network models”. In: *SPE journal* 3.04 (1998), pp. 324–336.

[41] Anna E Peksa, Karl-Heinz AA Wolf, and Pacelli LJ Zitha. “Bentheimer sandstone revisited for experimental purposes”. In: *Marine and Petroleum Geology* 67 (2015), pp. 701–719.

[42] Thomas Ramstad et al. “Relative permeability calculations from two-phase flow simulations directly on digital images of porous rocks”. In: *Transport in Porous Media* 94.2 (2012), pp. 487–504.

[43] Sandeep Rellegadla, Shikha Jain, and Akhil Agrawal. “Oil reservoir simulating bioreactors: tools for understanding petroleum microbiology”. In: *Applied microbiology and biotechnology* 104 (2020), pp. 1035–1053.

[44] E Fernandez Righi et al. “Experimental study of tertiary immiscible WAG injection”. In: *SPE/DOE Symposium on Improved Oil Recovery*. OnePetro. 2004.

[45] Kiani Sajad, Shirin Alexander, and Andrew Barron. *Nanoparticles, Polymers, and Surfactants as Emerging Platforms in Fluid Flow Transport*. May 2020. DOI: `10.13140/RG.2.2.20954.36809`.

[46] Ramkrishna Sen. “Biotechnology in petroleum recovery: the microbial EOR”. In: *Progress in energy and combustion Science* 34.6 (2008), pp. 714–724.

[47] Hamidreza Shahverdi et al. “Three-phase relative permeability and hysteresis effect during WAG process in mixed wet and low IFT systems”. In: *Journal of Petroleum Science and Engineering* 78.3-4 (2011), pp. 732–739.

[48] James J Sheng. *Enhanced oil recovery field case studies*. Gulf Professional Publishing, 2013.

[49] R Simon and DJ Graue. “Generalized correlations for predicting solubility, swelling and viscosity behavior of CO2-crude oil systems”. In: *Journal of Petroleum Technology* 17.01 (1965), pp. 102–106.

[50] Rituraj Singh and Vikas Mahto. “Synthesis, characterization and evaluation of polyacrylamide graft starch/clay nanocomposite hydrogel system for enhanced oil recovery”. In: *Petroleum Science* 14 (2017), pp. 765–779.

[51] Upendra Singh Yadav and Vikas Mahto. “Modeling of partially hydrolyzed polyacrylamide-hexamine-hydroquinone gel system used for profile modification jobs in the oil field”. In: *Journal of Petroleum Engineering* 2013 (2012).

[52] Arne Skauge, Johne A Larsen, et al. “Three-phase relative permeabilities and trapped gas measurements related to WAG processes”. In: *SCA 9421, proceedings of the international symposium of the society of core analysts, Stavanger, Norway*. 1994.

[53] N. Sonnichsen. *Daily demand for crude oil worldwide from 2006 to 2020, with a forecast until 2026. 2021*. Visited on 2022-12-5. 2006. URL: `https://www.statista.com/statistics/271823/daily-global-crude-oil-demand-since-`.

[54] James. G. Speight. *Enhanced Recovery Methods for Heavy Oil and Tar Sands*. Houston, Texas: Gulf Publishing Company, 2013.

[55] Fred I Stalkup Jr. “Status of miscible displacement”. In: *Journal of Petroleum Technology* 35.04 (1983), pp. 815–826.

[56] Abdullah Taha and Mahmood Amani. “Overview of water shutoff operations in oil and gas wells; chemical and mechanical solutions”. In: *ChemEngineering* 3.2 (2019), p. 51.

[57] GQ Tang and Norman R Morrow. “Salinity, temperature, oil composition, and oil recovery by waterflooding”. In: *SPE Reservoir Engineering* 12.04 (1997), pp. 269–276.

[58] Ganesh. C. Thakur and Satter Abdus. *Integrated Waterflood Asset Management*. Tulsa, Okla: PennWell, 1998.

[59] VA Torrealba and Hussein Hoteit. “Improved polymer flooding injectivity and displacement by considering compositionally-tuned slugs”. In: *Journal of Petroleum Science and Engineering* 178 (2019), pp. 14–26.

[60] *Long Term Stability of Acrylamide Based Polymers during Chemically Assisted CO2 WAG EOR*. Vol. All Days. SPE Improved Oil Recovery Conference. Apr. 2014, SPE-169053–MS. DOI: `10.2118/169053-MS`. URL: `https://doi.org/10.2118/169053-MS`.

[61] Saul Vela, DW Peaceman, and Erik I Sandvik. “Evaluation of polymer flooding in a layered reservoir with crossflow, retention, and degradation”. In: *Society of Petroleum Engineers Journal* 16.02 (1976), pp. 82–96.

[62] Bing Wei. “Advances in Polymer Flooding”. In: *Viscoelastic and Viscoplastic Materials*. Ed. by Mohamed Fathy El-Amin. Rijeka: IntechOpen, 2016. Chap. 1. DOI: `10.5772/64069`. URL: `https://doi.org/10.5772/64069`.

[63] Li. Weirong et al. “Polymer-Alternating-Gas Simulation—A Case Study”. In: *SPE EOR Conference at Oil and Gas West Asia All Days*. 2014. DOI: `10.2118/169734-MS`.

[64] JR Welker. “Physical properties of carbonated oils”. In: *Journal of Petroleum Technology* 15.08 (1963), pp. 873–876.

[65] Thijs. van Wieren. “The effect of water-soluble polymers on water-alternating CO_2 performance in porous”. MA thesis. Delft, Zuid-Holland, Netherlands: Deflt University of Technology, 2022. URL: `http://resolver.tudelft.nl/uuid:353b7e86-177a-4720-8ba2-17dbd62c9c40`.

[66] Mohsen Mirzaie Yegane. “Effect of nanoparticles and pre-shearing on the performance of water-soluble polymers flow in porous media”. PhD thesis. Delft University of Technology, 2021.

[67] WF Yellig and RS Metcalfe. “Determination and Prediction of CO2 Minimum Miscibility Pressures (includes associated paper 8876)”. In: *Journal of Petroleum Technology* 32.01 (1980), pp. 160–168.

[68] Sanjay Surya Yerramilli, PL Zitha, and Ramesh Chandra Yerramilli. “Novel insight into polymer injectivity for polymer flooding”. In: *SPE European Formation Damage Conference and Exhibition*. SPE. 2013, SPE–165195.

[69] Hyunsang Yoo et al. “An experimental study on retention characteristics under two-phase flow considering oil saturation in polymer flooding”. In: *Journal of Industrial and Engineering Chemistry* 87 (2020), pp. 120–129.

[70] *The Role of Adsorption in Polymer Propagation Through Reservoir Rocks*. Vol. All Days. SPE International Conference on Oilfield Chemistry. Feb. 1987, SPE-16274–MS. DOI: `10.2118/16274-MS`. URL: `https://doi.org/10.2118/16274-MS`.

[71] *Two-Phase Flow Through Porous Media: Effect of an Adsorbed Polymer Layer*. Vol. All Days. SPE Annual Technical Conference and Exhibition. Oct. 1988, SPE-18085–MS. DOI: `10.2118/18085-MS`. URL: `https://doi.org/10.2118/18085-MS`.

A

2D Grid Discretisation with ImageJ

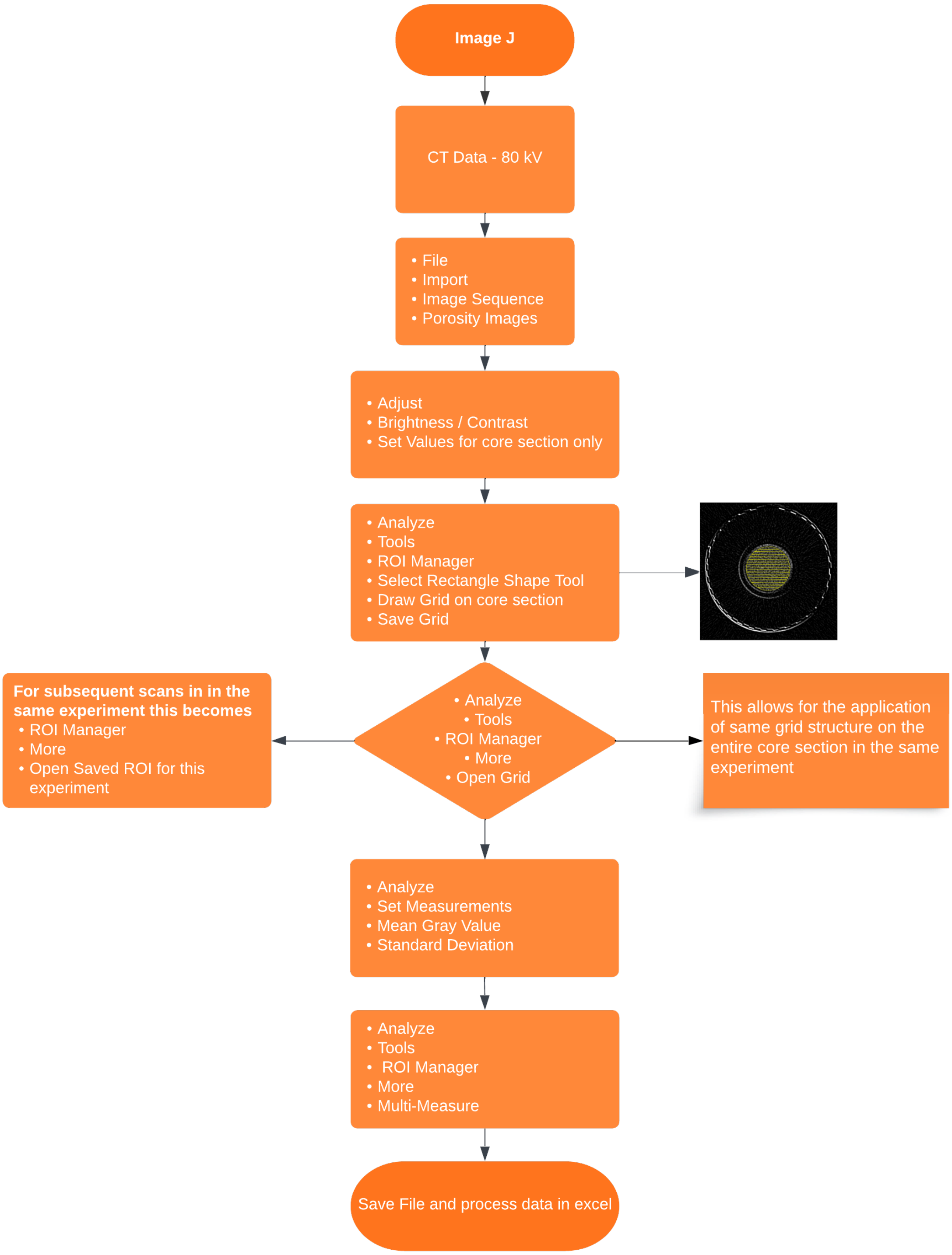

Figure A.1: ImageJ workflow flow chart, describing the process used to retrieve the data from CT-Scan and discretise the grid structure from 1D to 2D to compute each grid cell's porosity throughout the experiments.

B

Porosity and Permeability Maps

Exp. 1 Porosity and Permeability Maps

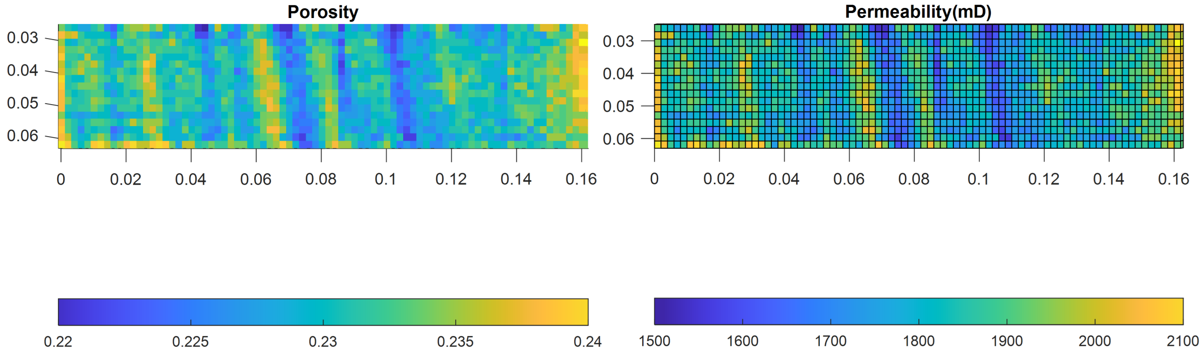

Figure B.1: 2D Grid consisting of 81 and 17 grid cells in the x and z directions, respectively, populated with porosity and permeability, representing the Bentheimer sandstone core in Exp. 1. All the discrete elements of the CT scan are used, and no coarsening is done due to the low resolution of the CT scan in this experiment

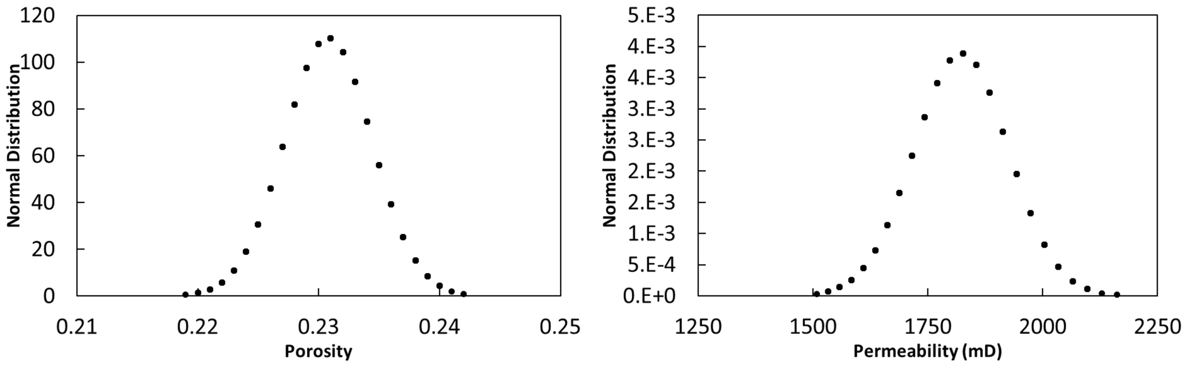

Figure B.2: A distribution of porosity values within the 2D Grid representing the Bentheimer sandstone core in Exp. 1. The permeability distribution is a direct function of porosity obtained using the Carman-Kozeny equation 3.22 and thus follows a similar distribution trend to porosity.

Exp. 2 Porosity and Permeability Maps

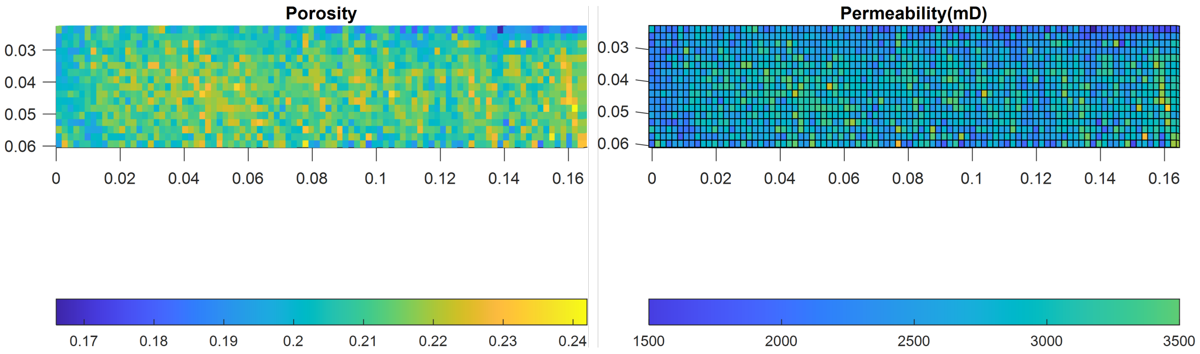

Figure B.3: 2D Grid consisting of 92 and 17 grid cells in the x and z directions, respectively, populated with porosity and permeability, representing the Bentheimer sandstone core in Exp. 2. Grid coarsening is applied in the X-direction by selecting a ratio of 3 fine cells per coarse cell, reducing 275 discrete CT slices to 92 grid cells

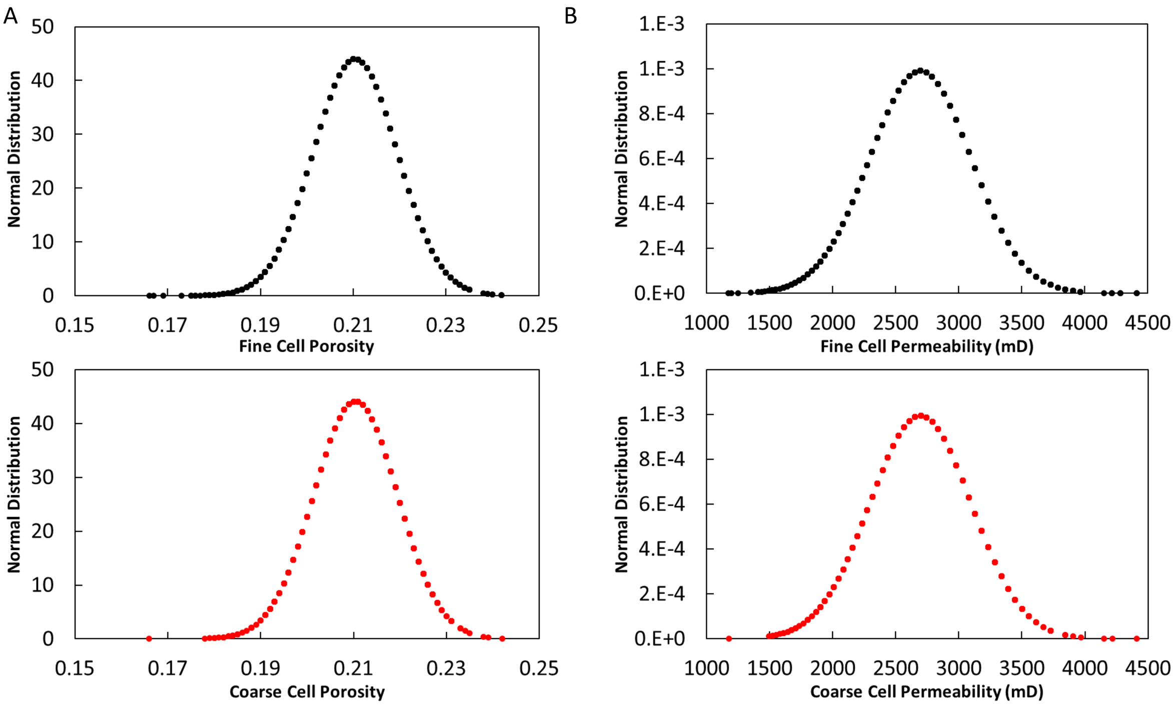

Figure B.4: (A) A comparison between the fine cell and coarse cell porosity distribution for Exp. 2 shows that even with the grid coarsening, the variability in porosity is well represented in the modelled core section. (B) A comparison between the fine and coarse cell permeability distribution for Exp. 2. The permeability distribution is a direct function of porosity obtained using the Carman-Kozeny equation 3.22 and thus follows a similar distribution trend to porosity.

Exp. 3 Porosity and Permeability Maps

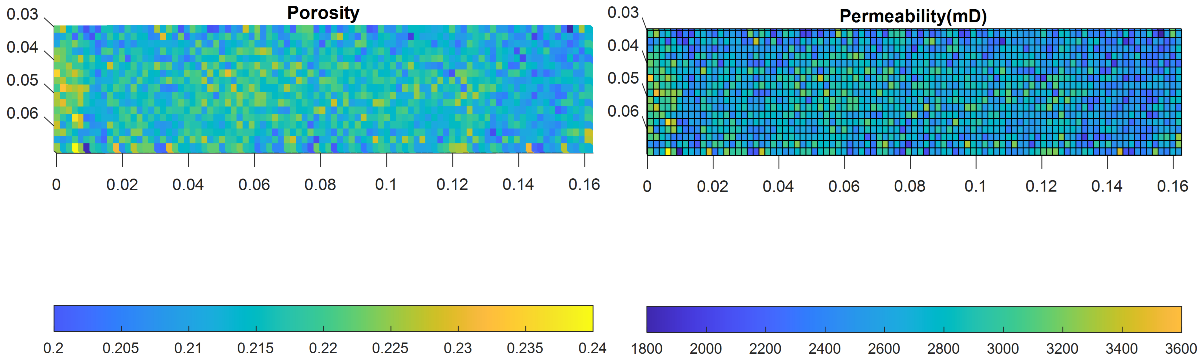

Figure B.5: 2D Grid consisting of 91 and 17 grid cells in the x and z directions, respectively, populated with porosity and permeability, representing the Bentheimer sandstone core in Exp. 3. Grid coarsening is applied in the X-direction by selecting a ratio of 3 fine cells per coarse cell, reducing 272 discrete CT slices to 91 grid cells

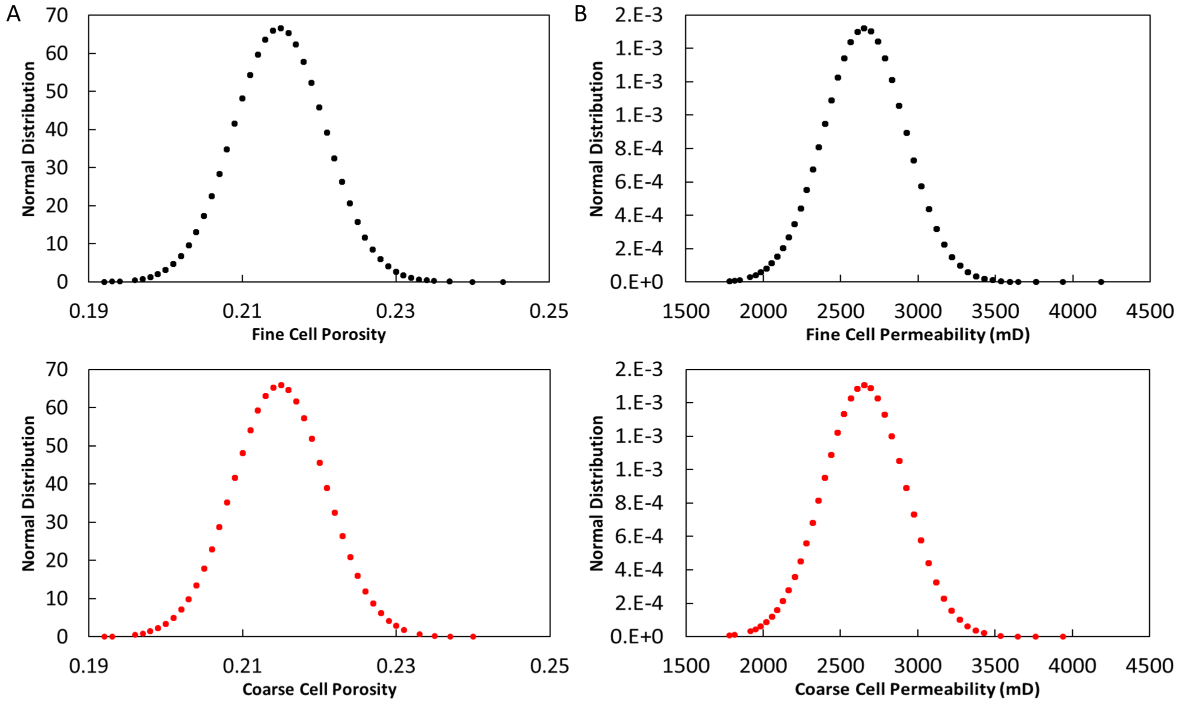

Figure B.6: (A) A comparison between the fine cell and coarse cell porosity distribution for Exp. 3 shows that even with the grid coarsening, the variability in porosity is well represented in the modelled core section. (B) A comparison between the fine and coarse cell permeability distribution for Exp. 3. The permeability distribution is a direct function of porosity obtained using the Carman-Kozeny equation 3.22 and thus follows a similar distribution trend to porosity.

C

Primary Drainage History Match Results

Exp. 1

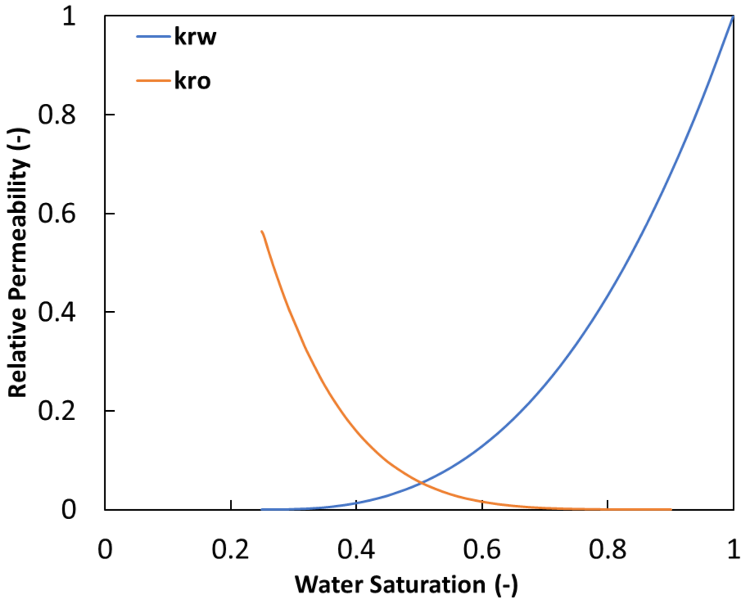

Figure C.1: Relative Permeability curves for the primary drainage stage in Exp. 1. k_{rw} and k_{ro} represent the water and oil relative permeability curves, respectively.

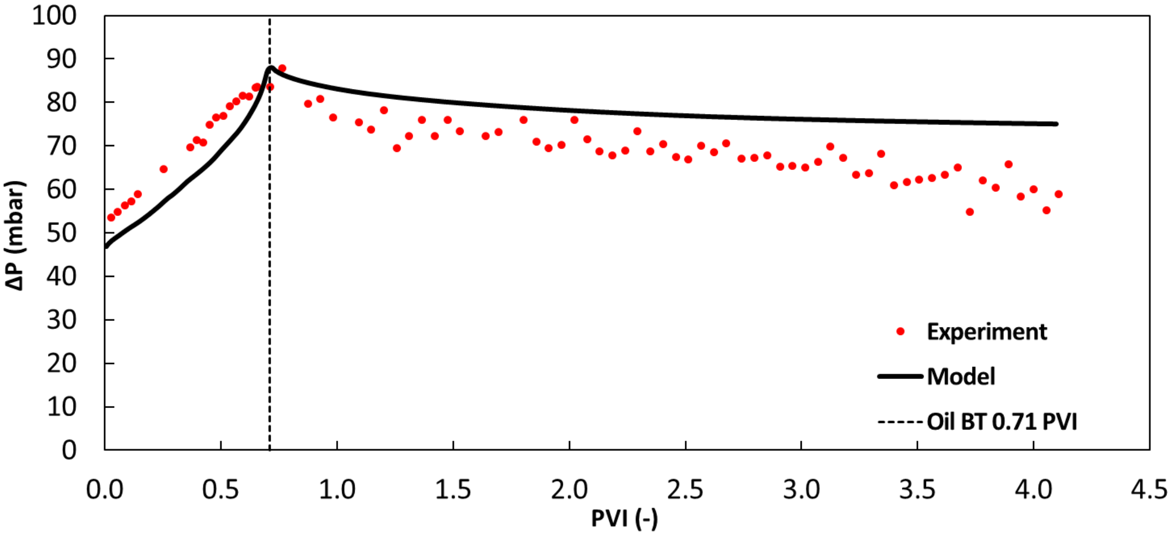

Figure C.2: Pressure drop match for primary drainage before Polymer injection in Bentheimer sandstone, Exp. 1. The breakthrough time for the oil phase was 0.71 ± 0.03

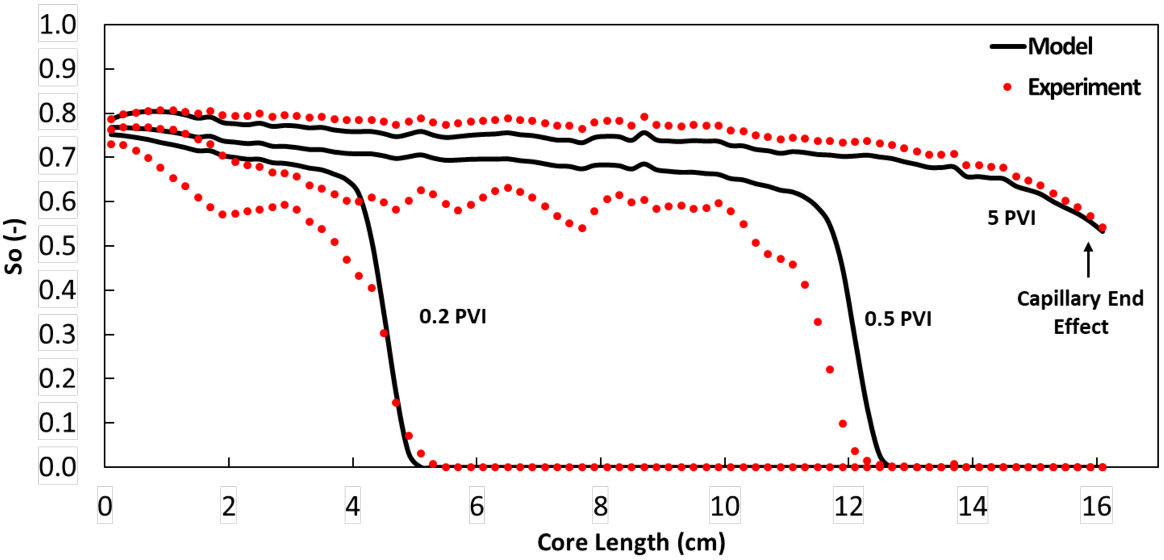

Figure C.3: Oil saturation match at several PVI during primary drainage in Exp. 1. Buckley-Leverett displacement at 0.2 and 0.5 PVI. The capillary-end effect was observed at the end of primary drainage at 5 PVI

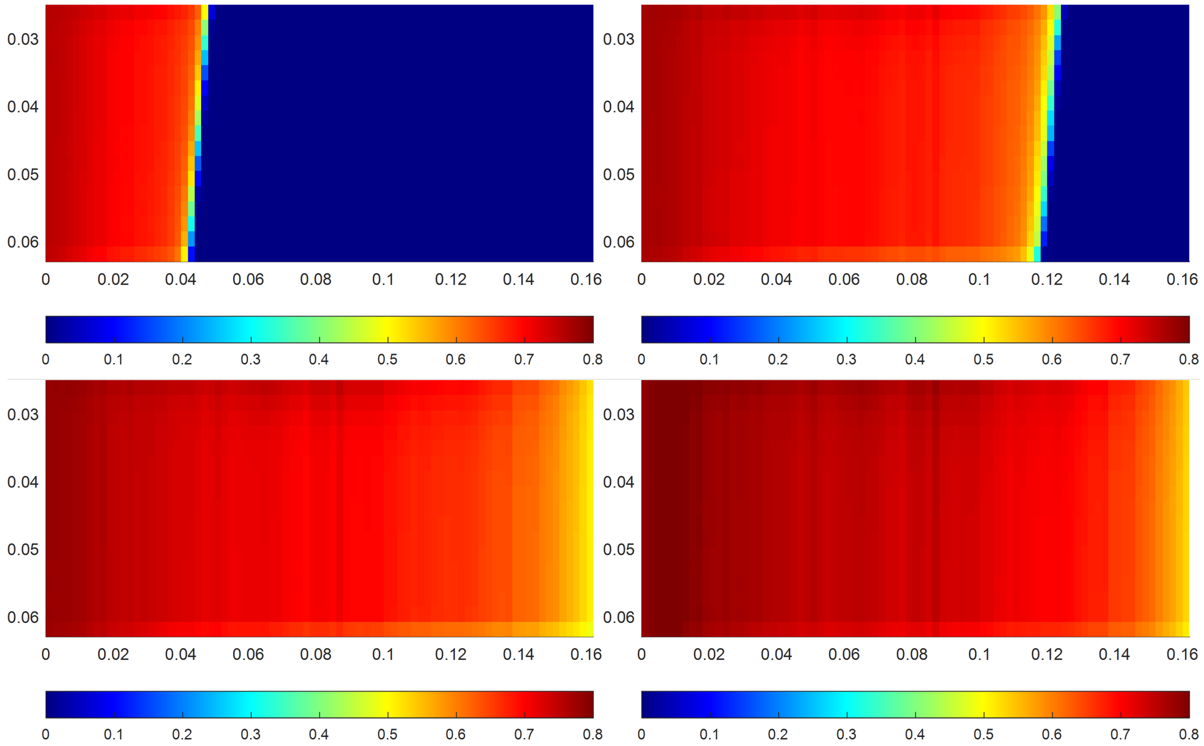

Figure C.4: Simulation visuals of primary drainage, Exp. 1 in MRST. Clockwise from top left - Oil saturation at 0.2, 0.5, 1 and 5 PVI Oil. The capillary-end effect is visible from the low oil saturation at 5 PVI in the last 2cm of the core.

Exp. 2

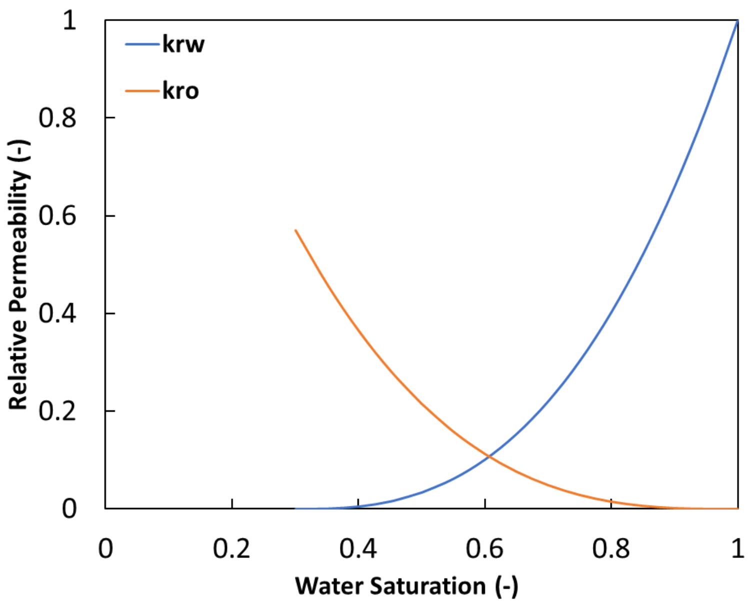

Figure C.5: Relative Permeability curves for the primary drainage stage in Exp. 2. k_{rw} and k_{ro} represent the water and oil relative permeability curves, respectively.

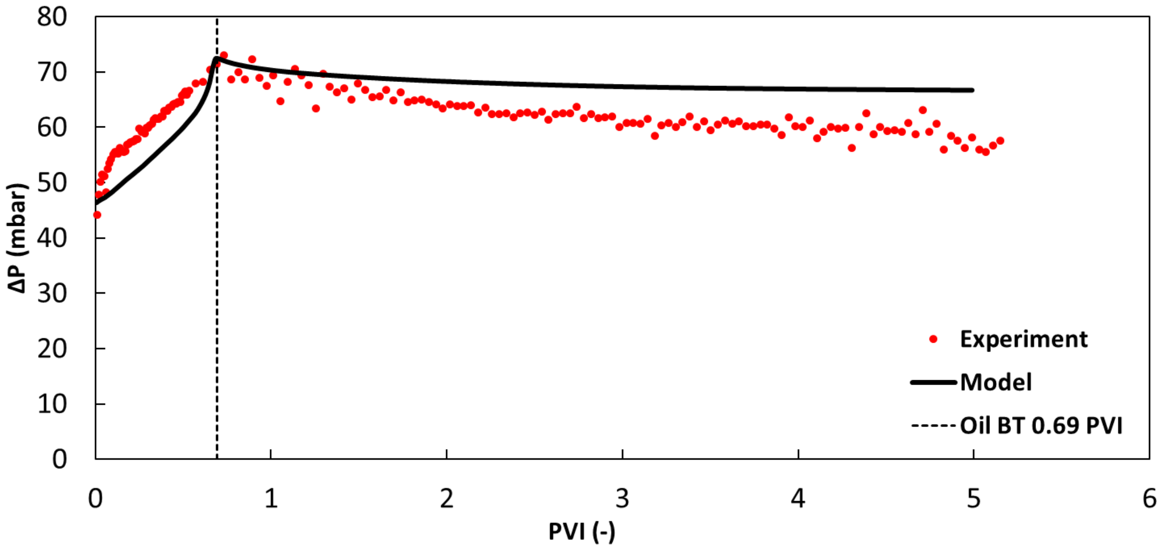

Figure C.6: Pressure drop match for primary drainage before CO_2 injection in Bentheimer sandstone, Exp. 2. The breakthrough time for the oil phase was 0.69 ± 0.04

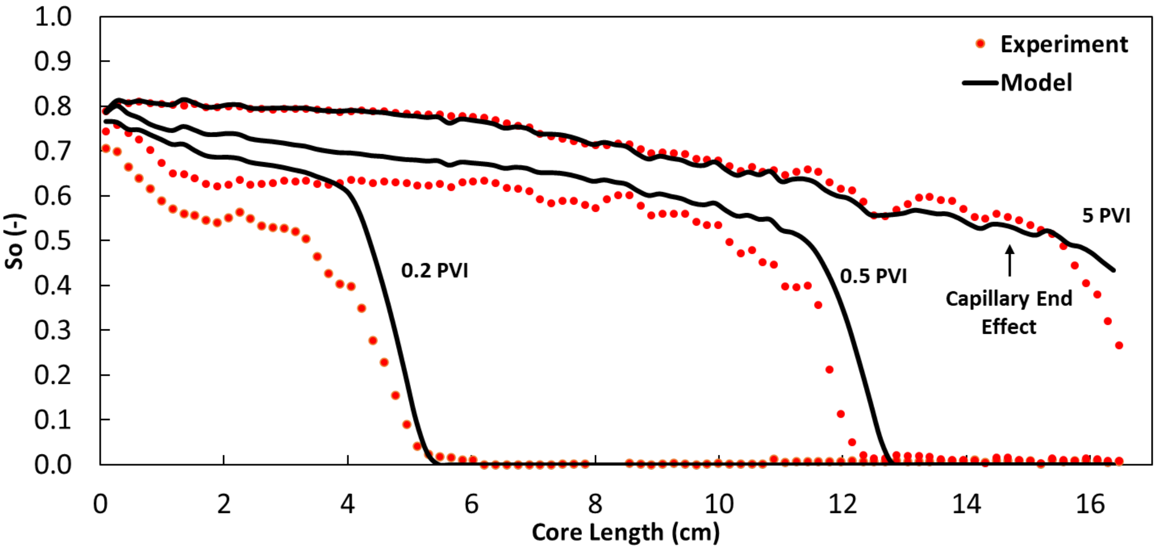

Figure C.7: Oil saturation match at several PVI during primary drainage in Exp. 2. Buckley-Leverett displacement at 0.2 and 0.5 PVI. The capillary-end effect was observed at the end of primary drainage at 5 PVI

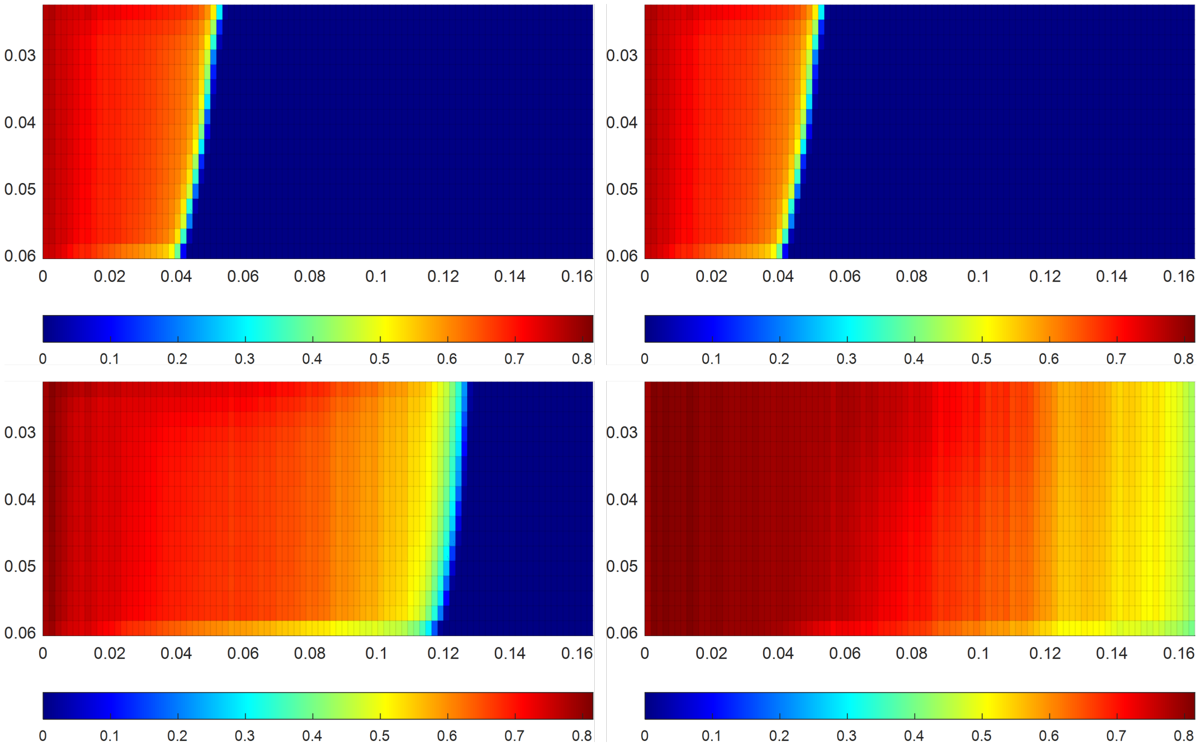

Figure C.8: Simulation visuals of primary drainage, Exp. 2 in MRST. Clockwise from top left - Oil saturation at 0.2, 0.5, 1 and 5 PVI Oil. The capillary-end effect is visible from the low oil saturation at 5 PVI in the last 2cm of the core.

D

Calculation of Inaccessible Pore Volume

Table D.1: Parameters and equations employed to compute the Inaccessible Pore Volume through the radius of gyration technique for the Bentheimer sandstone core for the Polymer flood and PA-WAG injection in Exp. 1 and Exp. 3, respectively.

Parameter	**Exp. 1**	**Exp. 3**	**Equation**	**Description**
$R_g(cm)$	0.0002	0.0002	-	Radius of Gyration
ϕ	0.23	0.21	-	Core Porosity
$d(cm)$	3.8	3.8	-	Core diameter
$A(cm^2)$	11.34	11.34	$\frac{3.14d^2}{4}$	Core Cross-Sectional Area
$L_{max}(cm)$	16.5	16.5	-	Core Length
$k_D(Darcy)$	1.82	2.65	-	Core Permeability
$k(cm^2)$	1.82e-7	2.65e-7	$k_D * 1e-7$	Core Permeability
$\rho_s(g/cm^3)$	2.65	2.65	-	Sand Density
$A_r(cm^{-1})$	126.67	91.6	$\sqrt{\frac{6\phi^3}{25k}}$	Surface area per unit volume
$A_s(cm^2/g)$	47.8	34.56	$\frac{A_r}{\rho_s}$	Surface area
$PV(cm^3)$	43.02	42.22	$A * L_{max} * \phi$	Pore Volume
α	1.2	1.2	-	Tortuosity of sand pack
$R_p(cm)$	0.003	0.004	$\alpha\sqrt{\frac{8k}{\phi}}$	Average Pore Throat Radius
$D_g(cm)$	0.036	0.052	$\frac{6(1-\phi}{A_r}$	Average Grain Diameter
$Depl$	1.79	1.55	$[1-\frac{2R_g}{R_p-(2R_g)}]^4$	Effect of Depletion Layer
BB	0.79	0.55	$Depl-1$	Pore Geometry Factor
frp	0.75	0.80	$\sqrt{\frac{1}{1+BB}}$	Pore space fraction available for polymer
IPV	0.25	0.20	$1-frp$	Inaccessible Pore Volume

E

PA-WAG Simulation Input Parameters

Table E.1: Summary of input parameters for cycle 1 of PA-WAG injection. This cycle was segmented into separate polymer and CO$_2$ runs.

Parameter	Cycle 1 - Polymer	Cycle 1 - CO$_2$
Number of Grid Blocks	91 x 1 x 17	
Grid Block Size (m x m x m)	0.002 x 0.038 x 0.002235	
Simulation Time (PVI)	0.22	1.20
Initial Saturation Distribution	Saturation distribution output of oil injection stage	Saturation distribution output of cycle 1 polymer
Injection Rate	Polymer – 0.00288 m^3/day (2 cm^3/min)	CO$_2$ - 0.0142 m^3/day (0.5cm^3/min)
Porosity	ϕ_{avg} = 0.215 (Calculated Porosity for each grid cell)	
Absolute Permeability (mD)	K_{avg} = 2651.6 (Calculated Permeability for each grid cell)	
Density (Oil/Polymer/ Gas) (kg/m^3)	829.7 / 1025.6 / -	829.7 / 1025.6 / 1.839
Viscosities (Oil / Polymer/ Gas) (cp)	2.28 / 6.57 / -	2.28 / 6.57 / 0.0146
Polymer Viscosity Multiplier	9	
IPV	0.2	
RRF	5.5	
Maximum Adsorption (kg/kg)	9.96E-05	
Mixing Parameter	1	
Maximum Polymer Concentration (kg/m^3)	2	

Table E.2: Summary of input parameters for cycle 2 of PA-WAG injection. This cycle was segmented into separate polymer and CO$_2$ runs.

Parameter	Cycle 2 - Polymer	Cycle 2 - CO$_2$
Number of Grid Blocks	91 x 1 x 17	
Grid Block Size (m x m x m)	0.002 x 0.038 x 0.002235	
Simulation Time (PVI)	0.22	1.20
Initial Saturation Distribution	Saturation distribution output of cycle 1 CO$_2$	Saturation distribution output of cycle 2 polymer
Injection Rate	Polymer – 0.00288 m^3/day (2 cm^3/min)	CO$_2$ - 0.0142 m^3/day (0.5cm^3/min)
Porosity	ϕ_{avg} = 0.215 (Calculated Porosity for each grid cell)	
Absolute Permeability (mD)	K_{avg} = 2651.6 (Calculated Permeability for each grid cell)	
Density (Oil/Polymer/ Gas) (kg/m^3)	829.7 / 1025.6 / 1.839	
Viscosities (Oil / Polymer/ Gas) (cp)	2.28 / 6.57 / 0.0146	
Polymer Viscosity Multiplier	9	
IPV	0.2	
RRF	5.5	
Maximum Adsorption (kg/kg)	9.96E-05	
Mixing Parameter	1	
Maximum Polymer Concentration (kg/m^3)	2	

Table E.3: Summary of input parameters for cycles 3-6 of PA-WAG injection. In each cycle, polymer and CO_2 injections were simulated in the same run.

Parameter	Cycle 3 - 6
Number of Grid Blocks	91 x 1 x 17
Grid Block Size (m x m x m)	0.002 x 0.038 x 0.002235
Simulation Time (PVI)	Polymer - 0.22 ; CO_2 - 1.20
Initial Saturation Distribution	Saturation distribution output of previous injection cycles
Injection Rate	Polymer – 0.00288 m^3/day (2 cm^3/min) ; CO_2 - 0.0142 m^3/day (0.5cm^3/min)
Porosity	ϕ_{avg} = 0.215 (Calculated Porosity for each grid cell)
Absolute Permeability (mD)	K_{avg} = 2651.6 (Calculated Permeability for each grid cell)
Density (Oil/Polymer/ Gas) (kg/m^3)	829.7 / 1025.6 / 1.839
Viscosities (Oil / Polymer/ Gas) (cp)	2.28 / 6.57 / 0.0146
Polymer Viscosity Multiplier	9
IPV	0.2
RRF	5.5
Maximum Adsorption (kg/kg)	9.96E-05
Mixing Parameter	1
Maximum Polymer Concentration (kg/m^3)	2

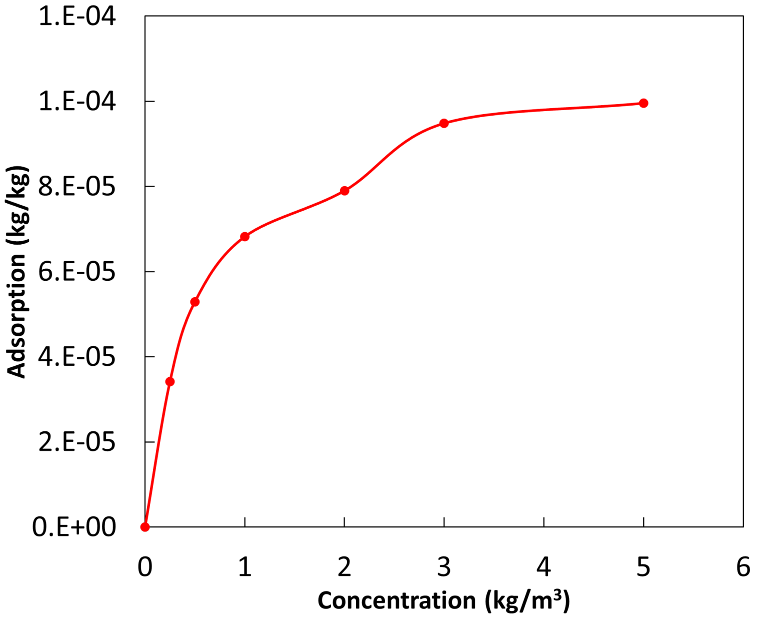

Figure E.1: Langmuir type isotherm for polymer adsorption in PA-WAG injection, Exp. 3 derived from the work of Yerramilli et al. (2013) [68] on HPAM polymers.

F

PA-WAG History Match Results

First PA-WAG Cycle

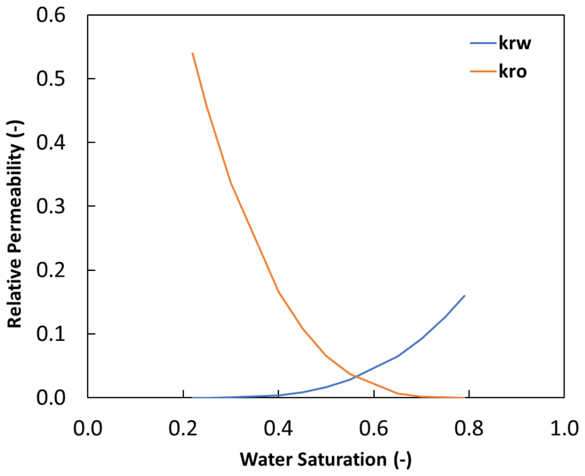

Figure F.1: Relative Permeability curves for the polymer injection phase in cycle 1 of PA-WAG injection, Exp. 3

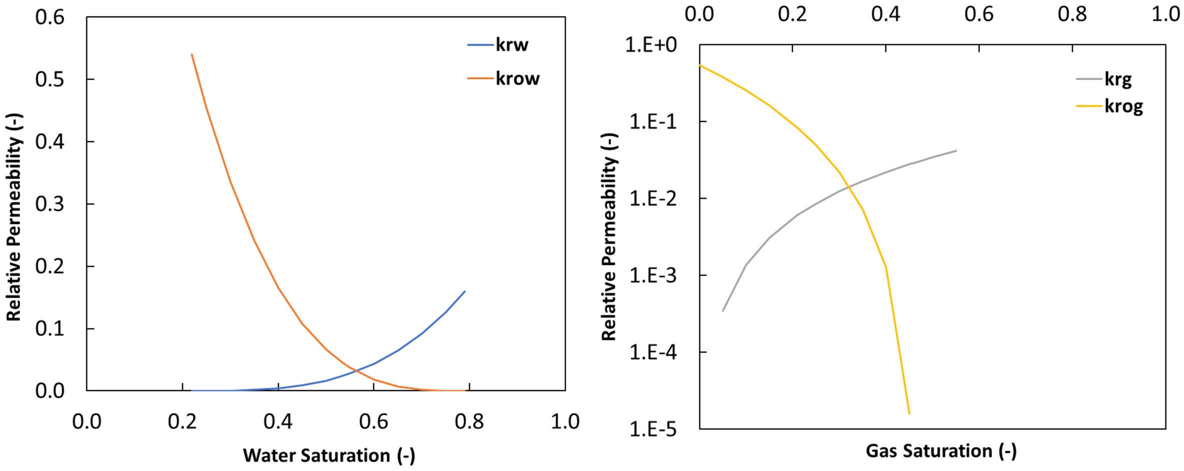

Figure F.2: Relative Permeability curves for the CO_2 injection phase in cycle 1 of PA-WAG injection, Exp. 3.

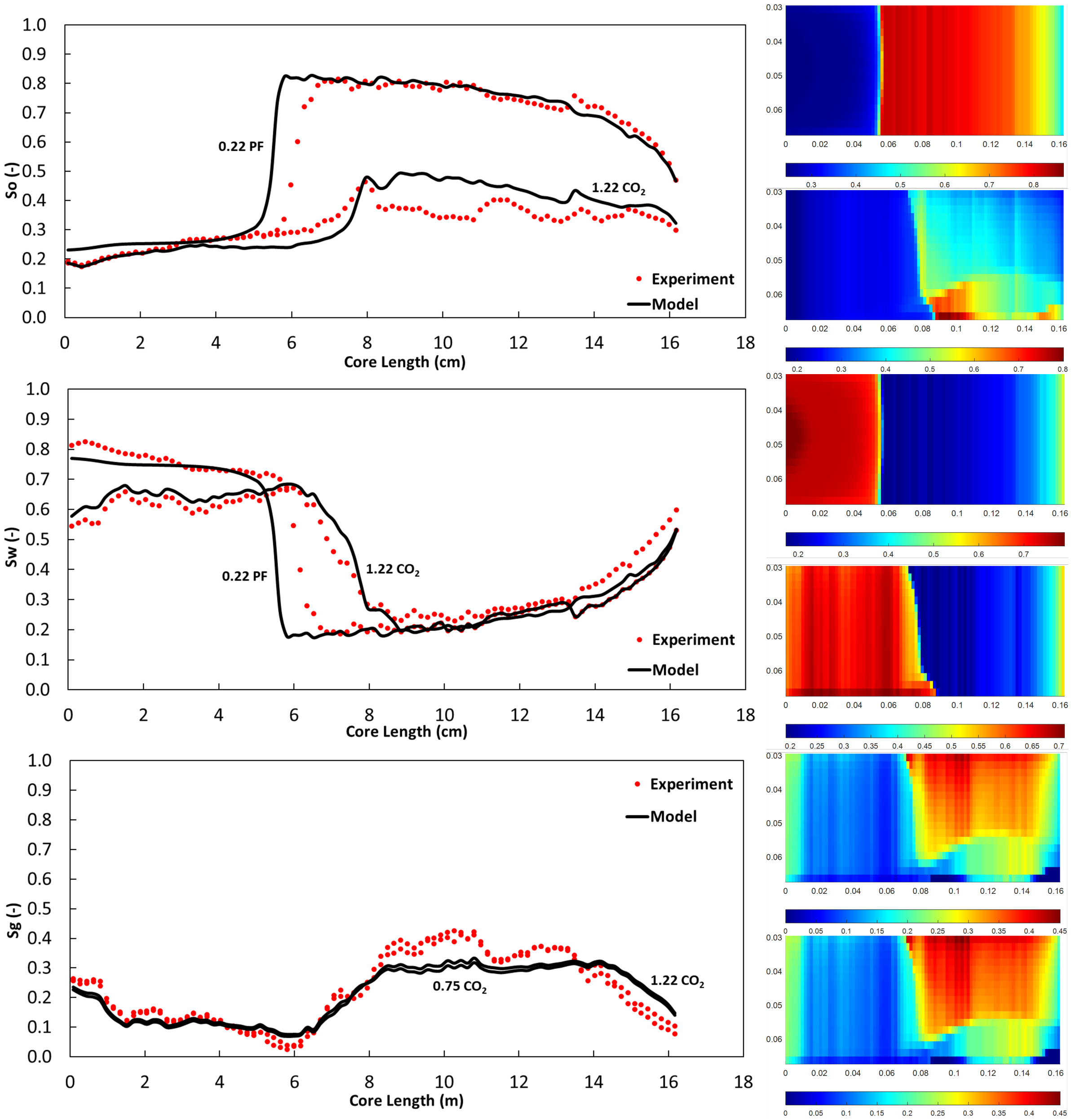

Figure F.3: Saturation profiles for oil (top), gas (middle) and water (bottom) at the end of cycle 1 after the completion of the polymer slug injection (0.22 PF) and CO_2 slug injection (1.22 CO_2) along with the corresponding MRST simulation. For Cycle 1, gas saturations are only presented for the CO_2 injection phase since there is no gas initially in the system at the start of the PA-WAG injection. Gas saturation becomes relevant only during the CO_2 injection stage.

Second PA-WAG Cycle

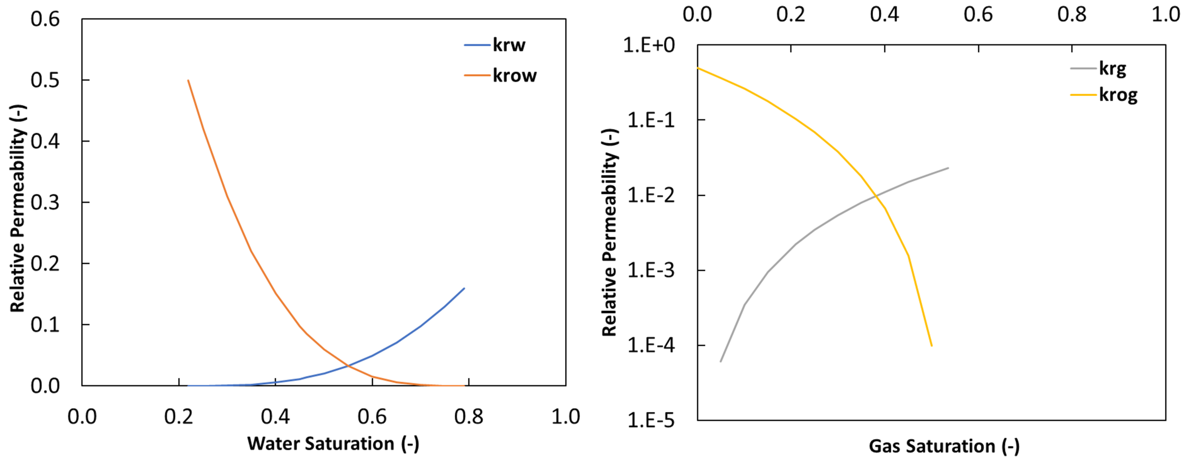

Figure F.4: Relative Permeability curves for the polymer injection phase in cycle 2 of PA-WAG injection, Exp. 3.

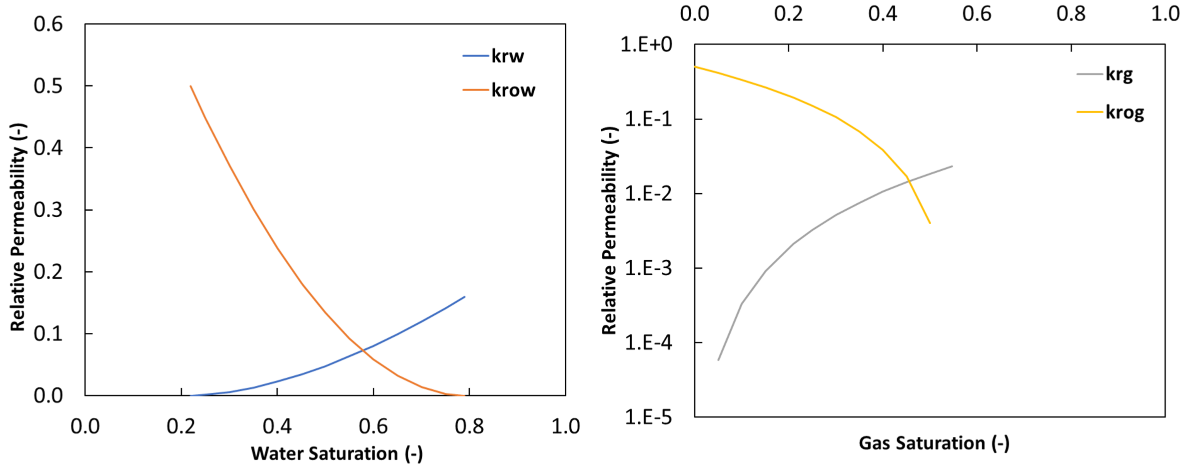

Figure F.5: Relative Permeability curves for the CO_2 injection phase in cycle 2 of PA-WAG injection, Exp. 3.

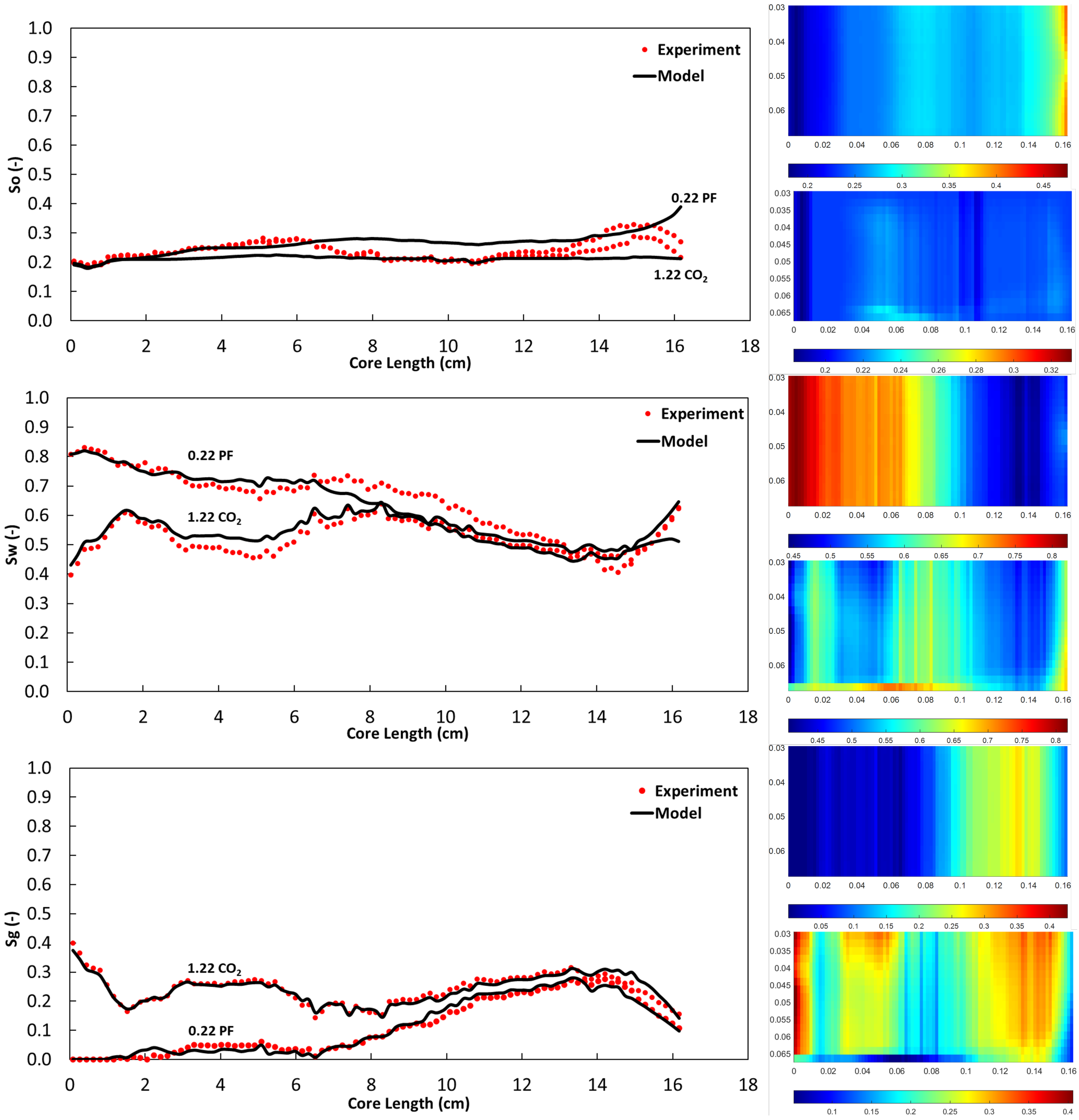

Figure F.6: Saturation profiles for oil (top), gas (middle), and water (bottom) after the polymer slug injection (0.22 PF) and CO$_2$ slug injection (1.22 CO$_2$) in cycle 2 with the corresponding MRST simulation visuals during this stage. Gas trapping becomes evident at the end of polymer injection in this cycle.

Subsequent PA-WAG Cycles

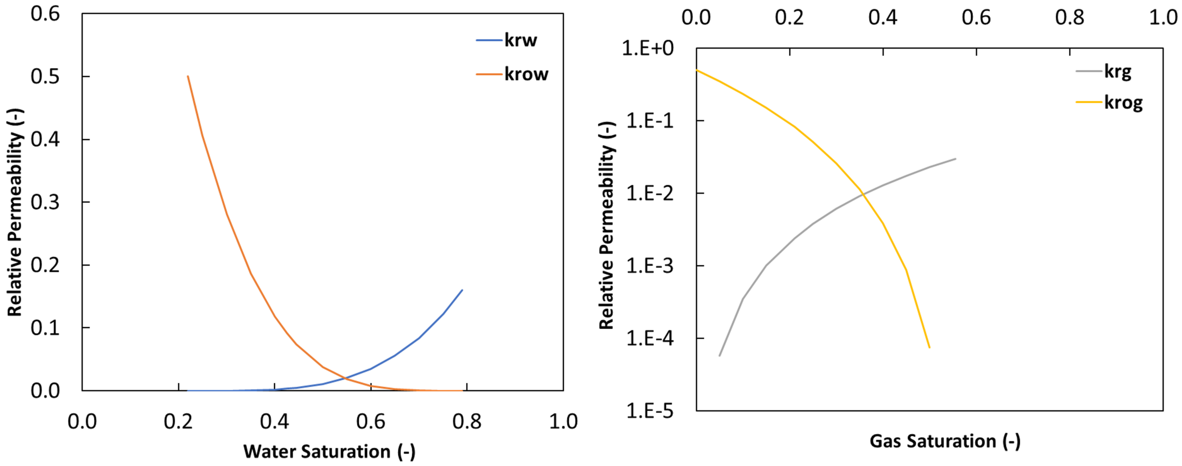

Figure F.7: Relative Permeability curves for cycle 3 of PA-WAG injection, Exp. 3.

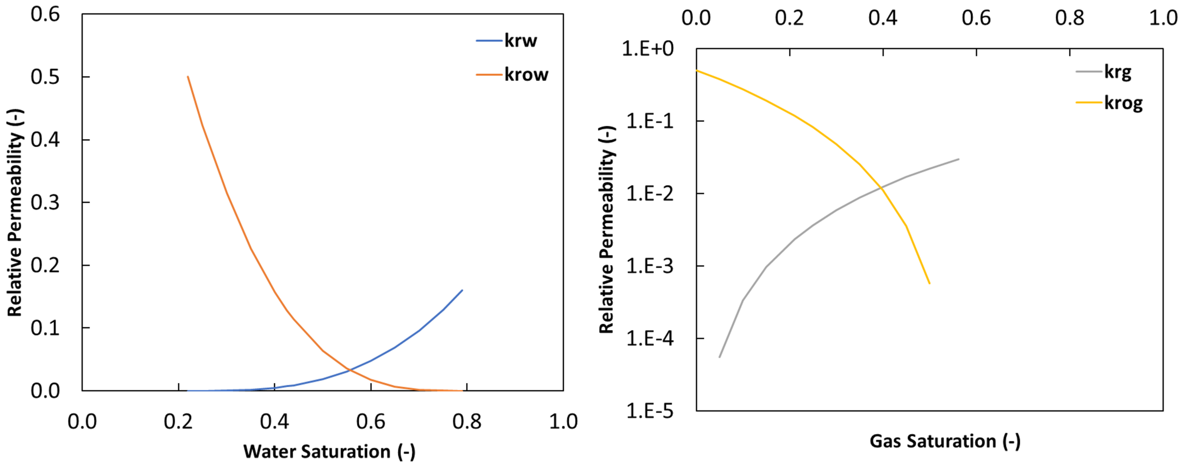

Figure F.9: Relative Permeability curves for cycle 5 of PA-WAG injection, Exp. 3.

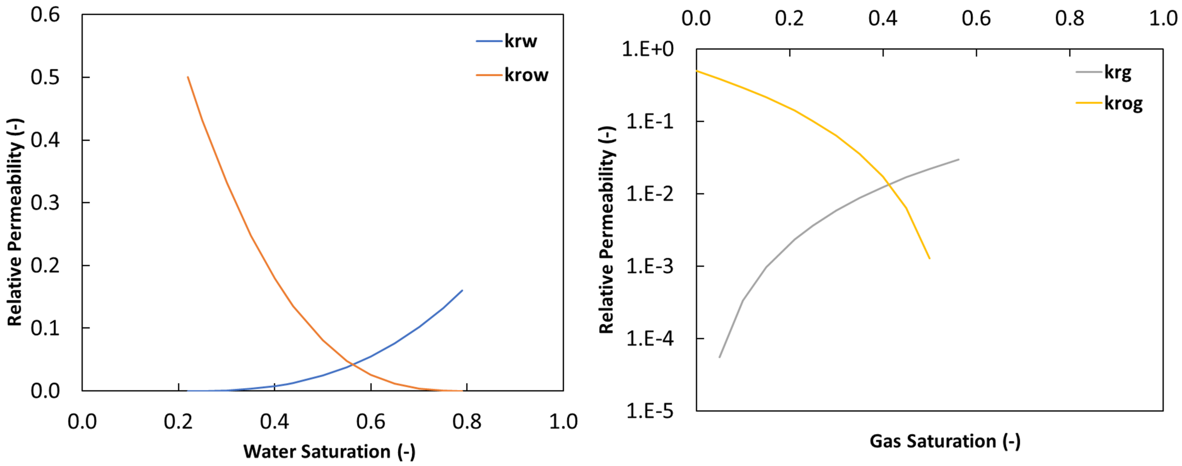

Figure F.11: Relative Permeability curves for cycle 6 of PA-WAG injection, Exp. 3.

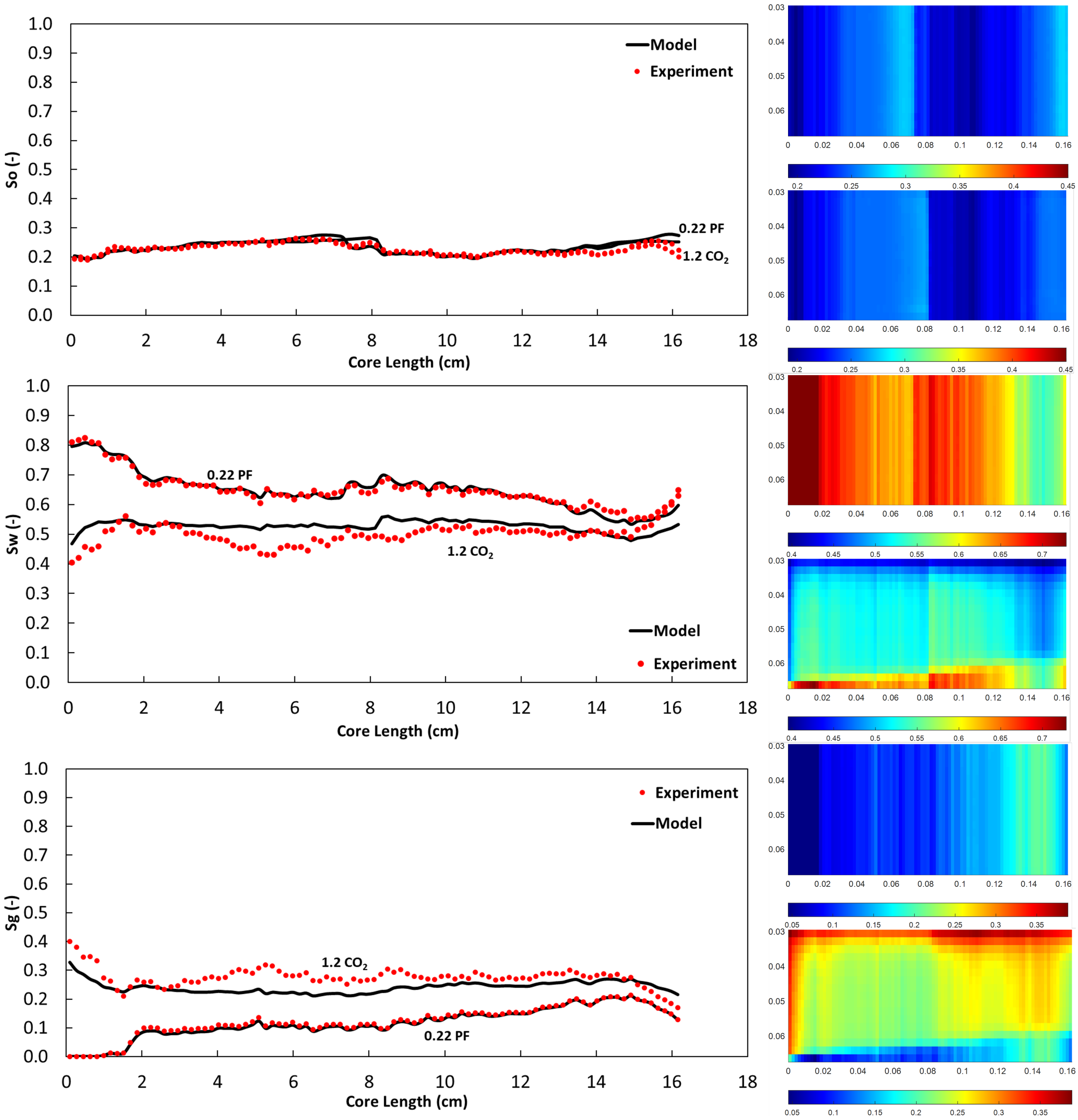

Figure F.8: Saturation profiles for oil (top), gas (middle), and water (bottom) after the polymer slug injection (0.22 PF) and CO_2 slug injection (1.22 CO_2) in cycle 3 with the corresponding MRST simulation visuals during this stage. For cycle 3, the oil saturations resulting from both polymer and CO_2 injection are identical and overlap each other due to negligible incremental recovery after the end of cycle 2.

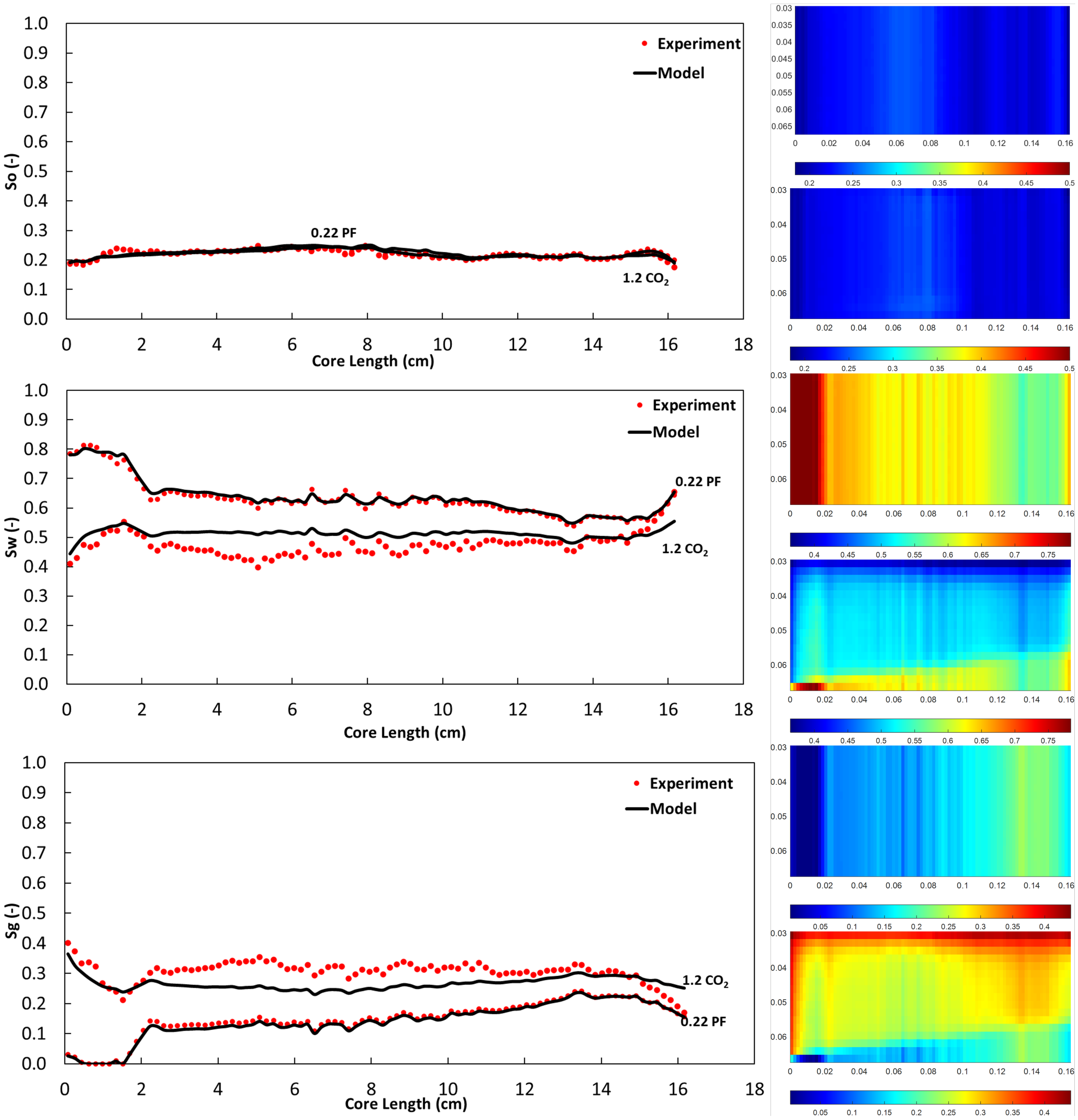

Figure F.10: Saturation profiles for oil (top), gas (middle), and water (bottom) after the polymer slug injection (0.22 PF) and CO$_2$ slug injection (1.22 CO$_2$) in cycle 5 with the corresponding MRST simulation visuals during this stage. For cycle 5, the oil saturations resulting from both polymer and CO$_2$ injection are identical and overlap each other due to negligible incremental recovery after the end of cycle 2.

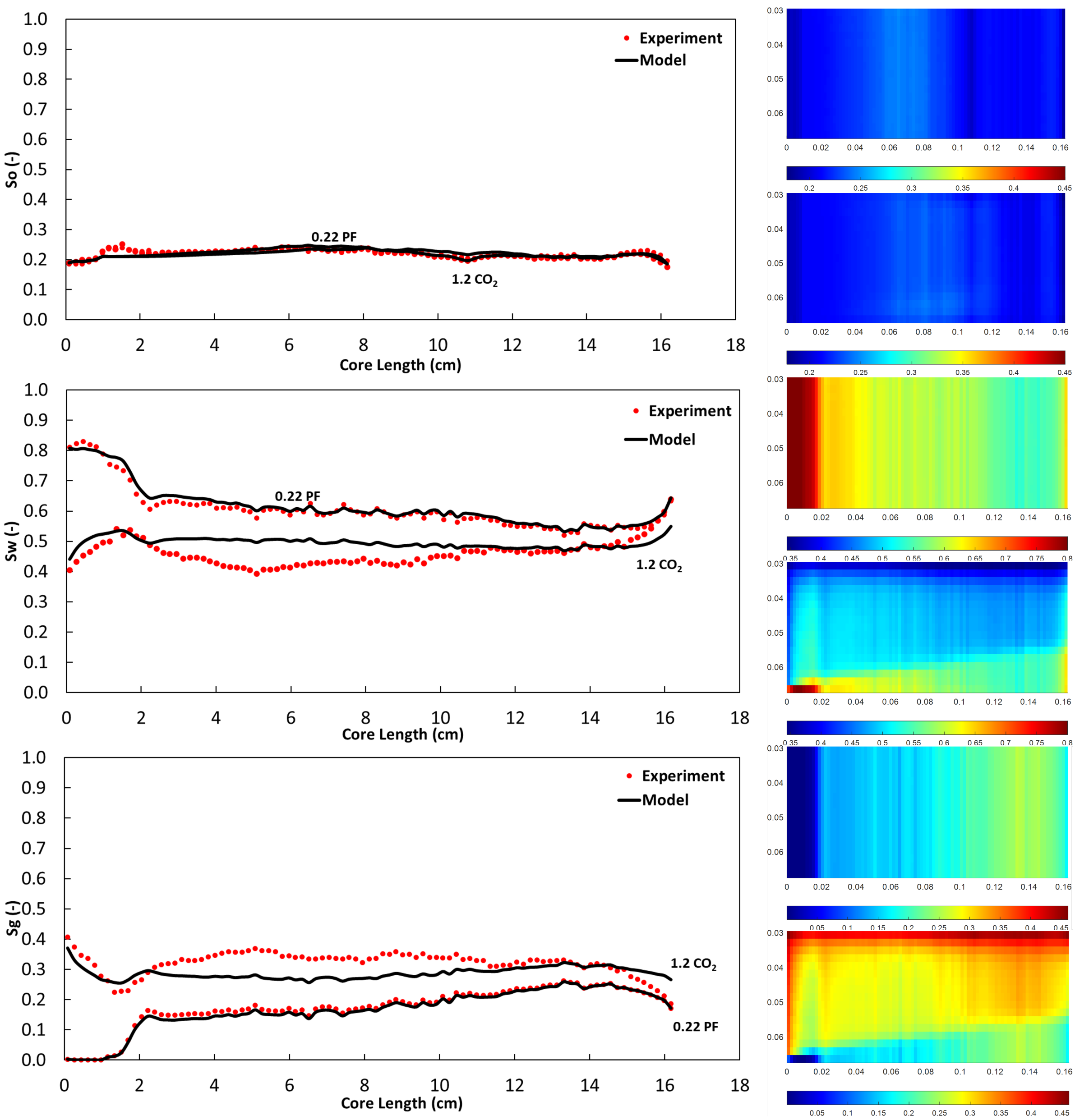

Figure F.12: Saturation profiles for oil (top), gas (middle), and water (bottom) after the polymer slug injection (0.22 PF) and CO_2 slug injection (1.22 CO_2) in cycle 6 with the corresponding MRST simulation visuals during this stage. For cycle 6, the oil saturations resulting from both polymer and CO_2 injection are identical and overlap each other due to negligible incremental recovery after the end of cycle 2.

G

Capillary Pressure with Leverett-J function

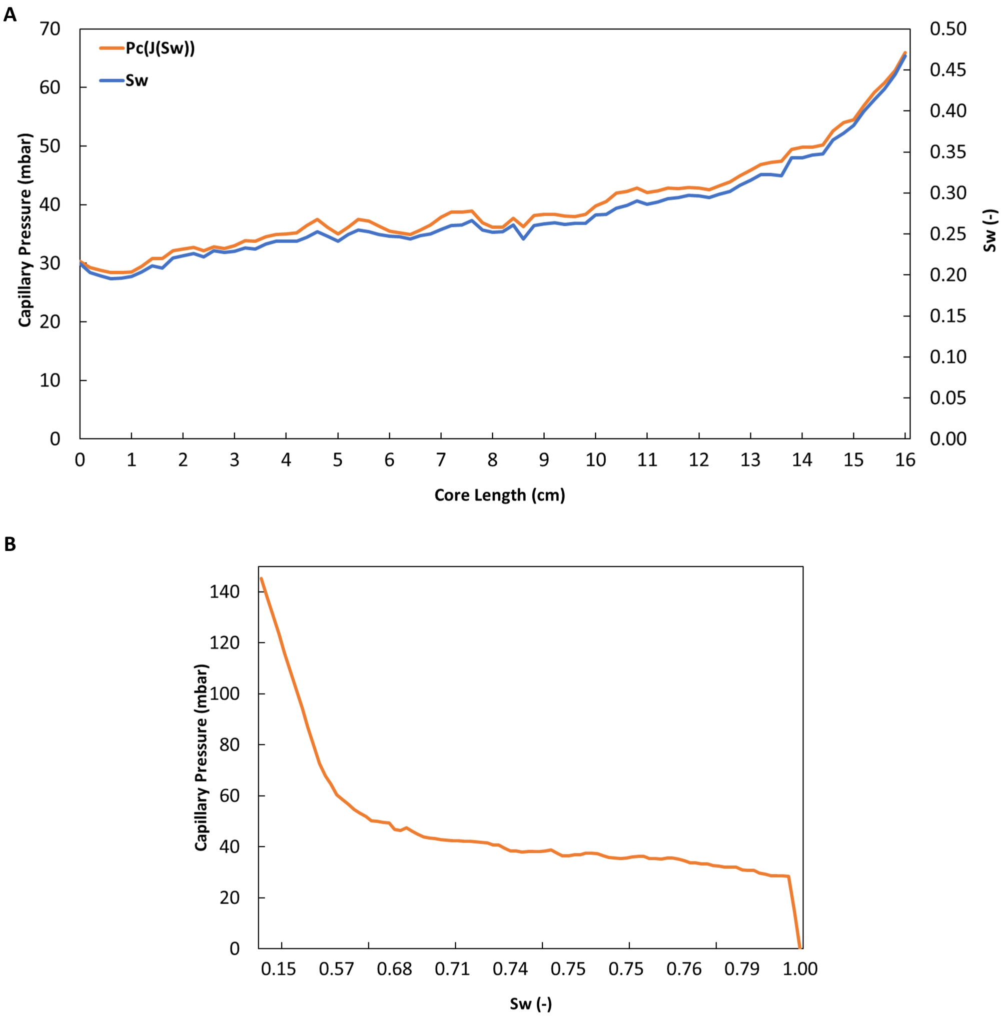

Figure G.1: (A) Correlation between the water saturation and capillary pressure along the core length. Elevated water saturation leads to increased capillary pressure demand for oil to displace water contributing to the capillary end effect at the core outlet in Exp. 1. (B) Capillary Pressure Curve generated using the Leverett-J function in Exp. 1.

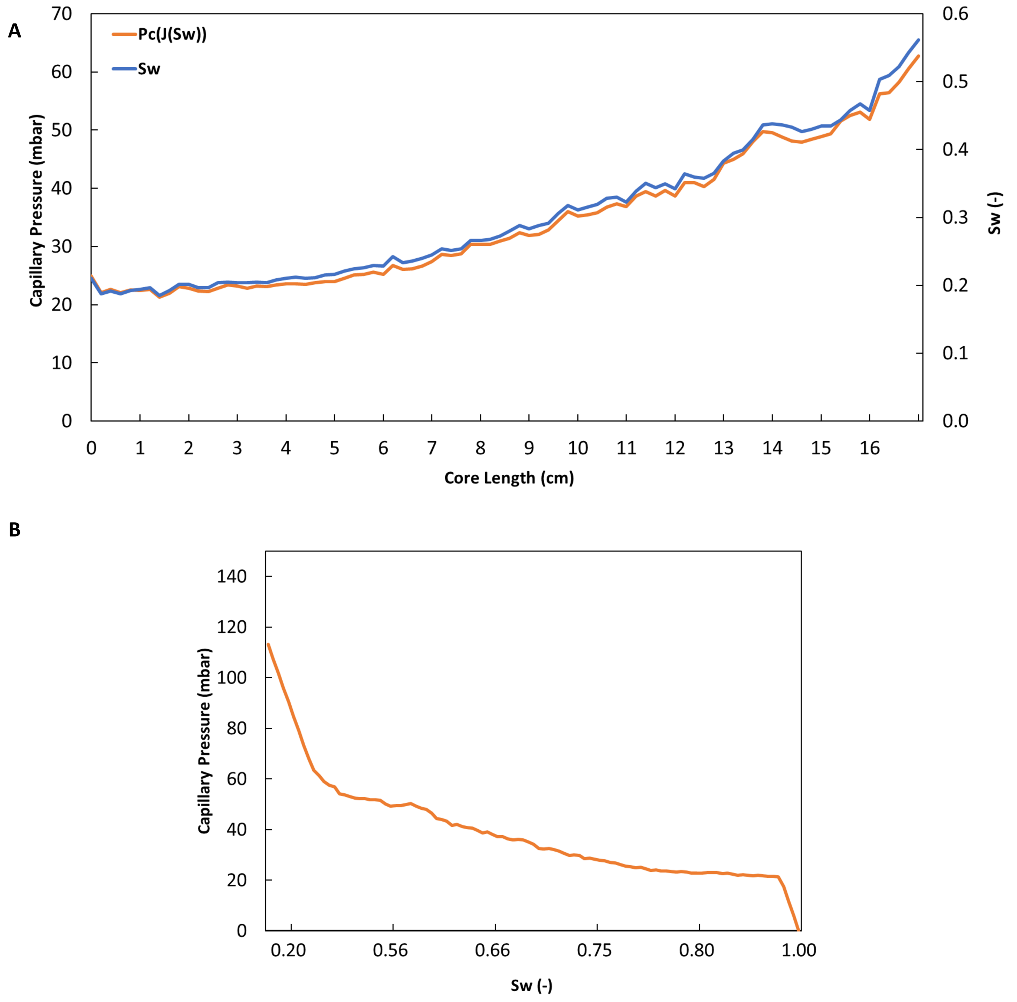

Figure G.2: (A) Correlation between the water saturation and capillary pressure along the core length. Elevated water saturation leads to increased capillary pressure demand for oil to displace water contributing to the capillary end effect at the core outlet in Exp. 2. (B) Capillary Pressure Curve generated using the Leverett-J function in Exp. 2.

A

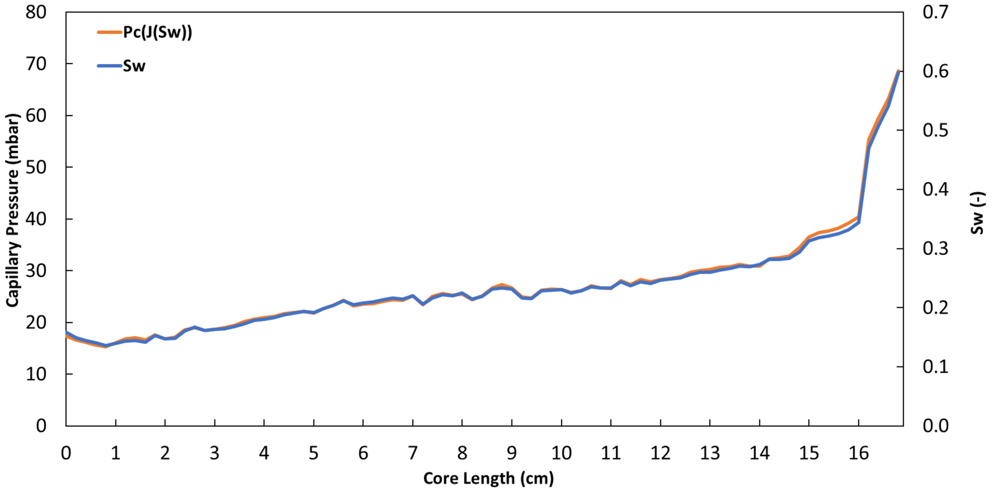

B

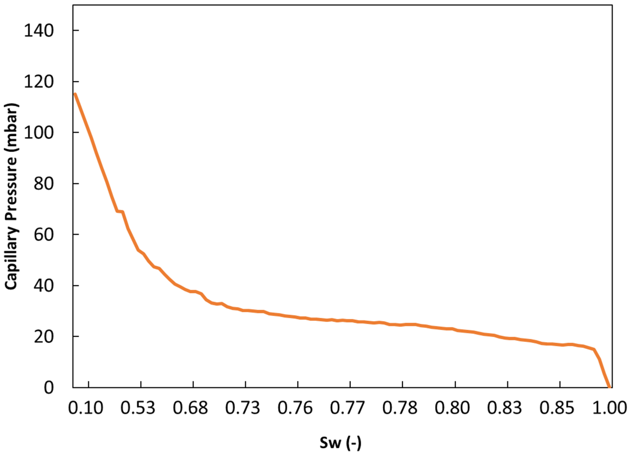

Figure G.3: (A) Correlation between the water saturation and capillary pressure along the core length. Elevated water saturation leads to increased capillary pressure demand for oil to displace water contributing to the capillary end effect at the core outlet in Exp. 3. (B) Capillary Pressure Curve generated using the Leverett-J function in Exp. 3.